TKK Dissertations 5
Espoo 2005

NUMERICAL SIMULATIONS OF MICROACOUSTIC RESONATORS AND FILTERS

Doctoral Dissertation

Tapani Makkonen

Helsinki University of Technology
Department of Engineering Physics and Mathematics
Materials Physics Laboratory

TKK Dissertations 5
Espoo 2005

NUMERICAL SIMULATIONS OF MICROACOUSTIC RESONATORS AND FILTERS

Doctoral Dissertation

Tapani Makkonen

Dissertation for the degree of Doctor of Science in Technology to be presented with due permission of the Department of Engineering Physics and Mathematics for public examination and debate in Auditorium F1 at Helsinki University of Technology (Espoo, Finland) on the 29th of April, 2005, at 12 noon.

Helsinki University of Technology
Department of Engineering Physics and Mathematics
Materials Physics Laboratory

Teknillinen korkeakoulu
Teknillisen fysiikan ja matematiikan osasto
Materiaalifysiikan laboratorio

Distribution:
Helsinki University of Technology
Department of Engineering Physics and Mathematics
Materials Physics Laboratory
P.O.Box 2200
FI - 02015 TKK
URL: http://focus.hut.fi/
Tel. +358-9-451 3168
Fax. +358-9-451 3164
E-mail: mafy@focus.hut.fi

ISBN 951-22-7635-6
ISBN 951-22-7636-4 (PDF)
ISSN 1795-2239
ISSN 1795-4584 (PDF)
URL: http://lib.hut.fi/Diss/2005/isbn9512276364/

TKK-DISS-1989

Otamedia Oy
Espoo 2005

HELSINKI UNIVERSITY OF TECHNOLOGY P.O. BOX 1000, FIN-02015 HUT http://www.hut.fi	ABSTRACT OF DOCTORAL DISSERTATION

Author Matti Tapani Makkonen

Name of the dissertation

Numerical Simulations of Microacoustic Resonators and Filters

Date of manuscript 25 January 2005	Date of the dissertation 29 April 2005
☐ Monograph	☑ Article dissertation (summary + original articles)

Department	Engineering Physics and Mathematics
Laboratory	Materials Physics Laboratory
Field of research	Surface and bulk acoustic wave resonators and filters
Opponent(s)	Prof. Leonhard M. Reindl
Supervisor	Prof. Rainer Salomaa
(Instructor)	Docent Victor P. Plessky

Abstract

This dissertation discusses numerical simulations of microwave acoustic resonators and bandpass filters employed in wireless telecommunication systems. In the first part of the dissertation, tailored finite element method (FEM) software with efficient numerical techniques is implemented and applied in the modeling of thin-film bulk-acoustic wave resonators (FBARs). Simulations with 3D FEM models of FBARs are carried out to investigate the effect of the electrode shape on the spurious resonances that often are present in the electrical response. The modeling results are validated through comparison of simulated and measured mechanical vibration amplitudes. The usability of the FEM tool is further demonstrated in simulations of a resonator design that features a clean electrical frequency response, free of spurious resonance peaks caused by anharmonic modes. Additionally, a method is proposed for determination of the elastic constants of a piezoelectric thin-film material. The technique is based on fitting of the computed dispersion curves of Lamb-wave modes to those measured from an FBAR using a scanning laser interferometer.

In the second part of this dissertation, numerical simulations are used to study propagation properties of longitudinal leaky surface acoustic wave (LLSAW) mode under periodic electrode array on YZ-cut lithium niobate (LN). A combined FEM/boundary element method is employed to compute the electric admittance of one-port synchronous LLSAW resonators. Simulations and experiments are used to derive the dependence of the resonator resonance frequencies and Q values on the electrode dimensions. Ladder-type bandpass filters exploiting the LLSAW mode are implemented on YZ-cut LN in the frequency range from 2.5 GHz to 5.2 GHz, with fundamental mode LLSAW resonators as building blocks. The results demonstrate that the high phase velocity of the LLSAW mode on YZ-cut LN allows inexpensive fabrication of wide-band, low-loss filters up to 5 GHz using conventional optical lithography.

The third topic considered is comprehensive modeling of a SAW duplexer, including electromagnetic modeling of the ceramic package. The parasitic capacitive and inductive couplings in the package are obtained using rigorous computation, allowing one to estimate the package effects on the duplexer performance.

Keywords finite element method, thin-film bulk acoustic wave resonator, surface acoustic wave, bandpass filter

Number of pages	79 p. + app. 10 p.	ISBN (printed)	951-22-7635-6
ISBN (pdf)	951-22-7636-4	ISBN (others)	
ISSN (printed)	1795-2239	ISSN (pdf)	1795-4584

Publisher Helsinki University of Technology, Materials Physics Laboratory

Print distribution

☑ The dissertation can be read at http://lib.tkk.fi/Diss/ 2005/isbn9512276364/

Preface

The research described in this dissertation has been carried out in the Materials Physics Laboratory at the Helsinki University of Technology, except for a period from November 2002 to February 2003 when I worked as a visiting researcher at Temex Microsonics (now TEMEX), Sophia-Antipolis, France. My work has been financially supported by Nokia Foundation and Foundation of Technology (TES, Finland) while CSC (the Finnish IT center for science) has provided computational resources.

I miss Professor Martti M. Salomaa, the director of the Materials Physics Laboratory. It is unfortunate that he did not live to witness the defence of my Thesis, as he acted as my supervisor starting from my Master's thesis and Licentiate thesis until the near completion of my doctoral work. I remember him for his endless efforts to secure the well-being of his students. I am most grateful for his trust, encouragement, and his instructions in the practices in science. His fingerprint will certainly show in my future doings.

The research on thin-film bulk-acoustic wave resonators (FBARs) was started at the end of 1996 on the initiative of Nokia Mobile Phones Ltd (NMP). The work was carried out also in collaboration with VTT (Technical Research Centre of Finland) Microelectronics. I thank Markku Ylilammi for his valuable help in modeling of FBARs and in understanding their characteristics, Jyrki Kaitila for his inspiring ideas, and Juha Ellä, Jyrki Molarius as well as Tuomas Pensala for useful discussions.

In surface-acoustic wave (SAW) theory and devices, I am indebted to Professor Victor Plessky, who introduced me to the intricacies of SAWs and encouraged me to take up the research of longitudinal leaky SAWs. His positive and enthusiastic attitude has been a great source of motivation and inspiration for me. He is always willing to help his students and share his insight with them. I have been privileged to work with him and benefit from the abundance of new fresh ideas he produces year after year. I also wish to express my gratitude to Professor Ali-Reza Baghai-Wadji and Professor Ken-ya Hashimoto for the lectures they delivered during their visits to the Materials Physics Laboratory; the lectures were most beneficial in increasing my understanding in wavelets and in SAW physics.

The research on longitudinal leaky SAW was carried out in intense collaboration with Temex Microsonics (now TEMEX), in the framework of Eureka project E! 2442 SUMO. I thank my superior William Steichen who made possible my visit to Temex Microsonics and Marc Solal for his interest in my work. I am also very grateful to all my colleagues there who made my stay a pleasant experience. I cordially thank Raphaël Lardat and Pascal Ventura for their hospitality. In particular, I appreciate and respect the company policy at Temex Microsonics that was favourable for publication of scientific results.

I am deeply grateful to Julius Koskela, former member of the SAW group, for implementing the periodic FEM/BEM software used to study the propagation properties of longitudinal leaky SAWs, as well as the initial version of the software for

modeling propagation of acoustic waves in layered structures. Furthermore, I appreciate his guidance in solution of many problems of SAW physics. I also thank my coauthors for their efforts and contributions.

I wish to thank the entire SAW group at the Materials Physics Laboratory for keeping up the spirit, in particular, Saku Lehtonen for his extensive comments on the manuscript as well as taking care of many practicalities of the dissertation procedure and Janne Salo for his advice on wave propagation. Johanna Meltaus and Sanna Härmä graced the otherwise so man-dominated laboratory and they kept me informed of the feminine point of view on many topics. I thank Olli Holmgren and Kimmo Kokkonen for their efforts on optical probing of the FBARs and SAW devices. My research progressed in the same pace with that of Jouni Knuuttila, who also started in the SAW group in the mid-1990s. I wish to express my gratitude to him both for tackling innumerable professional problems together with me, for his encouragement, and for his friendship off-duty. Especially, the lunches spent with the SAW group, characterized by imaginative discussions covering all topics between heaven and earth, were very joyful and provided a break from the daily routines.

I also gratefully acknowledge Eero Noponen for ensuring smooth operation of the computers and the network in the laboratory. Sami Virtanen deserves thanks for his valuable advice and the work he has carried out with impregnable discretion as the unofficial laboratory foreman after the passing of Professor Salomaa. All the members of the staff of the Materials Physics Laboratory, former and present, are recognized for their contribution to making the laboratory such a stimulating work community.

I generously thank all those who have shared with me the intriguing experiments in gastronomy, including Teemu Pohjola and Pekka Äyräs. Our culinary get-togethers have provided an excellent venue for fruitful exchange of opinions.

Finally, I am grateful to my parents for their continuing support, and my brother Anssi for all the exciting concert experiences.

Espoo, April 2005

Tapani Makkonen

List of publications

This dissertation is a review of the author's work in the fields of bulk and surface-acoustic wave technologies. It consists of an overview and the following selection of publications in these fields:

I T. Makkonen, A. Holappa, J. Ellä, and M. M. Salomaa, "Finite element simulations of thin-film composite BAW resonators", *IEEE Transactions on Ultrasonics, Ferroelectrics, and Frequency Control* **48**, 1241–1258 (2001).

II T. Makkonen, T. Pensala, J. Vartiainen, J. V. Knuuttila, J. Kaitila, and M. M. Salomaa, "Estimating materials parameters in thin-film BAW resonators using measured dispersion curves", *IEEE Transactions on Ultrasonics, Ferroelectrics, and Frequency Control* **51**, 42–51 (2004).

III T. Makkonen, V. P. Plessky, W. Steichen, V. I. Grigorievski, M. Solal, and M. M. Salomaa, "Longitudinal leaky SAW resonators and filters on YZ-$LiNbO_3$", *IEEE Transactions on Ultrasonics, Ferroelectrics, and Frequency Control*, (accepted).

IV T. Makkonen, V. P. Plessky, W. Steichen, and M. M. Salomaa, "Surface-acoustic-wave devices for the 2.5–5 GHz frequency range based on longitudinal leaky waves", *Applied Physics Letters* **82**, 3351–3353 (2003).

V T. Makkonen, V. P. Plessky, W. Steichen, S. Chamaly, C. Poirel, M. Solal, and M. M. Salomaa, "Fundamental mode 5 GHz surface-acoustic-wave filters using optical lithography", *Applied Physics Letters* **83**, 3596–3598 (2003).

VI T. Makkonen, S. Kondratiev, V. P. Plessky, T. Thorvaldsson, J. Koskela, J. V. Knuuttila, and M. M. Salomaa, "Surface acoustic wave impedance element ISM duplexer: modeling and optical analysis", *IEEE Transactions on Ultrasonics, Ferroelectrics, and Frequency Control* **48**, 652–665 (2001).

Throughout the overview, these publications are referred to by their Roman numerals.

Author's contribution

The papers in this dissertation are a result of work carried out in the Materials Physics Laboratory at the Helsinki University of Technology (HUT) during the years 1997–2003. Papers I-II report results obtained in collaboration with Nokia Mobile Phones (NMP) and VTT Microelectronics. Papers III–V emanate from cooperation with Temex Microsonics (now TEMEX), Sophia-Antipolis, France and GVR Trade SA, Bevaix, Switzerland. Work published in Paper VI was conducted in collaboration with Micronas Semiconductor SA, Bevaix, Switzerland.

The author has substantially contributed to the research reported in Papers I–VI. He has mainly written manuscripts for Papers I–V, and written essential parts of Paper VI. He is one of the two persons who implemented the computer program used for simulations discussed in Paper I. All the numerical simulations in Papers I and III were carried out by him, and he actively participated in the computation of the results in Papers II and VI. The author has also been strongly involved in the analysis of the results reported in all these papers. He has designed the surface acoustic wave filter reported in Paper IV, and has been actively involved in the design of the filters reported in Papers III and V. Most of the results in Papers I–VI have also been presented in international conferences by the author and collaborators.

List of abbreviations

The following abbreviations are used in the overview:

BAW	Bulk acoustic wave
BEM	Boundary element method
COM	Coupling of modes
CSP	Chip-size package
DOF	Degree of freedom
EMCC	Electromechanical coupling coefficient
FBAR	Thin-film bulk acoustic wave resonator
FE	Finite-element
FEM	Finite element method
IDT	Interdigital transducer
IL	Insertion loss
ISM	Industrial-scientific-medical
LLSAW	Longitudinal leaky surface acoustic wave
LSAW	Leaky surface acoustic wave
LTCC	Low-temperature co-fired ceramic
RF	Radio frequency
SAW	Surface acoustic wave
SMD	Surface mounted device
SMR	Solidly mounted resonator
TCF	Temperature coefficient of frequency
TE	Thickness extensional
TS	Thickness shear
US PCS	Personal communication services cell phone system in the United States
WLAN	Wireless local area network

Contents

1 Introduction

Acoustic waves in elastic solids are utilised in numerous applications in signal processing, including frequency generation, control and filtering in modern wireless communication systems [1–3]. Continuing expansion of telecommunication demands higher operating frequencies and larger bandwidths to enable enhanced data transmission capabilities and to accommodate a larger number of users. The Bluetooth system operating at 2.45 GHz and wireless local area networks (WLAN) operating at 5-6 GHz [4] are prominent examples of relatively recent systems. Resonators and bandpass filters based on bulk acoustic waves (BAW) and surface acoustic waves (SAW) are extensively used in wireless applications such as cellular phones, data communication, navigation, pager and satellite communication, as they often feature superior performance in comparison to competing technologies [5]. The physical phenomenon underlying the operation of BAW and SAW devices is the piezoelectricity [6]. In piezoelectric materials the electric and mechanical fields are coupled, enabling the excitation of acoustic waves by electric fields. Since the velocity of acoustic waves in elastic solids is generally five orders of magnitude lower than that of the electromagnetic waves, the dimensions of the acoustic wave devices may, in principle, be made in the same proportion smaller than devices directly employing the electromagnetic waves, e.g., ceramic filters. Hence, microwave acoustic resonators and filters decrease the surface area on the printed circuit board needed for the frequency filtering functions, and also enable small component heights. In addition, acoustic wave devices are reliable, mechanically robust, provide excellent filter selectivity and usually require no trimming. The components are highly reproducible and may be mass produced using the standard fabrication processes employed in the manufacture of integrated circuits. This serves to satisfy one of the most important requirements set for the component in consumer applications, that is, a low cost.

The unifying theme linking all the Papers in this Thesis together is the strive towards higher operating frequencies for bandpass filters based on acoustic waves. Here, we consider numerical modeling and analysis of both thin-film bulk acoustic wave resonators (FBARs) [7, 8] and SAW resonators [9–12]. Suitable electrical interconnection of individual resonators allows one to synthesize bandpass filters.

The rapid dissemination of the wireless communication applications that took place in the last decade has created a renaissance in the SAW and BAW filter technology. The requirements the mobile systems pose on the radio-frequency (RF) filters are rather distinct from those set on filters in earlier applications, e.g., on SAW filters for television sets [13]. In addition to a high center frequency, wide bandwidth and small size, wireless applications demand a low insertion loss (IL). Mobile terminals have only limited power available, furnished by the battery. Therefore, to extend the battery lifetime, small power consumption is desirable. For RF filters used in the transmission path, this necessitates a low IL in the passband. For instance, in a filter with a 3 dB IL already half of the power is lost. Therefore, even lower IL values are

pursued. In the reception path, a low IL of the RF filter increases the sensitivity and signal quality. Resonator-type filters [14], such as ladder filters, dual mode filters or coupled resonator filters have emerged as solutions to meet the challenge of low IL and they serve as key components in the RF sections of modern mobile communication equipment. When the filter may be considered to be formed of a cascade connection of basic blocks consisting of one resonator connected electrically in series and another resonator connected in parallel, the filter is called a ladder filter. All the filters studied in this Thesis are ladder filters. The resonators constituting the ladder filter may be implemented using either bulk or surface acoustic waves, as the electrical responses of the two are similar.

In the FBARs, studied in Papers I–II, the operating frequency is governed through the wave velocities in the thin film materials layers composing the device and through the layer thicknesses. In fabrication of FBARs, the submicron manufacturing techniques required for SAW devices are not necessary. The operating frequency is controlled primarily through the thickness of the piezoelectric film: the operating frequency increases with decreasing film thickness. The first composite FBARs were reported in the beginning of the 1980s [7, 8], but FBAR filters have only recently been applied in high-volume commercial applications [15]. The appearance of FBAR devices on the market has been delayed by several technological challenges, such as reproducible fabrication of high-quality piezoelectric thin-films by sputtering, and difficulties in obtaining high thickness uniformity of the film throughout the wafer. Furthermore, the design of resonators with clean frequency response, free from spurious resonances, is required. Analysis and design of FBARs demands accurate and reliable modeling. In this work, the finite element method (FEM) [16, 17] is chosen for the modeling task. FEM is a flexible method capable of modeling complicated device geometries, nonuniform materials properties and quite general boundary conditions. In Paper I, FEM-based software customized to model FBARs is introduced. The tool employs sophisticated numerical methods to enable computationally efficient and economic FEM simulations of FBARs. In the interest of modeling accuracy, comparison of results computed using 2D and 3D FEM models is carried out. In particular, the 3D FEM modeling is applied to investigating the effects of the top electrode shape of an FBAR on the behaviour of the spurious resonances. The modeling is validated through comparing the computed vibration amplitude profiles at several frequencies with those measured from the surface of the top electrode using a laser interferometer.

The quality of a sputtered piezoelectric material, such as zinc oxide (ZnO), depends strongly on the sputtering conditions, e.g., temperature and pressure [18]. Hence, the materials parameters of the thin-film are different from those of bulk material and they may vary considerably between different process runs. For proper dimensioning of the layer of piezoelectric material in the FBAR it is necessary to know the acoustic velocity in the material, which depends on the materials constants. Using the actual measured materials constants in modeling—instead of values published

in literature—provides more accurate modeling results. In addition, the materials parameters may be used to assess the quality of the thin film. Consequently, the task of the determination of materials constants for materials in thin-film form arises. In Paper II, a method for estimating the materials parameters of the piezoelectric thin-film material (ZnO) in an FBAR is proposed. The technique is based on fitting the measured and computed dispersion curves of Lamb-wave modes propagating along the layered resonator structure.

Surface acoustic waves propagate along the surface of an elastic half-space [19]. The energy of the SAW is confined into the vicinity of the substrate surface [20]. In SAW devices, the wave is excited using an interdigital transducer (IDT), first described by White and Voltmer [21], which is essentially a periodic system of interleaved metal electrodes deposited on the surface of a piezoelectric substrate. The resolution of the optical lithography sets the technological upper limit for the fundamental operating frequency of SAW devices. The lowest linewidths achievable using conventional optical lithography used in the mass fabrication of SAW devices today are close to 250 nm[1] [22]. The operating frequency of a SAW device (f_0) is to first order proportional to the velocity of the SAW (v) and inversely proportional to the wavelength of the SAW (λ): $f_0 = v/\lambda$. In low-loss SAW filters for frequencies above 0.5 GHz, the leaky SAW (LSAW) mode on lithium tantalate ($LiTaO_3$) and lithium niobate ($LiNbO_3$) substrates is commonly employed. The phase velocity of the leaky SAW is between those of the slow shear and fast shear bulk waves. For example, the velocity of LSAW under a periodic aluminum electrode array with a normalized thickness[2] of 3% on the 36°YX-cut $LiTaO_3$ substrate is about 4100 m/s [23]. This implies that, in principle, LSAW would enable fundamental mode filters with center frequencies slightly over 4 GHz. Utilisation of the leaky SAW mode at higher frequencies necessitates fabrication techniques that are not suitable for economic large-scale production, such as electron beam lithography [24]. Therefore, wave modes with higher velocities than the ordinary leaky SAW mode are actively explored.

To obtain high-velocity SAW modes, layered configurations may be employed. They consist of a piezoelectric layer fabricated atop a substrate supporting a wave with comparatively high propagation velocity. Materials with high acoustic wave velocity include, e.g., sapphire, diamond and silicon carbide. However, these materials are all nonpiezoelectric. For the electrical excitation of the wave, a piezoelectric thin film, such as ZnO, may be deposited on the substrate. Several authors have recently investigated such configurations [25–28]. In addition to the high SAW velocity, the layered configurations enable temperature compensation [29], when the temperature coefficient of frequency (TCF) for the thin film and that for the substrate have opposite signs. However, thin films fabricated using sputtering are polycrystalline. The

[1] In the commonly employed IDT used to generate the SAW, there are two fingers per electrical period, resulting in a SAW wavelength 1 μm for linewidth 0.25 μm.

[2] The normalized thickness is defined as $h/(2p) = h/\lambda_0$, where h is the absolute electrode thickness and $2p = \lambda_0$ is the electrical period of the grating (see Fig. 3.3).

propagation loss of the SAW in a polycrystalline material tends to be higher than that in a monocrystalline bulk material. The surface-wave properties, such as the phase velocity and coupling coefficient, are sensitive to the thickness of the thin film which, consequently, needs to be precisely controlled.

Here, we consider a high-velocity SAW mode on a monocrystalline substrate, viz. a longitudinal leaky SAW (LLSAW) [30, 31]. The velocity of the LLSAW is larger than those of the shear bulk waves and slightly lower than the velocity of the longitudinal bulk wave. The LLSAW exists in certain highly anisotropic crystal materials, e.g., lithium tetraborate ($Li_2B_4O_7$) [32]. In $LiTaO_3$ and $LiNbO_3$ substrates, the LLSAW mode with low propagation loss exists only when a periodic grating of relatively thick electrodes is present on the substrate surface [33]. The fabrication of LLSAW devices requires only deposition of the metal electrodes on the substrate surface and, hence, fabrication is simpler than that of the layered configurations. In addition, the inherent losses in monocrystalline material are low. In this Thesis, LLSAW mode on YZ-cut of $LiNbO_3$ substrate is considered [34]. This wave mode, investigated in Papers III–V, is suitable for implementing high-frequency filters because of its high phase velocity of about 6100 m/s under a periodic grating of aluminum (Al) electrodes with a normalized thickness of h/λ_0 close to 8%.

For the utilisation of LLSAW in filter applications it is necessary to know the dependence of LLSAW propagation properties under a periodic Al grating. In Paper III, the dependence of the phase velocity and propagation loss (or Q value) on the dimensions of the Al electrodes is investigated in detail, both theoretically and experimentally. Paper IV is the first one to report a ladder-type bandpass filter based on LLSAW mode on YZ-$LiNbO_3$ substrate. The center frequency of the filter is in the 2.5 GHz frequency range and it proves the concept of using LLSAW to implement wide-band high-frequency filters. In Paper V, a unique filter with center frequency as high as 5.2 GHz is presented, demonstrating that the LLSAW mode may be applied to fabricate filters for the wireless local area network (WLAN), operating at frequencies above 5 GHz, using conventional optical lithography. The resonators comprising the filter employ the fundamental LLSAW mode. With the critical dimension within the IDT (smallest width of electrodes or the gaps between them) being about 290 nm, the optical lithography is approaching its technological limits.

As the frequencies increase, proper design of the layout for the metallizations on the substrate (chip) as well as in the package enclosing the chip become increasingly important. At high frequencies, the effects of the parasitic capacitive and inductive couplings and resistive losses on the electrical frequency response of the device become pronounced. Accurate modeling techniques are needed to predict these effects such that the demanding specifications set for the performance of the filter can be met. To reliably predict the transmission response of a packaged SAW filter, both the package effects and the acoustics of the SAW chip inside need to be considered in the modeling [35, 36]. Such a comprehensive approach to filter modeling including

electroacoustic and electromagnetic modeling is pursued in Paper VI. In particular, numerical modeling of the parasitic electromagnetic couplings in a ceramic package of a SAW ladder filter is demonstrated. Moreover, detrimental acoustic effects occurring in the SAW resonators of the ladder filter are considered, as these effects may cause additional acoustic losses and thus deteriorate the filter performance. Software capable of modeling these 3D acoustic effects is presently not commonly available. This promotes the importance of the possibility to directly measure the acoustic phenomena from the surface of the device, e.g., by using laser interferometry. The laser-interferometric technique is amenable for the measuring task since it is a noninvasive, non-contact method which does not disturb the acoustic field being measured [37]. In Paper VI, plots of the acoustic vibration amplitude measured from a SAW duplexer filter are presented.

This overview consists of five Chapters. Chapter 2 considers thin-film bulk acoustic wave resonators and their modeling using the finite element method. Phenomena relevant to FBAR operation, such as Lamb-wave propagation in layered structures, energy trapping and spurious modes are discussed. Moreover, a method for the determination of materials parameters for thin films, based on fitting the computed and measured Lamb-wave dispersion curves, is presented. Chapter 3 builds upon author's research work on longitudinal leaky surface acoustic waves and on ladder filters based on this wave mode. Chapter 4 concentrates on numerical simulations carried out to estimate the influence of packaging on the transmission response of a SAW duplexer filter. Furthermore, results of laser-interferometric investigations of the acoustic vibration amplitude in the SAW filter are presented. Chapter 5 provides a summary and conclusions.

2 Modeling composite thin-film bulk acoustic wave resonators

In this Chapter, the structure and operation of FBARs are discussed and the author's work focusing on their modeling using the finite element method (FEM) is reviewed. The implemented FEM simulation tool is presented and its applicability to FBAR modeling is demonstrated (Paper I). FEM simulations are used to demonstrate energy trapping behaviour and spurious anharmonic resonance modes in FBARs. At the end of the Chapter, a numerical technique for computation of dispersion curves of Lamb-wave modes [38, 39] propagating in stratified structures, such as FBARs, is described. The computational method is applied in Paper II, where an approach for determining the material constants of thin-film materials is demonstrated.

2.1 Thin-film bulk acoustic wave resonators (FBARs)

The operation principle of FBARs is the same as in quartz resonators [40], which have been used in applications of frequency generation, control and selection from the beginning of the 1920s [41]. A bridge-type FBAR is presented schematically in Fig. 2.1, comprising a layer of piezoelectric material between the top and bottom electrodes and a support layer below the bottom electrode. For the moment, let us consider a simpler idealistic model, consisting only of a plate of piezoelectric material, infinite in lateral dimensions. Infinitely thin metallisations both on the upper and lower surfaces of the plate constitute the top and bottom electrodes. Connecting driving alternating voltage across the top and bottom electrodes creates an electric field in the thickness direction within the piezoelectric material. Because of the converse piezoelectric effect [6] the electric field causes strains in the piezoelectric material thereby exiting mechanical vibration. Hence, the voltage excites a bulk acoustic wave within the plate. The bulk plane wave propagating in the direction perpendicular to the plate (in thickness direction) reflects from the upper and lower surfaces. At frequencies where the thickness contains an integral number of half wavelengths, a standing wave is formed and resonance occurs. The modes with an even number of half wavelengths in the thickness direction may not be electrically excited. The resonance, where the thickness of the piezoelectric plate equals half a wavelength of the bulk wave, is called the fundamental resonance. At the resonance frequency the magnitude of the input electric admittance attains a high value and exhibits a strong peak (see Fig. 2.5). For a sufficiently strong resonance, the electric impedance changes at the resonance frequency from capacitive to inductive (reactance becomes a positive quantity). The resonance frequency may be taken to be either the frequency of maximum magnitude of admittance, the frequency of maximum conductance (real part of admittance) or the frequency of the zero crossing of susceptance (imaginary part of admittance). For a resonator with a high figure of merit, say >10, all these frequencies are practically equal [40]. This frequency is the series resonance frequency, f_s, corresponding

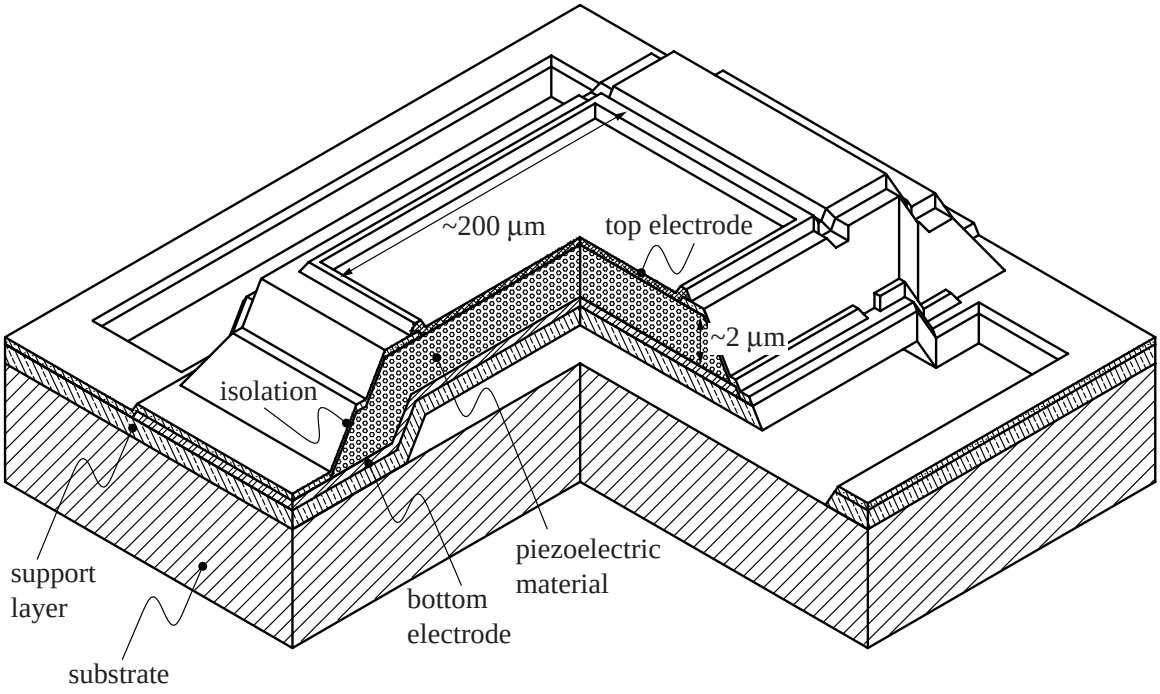

Figure 2.1: Bridge-type thin-film bulk acoustic wave resonator. In actual resonators, the lateral dimensions are much larger than the thickness of the resonator; the dimensions have been scaled here for clarity. The hatching indicates faces that have been cut to create the cutaway view.

to the natural vibration mode of the plate under short-circuited electrodes [40, 42], i.e., under circumstances where the potential on each electrode is fixed. At some higher frequency, the magnitude of admittance attains low values and the impedance changes again from inductive to capacitive. Again, the resonance frequency may be defined either as the minimum of magnitude of admittance or as the frequency of the zero crossing of susceptance. This frequency is called antiresonance or parallel resonance frequency, f_p. It corresponds to the natural vibration mode of the plate under the open circuited electrodes [40, 42, 43], i.e., the case where the total charge on each electrode is fixed. The frequency separation between the resonance and antiresonance frequencies depends on the piezoelectric material as well as the device configuration, strongly piezoelectric materials having a larger frequency separation.

A characteristic parameter used as a measure for the performance of the piezoelectric resonator is the electromechanical coupling coefficient (EMCC). There are several ways of defining the EMCC [6, 44]. A definition suitable for describing the piezoelectricity of the material (strongly piezoelectric materials possess higher EMCC) may not be appropriate for describing the resonator performance. A definition convenient for experimental work is the effective coupling coefficient expressed as [45]

$$k_{\text{eff}}^2 = \frac{f_p^2 - f_s^2}{f_p^2} \ . \tag{2.1}$$

Here, f_s and f_p are the resonance and antiresonance frequencies, respectively. As the bandwidth of a ladder filter is predominantly determined by the frequency separation between the resonance and antiresonance (resonance–antiresonance distance) of the resonators used in the construction of the filter, k_{eff} describes the utility of the resonator in filter applications with respect to the achievable filter bandwidth.

Traditional thickness-mode quartz resonators are fabricated through thinning a bulk material into appropriate thickness by lapping and polishing procedures [40] to achieve the targeted operating frequency. Very low thicknesses needed for fundamental-mode high-frequency operation cannot be fabricated this way, as thin wafers are mechanically fragile. Composite thin-film bulk acoustic wave resonators have emerged as a way to achieve high-frequency fundamental-mode operation. In FBARs, the electrodes and the piezoelectric material are fabricated atop a substrate material using standard photolithographic, sputtering and etching techniques. FBARs permit the use of low-cost silicon substrates. The first FBARs [7, 8] were fabricated through etching the bulk silicon from the back side of the substrate to form the thin membrane. This method yields fragile wafers and the number of components on the wafer is limited. These problems are alleviated if an etching technique producing vias with walls perpendicular to the plane of the substrate is used [46]. In a technique described by Kline and Lakin [47], the membrane is formed through etching the bulk material away beneath the sputtered layers from the top side of the substrate. The resulting ditch forms the air gap between the membrane and bulk material. In a third technique, a sacrificial layer is first deposited on the substrate surface and the remaining layers are fabricated atop the sacrificial layer [48, 49]. The air gap is then formed via etching the sacrificial layer away. In the membrane-type FBARs, the residual stresses in the thin-film layers need to be controlled [50], because too large stresses may either break the membrane after it has been released or bring it into contact with the substrate, thereby destroying the electrical response of the resonator [51].

In the mid-1990s, Lakin *et al.* [52] introduced the acoustic mirror, originally described by Newell [53], into the FBARs. FBARs of this type are termed solidly mounted resonators (SMR). In SMR, the acoustic isolation between the resonator and the bulk material is achieved using a Bragg-type reflector consisting of layers with alternately distinctly different acoustic impedances. Choosing the layer thicknesses appropriately, this kind of an acoustic mirror reflects the bulk wave and prevents the acoustic energy from escaping into the solid. The mirror operates efficiently only for the desired wave mode in a limited frequency range. This is an advantage, as it decreases the quality (Q) factors associated with higher harmonics in the resonator response. The residual stresses in thin-film layers for SMR are not as critical as those for membrane type FBARs, as long as the stresses are not high enough to break the adhesion between the layers. It is also known that the spurious mode content for SMR is lower than that for membrane-type FBARs [54]. The resonators studied in

Papers I and II are mainly of SMR type.

The thin-film piezoelectric material layers are commonly fabricated with sputtering. The properties of the thin film are sensitive to the substrate material and sputtering parameters, such as pressure, temperature, power, and gas composition and flow [18, 55]. These parameters need to be adjusted carefully to obtain a high-quality piezoelectric film with a high effective coupling coefficient. The maximum attainable effective coupling coefficient is dictated chiefly by the crystal properties of the piezoelectric layer, such as preferred orientation, texture and grain size. Aluminum nitride (AlN) was one of the first materials fabricated in thin-film form. However, it is only recently that the fabrication technique has reached a level of sophistication high enough to enable large-scale production of FBARs for applications in mobile communication systems [15]. Another widely used material for FBARs is ZnO [8, 56, 57]. In fabrication, the thicknesses of the top electrode, bottom electrode, and the piezoelectric material layer need to be controlled precisely to obtain the correct resonator operating frequency [58]. The thicknesses and materials properties of the layers should be constant over the whole wafer area to obtain high fabrication yield. In practice this is difficult to attain and, therefore, trimming to correct operation frequency may be necessary by selective thickening or thinning of the resonators.

The number of materials currently available for use as the thin-film piezoelectric layer material is rather limited. Although a certain material may be available in bulk form (e.g., as wafers to be used as the substrate material for SAW devices), its fabrication in thin-film form using sputter deposition may not yet be mastered. For example, attempts have been made to fabricate $KNbO_3$ thin films [51]. The interest in this material derives from its high effective coupling coefficient; the value 46.8% has been quoted for bulk $KNbO_3$ [51]. However, the thin-film $KNbO_3$ reported in [51] suffered from low effective coupling coefficient and low Q value (high losses). Hence, further development is still required to achieve adequate material quality allowing FBAR applications based on $KNbO_3$.

Appealing features of the FBARs are, for example, the possibility to obtain high operating frequency through decreasing the thin-film thickness and the possibility to adjust the coupling coefficient and temperature behaviour. The effective coupling coefficient for a resonator depends not on only on the properties of the piezoelectric thin film, but also on the other materials layers in the resonator, e.g., the top and bottom electrodes. The electrodes affect the profile of the displacement field within the piezoelectric layer. This may accomplish a closer match between the driving electric field profile and the displacement profile, resulting in an increase in the effective coupling coefficient [59]. Theoretical values 7.5% and 6.0% for the coupling coefficient[3] have been reported for the two commonly used materials ZnO and AlN, respectively [60]. However, if a coupling coefficient lower than this is desired, it may be obtained through varying the proportion of the thickness of the piezoelectric layer

[3]Definition $k^2_{\text{eff}} = \phi/tan(\phi)$, where $\phi = 1.571 f_s/f_p$ is used in [60].

to the total thickness of the resonator. This way, the ratio of the acoustic energy within the active piezoelectric film to the total acoustic energy within the composite resonator is reduced, resulting in corresponding decrease of the effective coupling coefficient. This is the reason why membrane-type FBARs commonly feature slightly higher values of k_{eff} than SMRs. The temperature characteristics may be engineered to improve temperature stability by proper selection of the materials in the composite resonator. For example, if the piezoelectric film material is AlN or ZnO with a negative temperature coefficient of frequency (TCF), a material with a positive TCF, such as SiO_2, may be used close to the piezoelectric film [61, 62]. FBARs with TCF close to zero have been reported in numerous papers [59, 63–65]. FBARs also have the potential to be integrated on the same chip with active microwave devices [66].

One of the first consumer applications of FBAR-based filters was for the personal communication services cell phone system in the United States (US PCS) [15, 67]. In this application, the FBAR filters can challenge the SAW filters, because the latter have difficulties to fulfill the required electrical performance. Because of the need for efficient use of frequencies, owing to increasing crowding of RF spectrum, the frequency bands allocated for transmission and reception in a wireless communication system may be very close to each other. This is the case for US PCS, where the transmission and reception bands extend from 1850 MHz to 1910 MHz and from 1930 MHz to 1990 MHz, respectively [68]. The US PCS system presents one of the most demanding specifications. Leaky SAW on $LiTaO_3$ or $LiNbO_3$ substrate has too high a TCF such that the frequency variation in the filter passband with temperature is too high to meet the specification of 20 MHz (1%) guard band between the transmission and reception bands. The total frequency variation is a sum of the frequency variations due to temperature changes and manufacturing tolerances. FBARs typically possess lower TCFs and higher Q values than SAW resonators and, consequently, they enable filters with lower frequency drift and steeper skirts (or narrower transition bands) than filters based on SAW resonators. High Q values of the FBARs also transform to low ILs of the filters. For example, in [69] an FBAR duplexer for US PCS achieves a minimum IL of 1 dB in the transmission band.

2.2 Modeling FBARs with the finite element method (FEM)

The goal of the research reported in Paper I was to implement a software tool for accurate modeling of FBARs to be used as an aid in design and analysis of actual components. Furthermore, the aim was to study the dependence of the spurious mode content on the resonator geometry, in particular, on the shape of the top electrode. The presence of spurious resonances in the resonator response may cause ripples in the passband of a filter [70, 71]. For numerical modeling of FBARs, tailored FEM software was created (Paper I, see also [72]). In the implementation, the objective was efficiency in memory management and solution algorithms.

In the modeling of quartz resonators, so-called plate theories have been widely

used [73, 74]. They use an ansatz for the functional form of the variation of the displacements and potential in the thickness direction of the quartz plate, such as power series expansion [73] or harmonic series expansion [74]. This serves to derive simplified approximate equations from the full set of equations required for an exact solution. In the traditional quartz resonators, the electrodes are thin in comparison with the thickness of the quartz. This allows modeling the effect of the electrodes as a mere mass load [74]. However, in FBARs the electrode thicknesses are comparable to that of the piezoelectric thin film. In addition, the resonator is usually composed of several additional material layers, e.g., a support layer below the bottom electrode in membrane type FBARs[4] and the acoustic mirror in SMR. Although the composite structure complicates the application of the plate theory modeling approach to FBARs, extensions of the plate theory to model FBARs have been reported, e.g., in [77]. Other modeling approaches include the mode-matching method [78, 79] and the finite-difference method [80–82]. In the mode-matching method, applied by Milsom *et al.* [83, 84], the resonator structure is subdivided into regions such that each region is uniform in lateral direction. The displacements and potential are expanded as a sum of the Lamb-wave modes within each region. Approximate interface conditions, e.g., continuity of the dominant Fourier harmonics of displacements across the region boundaries are imposed to solve the unknown coefficients for the Lamb-wave modes. Lakin *et al.* [85–87] have reported the usage of the finite-difference frequency-domain technique in the modeling of FBARs.

The materials parameters and device geometry determine the performance of the thin-film BAW resonator. In actual resonators, several of the material layers are patterned such that the structure is not uniform in lateral direction but features several discontinuities. The fabrication process of FBARs with sputtering and standard photolithographic techniques may result in spatial variations in the materials parameters. It is usual that the properties of the piezoelectric material are different close to the material onto which the thin-film layer is fabricated from the properties farther away from the interface [88, 89]. Moreover, the actual fabricated device may suffer from imperfections, such as variations in layer thicknesses and rough interfaces between the different materials. There may also be effects arising from the geometry of the device, such as the spurious resonances resulting from the occurrence of standing Lamb waves on the top electrode region. All these factors may affect the resonator behaviour and need to be taken into account in the modeling. Simulation of those effects which are inherently a result of the variations present in the lateral direction requires 2D or 3D models. Evidently, a highly flexible method is demanded for the modeling task. Here, the finite element method (FEM) has been chosen because it is powerful enough to take into account all these phenomena.

The FEM is a standard numerical method widely used in the field of structural

[4] AlN is mechanically so strong that the support layer is not necessary [75]. Such a self-supported FBAR with ZnO as the piezoelectric film has also been recently demonstrated [76].

mechanics [16, 17]. The classic paper on applying FEM to problems involving piezoelectric materials is by Allik and Hughes [90]. They apply FEM to numerically solve the governing and constitutive equations for linear piezoelectric media. These equations may be derived from Hamilton's principle for the linear piezoelectric continuum [91–93]. The problem is a coupled-field problem, as the mechanical and electrical quantities are interwined. Hamilton's principle is also taken as a basis for the derivation of many approximate formulations, e.g., the plate theories already mentioned above. The FEM may be utilized for numerical solution equally well within the framework of these approximate formulations, such as in the case of the laminated plate theory [94].

In FEM, the complete problem domain is discretized. This implies that FEM encounters inherent difficulties in dealing with open boundary field problems, as the problem domain needs to be truncated to keep the problem size finite. Truncation inevitably introduces an artificial boundary and, consequently, a modeling error resulting from an approximation of the boundary conditions at this boundary. Considering acoustic waves, the truncation of the model causes reflections of the wave from the artificial boundaries. Placing infinite elements along the artificial boundary on the side of the continuum has been suggested as one solution to this problem [95–97]. The infinite elements strive to implement an ideal absorbing boundary condition, such that a wave incident on the boundary would not reflect back. Instead of infinite elements, one may simply introduce regions at the boundaries of the model where the attenuation of the material increases from zero to a given finite value [98]. Since the increase of the attenuation is gradual, there is no abrupt change in the materials properties which would give rise to reflections of the wave. With a sufficiently high attenuation, the amplitude of the wave entering the region will decay rapidly such that there is no reflection. This solution has the benefit that it can be readily applied without any need for special FEM elements.

One possible solution is to combine FEM with another method which is used to model the semi-infinite region. An example of such a modeling technique is the FEM/boundary-element-method (BEM) formalism [99–103], which is used in the modeling of surface-acoustic wave devices. For example, [102] and [103] report software utilizing the combined FEM/BEM approach, capable of 3D modeling of biperiodic configurations. The FEM/BEM formalism is further discussed in Chapter 3.

FEM has been used extensively in numerical modeling of piezoelectric devices [43, 104, 105], including ultrasound transducers [102, 106], quartz resonators [107], surface acoustic wave devices [42, 108–111] and delay lines [112]. In Paper I, FEM is applied to modeling of FBARs. To minimize the losses in the FBAR, the energy needs to be well confined into the resonator such that as small a fraction as possible of the acoustic energy escapes from the active resonator volume. If high energy confinement is achieved, the amplitudes of the waves outside the active resonator region are small compared to those of the waves inside, and simply setting the displacements to

vanish at the model boundary located sufficiently far from the active region is a fair approximation. When present, waves radiating into the bulk may cause a standing wave once they reflect from artificial boundaries. This may be seen as a resonance peak in the modeled electrical response. In case damping regions cannot be used to suppress artificial reflections, the boundaries of the simulated volume should, if possible, be chosen such that resonance peaks induced by the boundaries occur outside the frequency range of interest [72].

In a FEM mesh, each node point is connected only to a limited number of other nearby located nodes. The benefit of this local connectivity is that the FEM matrices (system matrices) which describe the complete modeled system, have a banded structure. The pertinent system matrices are the electromechanical stiffness matrix K and mass matrix M. In particular, since FBARs are wide and thin structures, 2D FBAR models result in narrow numerical bandwidth of the system matrices. In each node point of the FEM mesh, four field variables are considered, i.e., the three components of displacement and the electric potential. The values of the fields at a node point are the unknowns or degrees of freedom (DOFs) which are finally solved from the FEM equations. In the FEM software implemented in this Thesis, prior to the optimization of the DOF ordering discussed below, preliminary ordering of the DOFs is used where each node corresponds to four consecutive columns and rows in the system matrices [113]. Hence, the K and M matrices are composed of 4×4 submatrices. Both the K and the M matrices are symmetric. Hence, it suffices to store the matrix elements on each column of the matrix starting from the element on the diagonal until the last nonzero element above the diagonal element. This is the skyline matrix storage scheme, which is used to store the electromechanical stiffness matrix (K matrix). However, for the mass matrix, only three diagonal elements of each 4×4 submatrix are nonvanishing [114], because there is no mass associated with the electric DOFs. Therefore, in the software, this specific structure of the mass matrix is taken into account such that only the three nonvanishing elements of each 4×4 submatrix are stored.

The original node numbering in the FEM mesh may not be optimal with respect to the resulting matrix bandwidth or matrix profile (number of elements within the skyline, i.e., number of matrix elements that need to be stored). Therefore, the software uses the Gibbs-King algorithm [115] to optimize the node numbering such that the matrix profile is minimized. The substantial reduction in the skyline of the stiffness matrix for a 3D finite-element (FE) model achieved by applying the Gibbs-King algorithm to optimize the node numbering is displayed in Fig. 2.2. In addition to the optimization of the node numbering, also the numbering of the DOFs may be optimized to decrease the matrix profile. Optimization of the node and DOF numbering is especially important for 3D FE models to avoid unacceptably high computational cost. The decrease in the number of stored matrix elements also reduces the computation time.

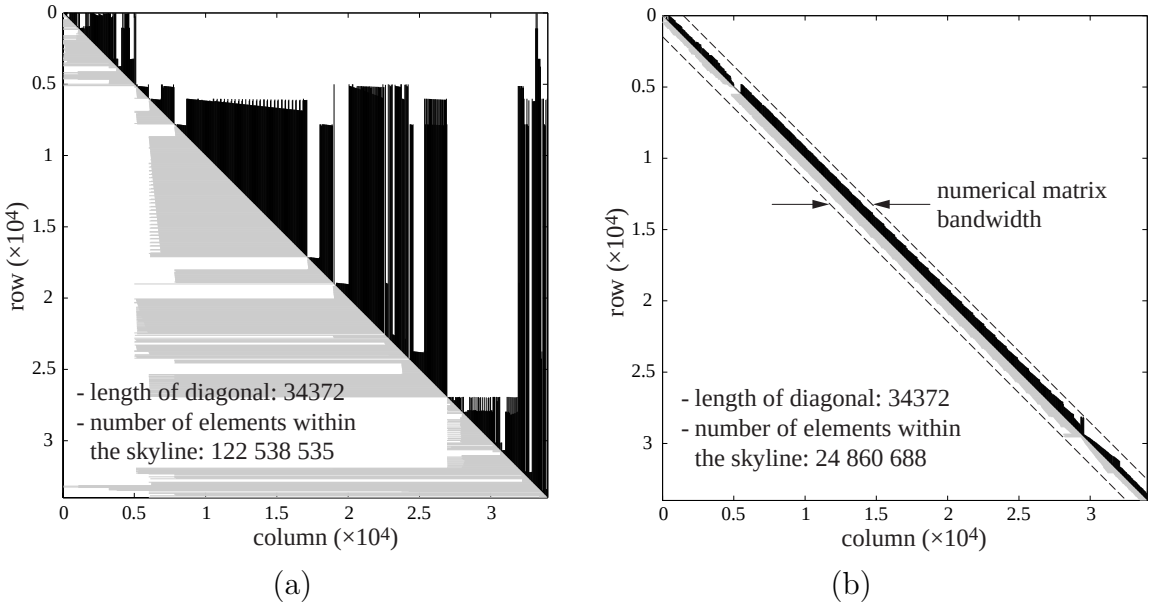

Figure 2.2: Skyline of the electromechanical stiffness matrix before (a) and after (b) the optimization of the numbering of the nodes in the FEM mesh with the Gibbs-King algorithm (for a 3D FE model). The matrix elements stored in memory are drawn in black.

In the FEM simulations of FBARs covered in this work, a modal analysis approach [116, 117] was used extensively. In the modal analysis, the eigenproblem resulting from the FEM formulation is solved for the frequencies of the vibration modes (eigenfrequencies) and for their mode shapes (eigenvectors). In the solution of the eigenproblem, the Lanczos spectral transformation method is used to compute specified number of eigenvectors whose eigenvalues are in the vicinity of a specified frequency. The advantage of the method is that it retains the structure of the K matrix. The algorithm is available in the numerical subroutine library ARPACK [118]. The method is efficient for problems which have small numerical bandwidths of the coefficient matrix [113]. If damping is taken into account in the modeling, it leads to a complex-valued eigenproblem. However, in the present version of the FEM software only real-valued generalized eigenproblems are implemented and, hence, the abovementioned damping region to suppress the reflection of the waves at the artificial boundaries was not used.

The implemented FEM software can also solve the field problem, where the response of the structure to time harmonic (i.e., sinusoidally varying) loading is computed (harmonic analysis). In harmonic analysis, the damping can be taken into account, since a solver for complex-valued linear systems of equations is included into the FEM software tool. However, the modal analysis approach was favored in the computations carried out in Paper I since solving the electric admittance of the modeled resonator as a function of frequency with a sufficiently high frequency resolution,

using harmonic analysis, was found to be slower than solving the eigenvalue problem within the frequency range of interest. This is partly because a direct solver is used in harmonic analysis, whereas the modified Lanczos algorithm is iterative. Based on the modal analysis results, i.e., the resonance frequencies, mode shapes, and strengths of excitation of each mode, the electric admittance and mechanical displacements as functions of frequency may be evaluated [72, 116].

The main features of the FEM software (called BAWFEM) developed mainly by the author are summarized below.

- 2D elements available:
  - linear (4 node), quadratic (8 node) and cubic (12 node) quadrilateral elements (also axisymmetric versions)
  - linear (3 node) and quadratic (6 node) triangular elements
- 3D elements available: linear (8 node) and quadratic (20 node) brick elements
- displacement, force, surface traction, voltage, charge, charge density and electric displacement loading can be modeled
- sets of nodes with coupled DOFs may be defined (e.g., to impose constant electric potential at all nodes on electrode). This also enables modeling of periodic configurations.
- efficient memory management:
  - skyline matrix storage scheme
  - reorganization of node numbers and/or DOFs using the Gibbs-King algorithm
- modeling spatial variation of materials parameters
- harmonic analysis (local frequency-dependent damping can be modeled)
- modal analysis using Lanczos method for efficient solution of generalized piezoelectric eigenvalue problem in a frequency range of interest
- preprocessing:
  - separate preprocessor program for creation of 2D FEM models has been implemented
  - program for converting 2D and 3D FEM meshes created with preprocessor of a commercial ANSYS FEM software into the format used by the BAWFEM solver has been developed
- postprocessing:
  - programs for visualization of 2D and 3D results have been implemented
  - electrical response and displacements can be computed based on modal analysis results using a separate program

Shortcomings of the BAWFEM software are that material losses cannot be taken into account in modal analysis and the inability to model half-spaces, e.g., substrate onto which the resonator is fabricated. Furthermore, addition of an iterative solver for

harmonic analysis is to be considered in possible further development of the software to reduce the computation time.

In the next Section, the dispersion of Lamb-wave modes in layered plates is considered to lay foundation for discussion on the energy trapping and spurious modes. These concepts are useful in the description of the characteristics of FBARs.

2.3 Propagation of acoustic waves in layered structures

In an anisotropic medium there are, in general, three bulk acoustic wave modes. The modes are classified according to the polarization of the displacement vector associated with the mode. If the dominant component of the displacement is more or less parallel with the propagation direction, the mode is called quasi-longitudinal. The two modes with the dominant component of displacement vector more or less perpendicular to the propagation direction are quasi-shear modes. The shear modes may have different velocities, in which case they are called fast quasi-shear and slow quasi-shear modes. For certain propagation directions the modes may become pure, such that the displacement vector is exactly parallel with or perpendicular to the propagation direction. The polarization vectors of the modes at any given frequency may be solved from the Christoffel equations [119], which are derived from the constitutive equations for piezoelectric media, equations of motion and Maxwell's equation under the quasi-static approximation[5].

In an unbounded bulk medium, all the modes may propagate independently at all frequencies. However, once the extent of the medium is limited, e.g., in a half-space or in a layer of finite thickness, in general, the bulk waves may not exist independently. Within the conceptual framework used below to describe the waves, this is because the propagating wave needs to fulfill the boundary conditions on the interface, such as vanishing stress. Therefore, e.g., a wave propagating along a layer of anisotropic material with finite thickness, in general, is composed of partial wave components corresponding to the quasi-longitudinal BAW and to the two quasi-shear BAWs. For a piezoelectric material, an additional electric term is present. The coupling between these partial waves depends on the properties and orientation of the layer material, the propagation direction as well as on the boundary conditions. The waves, presented as a linear combination of the partial waves, may propagate along the layer only with distinct wavelengths at a given frequency. Thus, due to the boundary conditions, a mode structure emerges. These modes propagating along a layered structure are called Lamb waves [20, 38, 39].

The characteristic displacements exhibited by the mode are used to establish the naming convention for the Lamb-wave modes. The x and z-axes are taken to be parallel and perpendicular, respectively, to a layer with infinite extent in x and y-

[5]Because the speed of light is about five orders of magnitude higher than that of acoustic waves, it is a valid approximation to compute the electric field as the negative gradient of the scalar electric potential. This approximation is referred to as the quasi-static approximation.

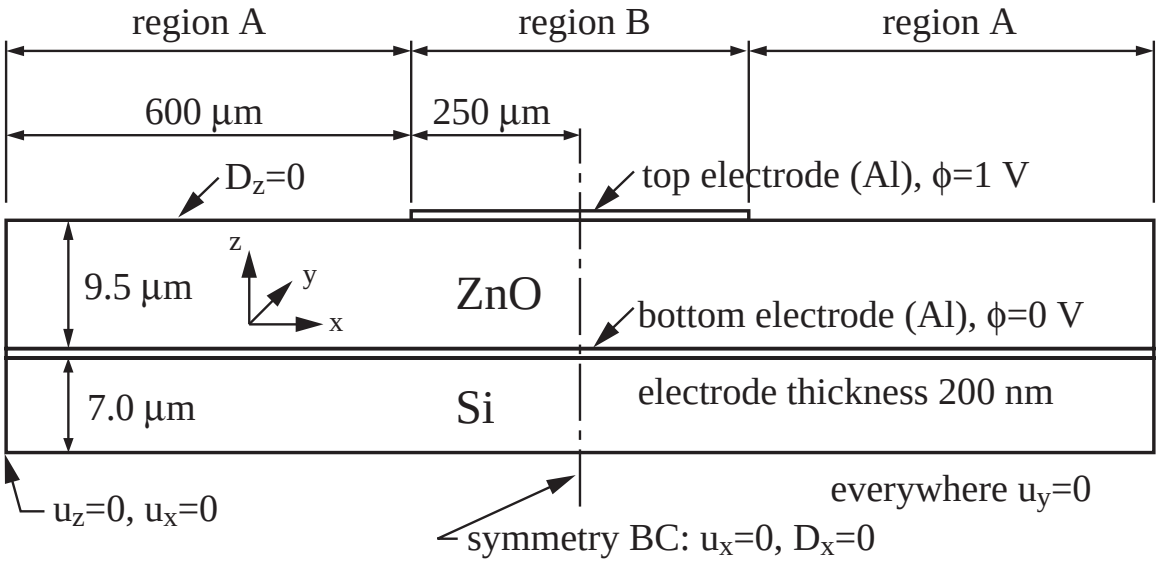

Figure 2.3: Cross section of a membrane-type composite thin-film BAW resonator [84] showing the boundary conditions imposed in the FE model.

directions. Consider the direction of the displacement vector when the wave propagates in the direction perpendicular to the layer (in the thickness or z-direction). Modes which have the dominant displacement component more or less parallel to the z-direction are called thickness extensional modes (TE) and modes which have the dominant displacement component more or less parallel to the x-direction are called thickness shear modes (TS). In addition, the number of half wavelengths (considering the dominant displacement component) in the z-direction determine the order of the mode. For example, for the TEn mode, considering the displacement component in the thickness direction, the plate contains n times $\lambda_t/2$ wavelengths. Here, λ_t denotes the wavelength of the wave propagating in the thickness direction of the plate.

Dispersion relation expresses the dependence of the x-component of the wavevector (wavenumber k_x) on frequency. One often refers to plotted dispersion relations as dispersion curves. Thus, for a given frequency, dispersion curves give the wavenumbers of the Lamb waves that can propagate along the plate. The computation of the dispersion curves is discussed in Section 2.5.

2.4 Energy trapping and spurious anharmonic modes in FBARs

Consider the FBAR model sketched in Fig. 2.3. Region B has a 200 nm thick aluminum layer (top electrode) atop the ZnO, whereas region A is without metallization. The computed dispersion curves for TE1 Lamb wave mode in region A and B are displayed in Fig. 2.4. The curve drawn with dashed line is for region A and that drawn

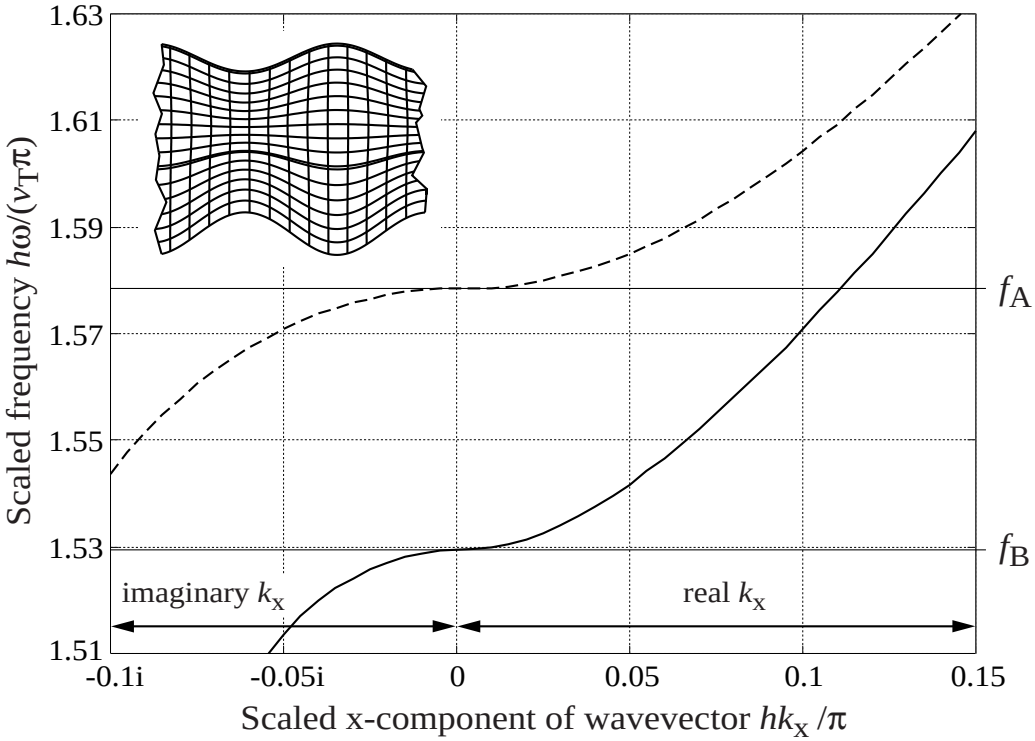

Figure 2.4: Dispersion curves for the TE1 Lamb-wave mode in an infinite Si/Al/ZnO layered plate with (solid) and without (dashed) an Al layer atop the ZnO. Frequency and k_x are expressed in units of $\pi v_T/h$ and π/h, respectively, where h=9.5 μm and v_T=2747 m/s (shear-wave velocity along the crystallographic axis Z in ZnO). The inset illustrates characteristic displacements for the TE1 mode propagating in the infinite plate with an Al layer atop the ZnO.

with solid line is for region B. In both cases the bottom electrode is grounded (set to potential 0 V). In region B, the top electrode is also grounded, i.e., the short-circuited condition is imposed. Imaginary k_x represents non-propagating (evanescent) modes. Hence, below a certain frequency the mode cannot propagate along the plate but, instead, the displacements decay exponentially. This frequency is called the cut-off frequency of the mode. In Fig. 2.4 the cut-off frequencies of the TE1 modes in region A and region B are labeled f_A and f_B, respectively.

Using the dispersion curves, the energy trapping phenomenon may be explained, first discussed for quartz resonators by Shockley *et al.* [120]. If the region B is sufficiently wide, the resonance frequency of the resonator (denoted as f_r) is close to the calculated cut-off frequency for region B (f_B). Then, the resonance frequency is below the cut-off frequency for the region A (f_A) and the TE1 mode cannot propagate in region A. This applies within the frequency range from f_B to f_A. Hence, the wave is confined to the metallized region (region B). This phenomenon is called energy trap-

ping [40, 120, 121]. Above the frequency f_{A}, the wave may propagate in region A and thus it transfers energy away from the metallized region. For a high Q value of the FBAR, it is thus necessary that at the series resonance frequency of the resonator the mode is trapped, such that energy does not escape from the active resonator region which would cause losses.

In the ideal one-dimensional case, where the layered plate constituting the resonator is infinite, it is possible to obtain a clean frequency response free from additional spurious resonance peaks close to the fundamental resonance frequency. However, the actual resonator structures are three-dimensional. The finite size of the electrodes may give rise to spurious resonances contaminating the frequency response close to the fundamental resonance frequency [48, 54, 122–124]. For example, consider the TE1 mode which is the mode employed in the FBARs in Papers I and II. There is a strong discontinuity in the region around the electrode edge, giving rise to mode conversion and wave reflection. These conditions may be described using the mode-matching technique, where the solution is represented as a linear combination of Lamb-wave modes in regions A and B such that the boundary conditions at the edges of the electrode are approximately satisfied [84]. The TE1 mode in region B alone with vanishing x-component of the wavevector, occurring exactly at the cut-off frequency f_{B}, cannot fulfill the boundary condition at the top electrode edge region. The solution inevitably involves waves for which the x-component of the wavevector is nonvanishing, i.e., the wave propagates along the lateral direction. Hence, the presence of the edges generates the TE1 mode (and usually other modes as well) propagating in the lateral direction [125]. Scattering into modes which may propagate outside the metallized region (region A) will increase losses [126]. At certain frequencies, due to the reflections of the TE1 Lamb-wave mode from the electrode edges, it forms a standing wave in the electroded region. These standing-wave modes are termed anharmonic TE1 modes.

The higher-order anharmonic modes have small wavelengths in the lateral direction. Hence, as the electrode effectively integrates the charge density on the electrode associated with the mode [87, 125], the strength of the spurious resonances decreases with increasing order of the anharmonic mode. The admittances computed using a 1D model and 2D and 3D FE models for the resonator in Fig. 2.3 are shown in Fig. 2.5. It can be observed that in the admittance computed using 2D and 3D FE models, spurious resonance peaks due to the anharmonic TE1 modes appear. The 1D model cannot model this inherently 2D effect. The 3D simulation predicts stronger anharmonic resonances and a richer mode spectrum than the 2D simulation. The dispersion curve for the TE1 mode in region B in Fig. 2.4 shows that the wavelength of the mode decreases with increasing frequency. Therefore, the spurious resonance peaks appear above the resonance of the fundamental TE1 mode in frequency.

The symmetry is exploited in the computation and the 2D and 3D FE models comprise only one half and one quarter of the resonator, respectively. The boundary

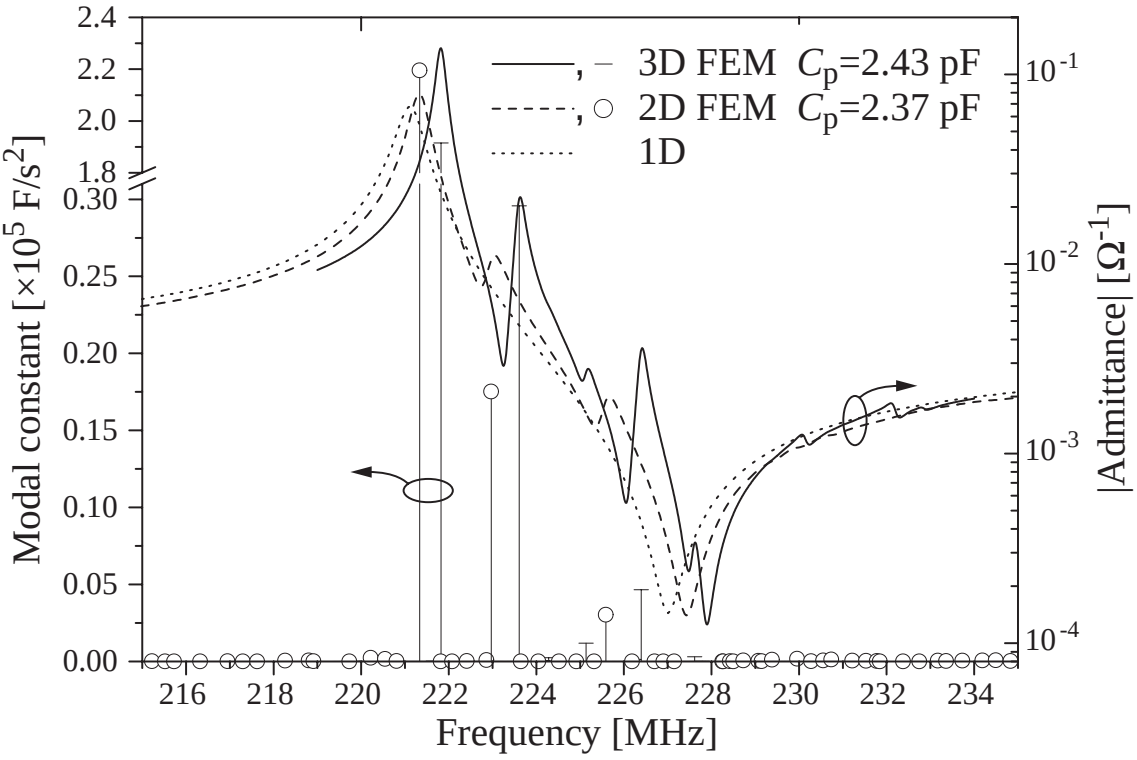

Figure 2.5: Magnitude of admittance (right axis) as a function of frequency simulated with a 1D model (dotted line) and with 2D (dashed line) and 3D FE models (solid line). In addition, the computed modal constants are shown (left axis). C_p is the computed static capacitance.

conditions employed in the 2D FE model are shown in Fig. 2.3. The free space region above the resonator is not included into the FEM model. Hence, we assume that the electric displacement is confined to the ZnO, a fair approximation for materials with high permittivity [127]. Thus, the electric boundary condition on the nonmetallized part of the ZnO top surface is that the normal component of the electric displacement vanishes.

In Fig. 2.6 the mode shapes for the fundamental TE1 and the third anharmonic TE1 mode computed using 2D FEM are shown. The model has been mirrored with respect to the symmetry plane to restore the complete resonator. The mode shapes show strong variation of electric potential at the electrode edges. They also show the exponential decay of the displacements in the region outside the top electrode. The experimental determination of the dispersion curves discussed in Paper II is based on measuring the displacements of these standing waves within the top electrode region. It is found that several different Lamb-wave modes exist at each frequency within the top electrode region. The computed charge distribution on the top electrode associated with the standing wave (lateral mode) may be integrated to obtain the contribution of the lateral mode to the electrical response (so called modal con-

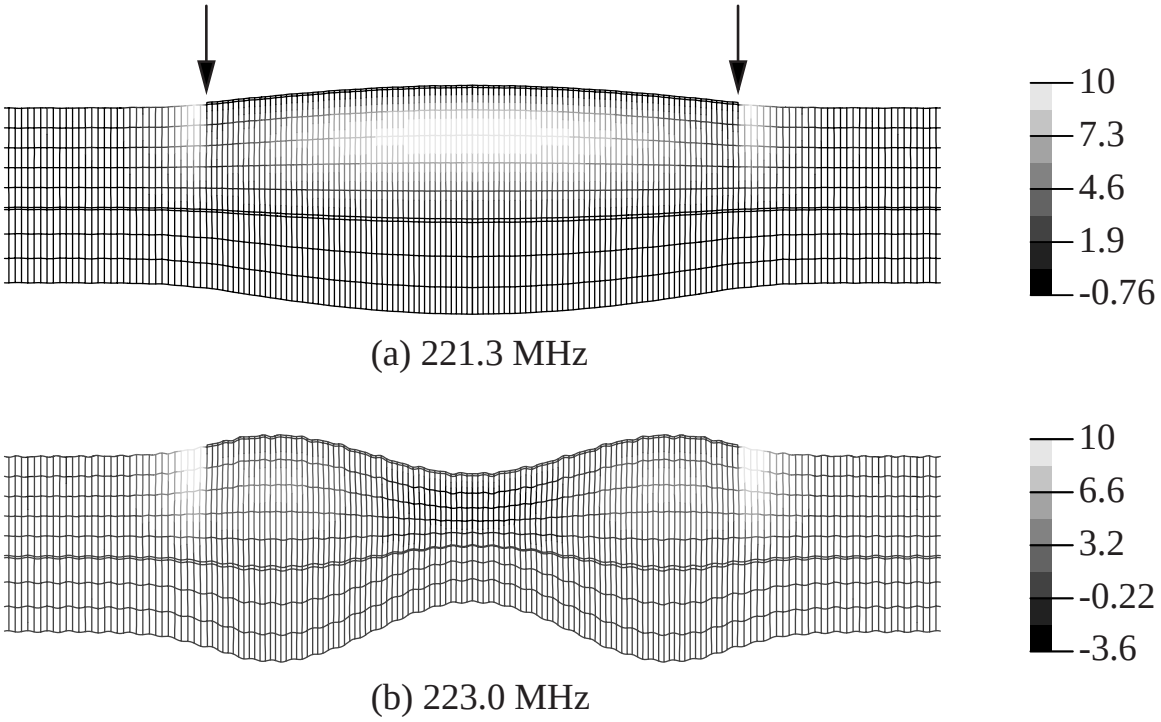

Figure 2.6: Mode shapes for fundamental and third anharmonic TE1 modes computed with 2D FE model. The bottom electrode is grounded and the top electrode is set to potential 1 V. The displacements are shown exaggerated for illustrative purposes. The gray scale coding indicates electric potential and it is normalized separately for each mode such that the maximum is given the value 10. The arrows mark the edges of the top electrode. The lateral and vertical dimensions are not on the same scale.

stant [116, 117]). If the modal constant is nonvanishing, the standing wave manifests itself as a resonance peak in the computed electrical response of the resonator. The lateral modes with a vanishing total charge on the electrode are decoupled and cannot be excited using voltage excitation, e.g., the even-order anharmonic TE1 modes in the 2D case (with even number of displacement maxima across the top electrode region).

In Paper I, the effect of the top electrode shape of an SMR on the behaviour of the spurious resonances is examined. The paper presents the novel result of usage of 3D FEM to investigate the effect of the top electrode shape of an FBAR on the electrical response, with verification of the simulations by comparing the simulated and measured displacements on the resonator top surface. Using an asymmetric top electrode has been suggested as a means to decrease the spurious mode content [128]. However, the computational results in Paper I indicate that the asymmetric electrode shape considered does not significantly affect the strength nor the frequency separation of the spurious resonances due to the anharmonic TE1 modes. Lanz [51] reported

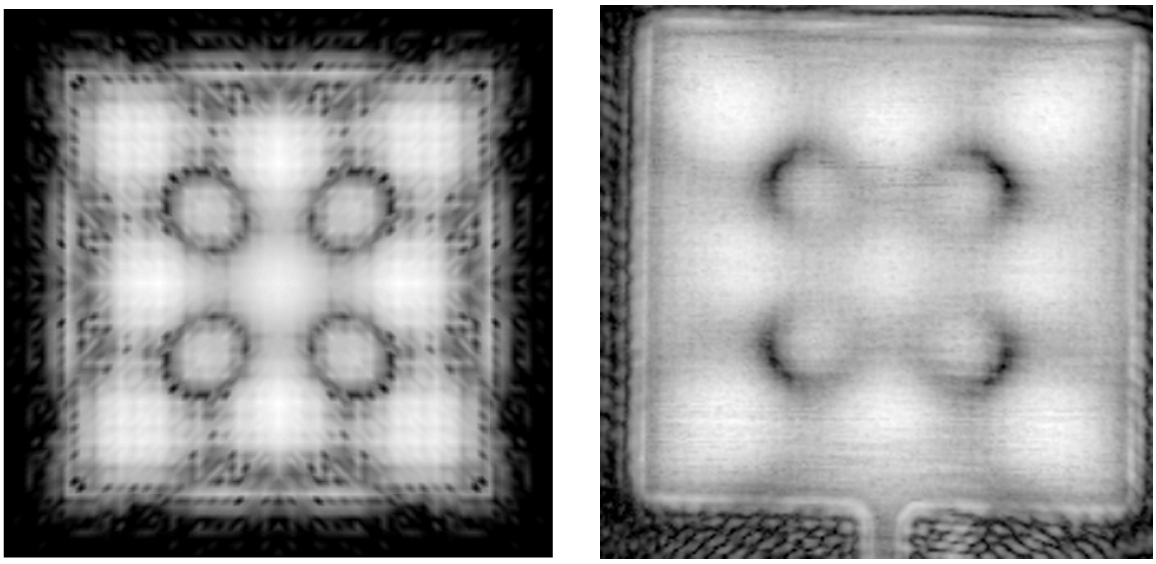

1070.5 MHz 1070.0 MHz

Figure 2.7: Magnitudes of z-displacements on the top surface of an FBAR with a square top electrode: those simulated using 3D FEM (left) and those measured using a laser-interferometer (right). The z-direction is normal to the surface.

strong spurious resonances for experimental AlN based bridge-type FBARs despite the asymmetric electrode shape. Another electrode shape reported to be effective in suppressing the spurious modes is the one with all the sides curved [129]. However, in this work the behaviour of spurious modes for this electrode shape was not diagnosed. In Paper I, the computed displacements on the top electrode are compared against the experiment at several frequencies, both for rectangular and circular top electrodes. A fair agreement between the simulated and measured displacement profiles is found. The computed and measured displacements for the resonator with a square top electrode are shown in Fig. 2.7.

Here, we further demonstrate the applicability of the developed FEM tool in FBAR design through considering a method proposed for the suppression of the spurious modes in [71, 130]. To explain the method in greater detail, let us first consider the dependence of the resonance frequency on the electrode width. Figure 2.8 displays the resonance frequency of the fundamental TE1 mode as a function of the top electrode width. The computation is carried out with FEM modal analysis using a 2D model of the resonator in Fig. 2.3 with a 600 nm thick top electrode. It is seen that the resonance frequency increases with decreasing top electrode width.

In the method for the suppression of the spurious resonances, the resonator geometry is chosen such that there is a narrow region at the edge of the top electrode where the thickness of the stack is larger than elsewhere on the top electrode. This

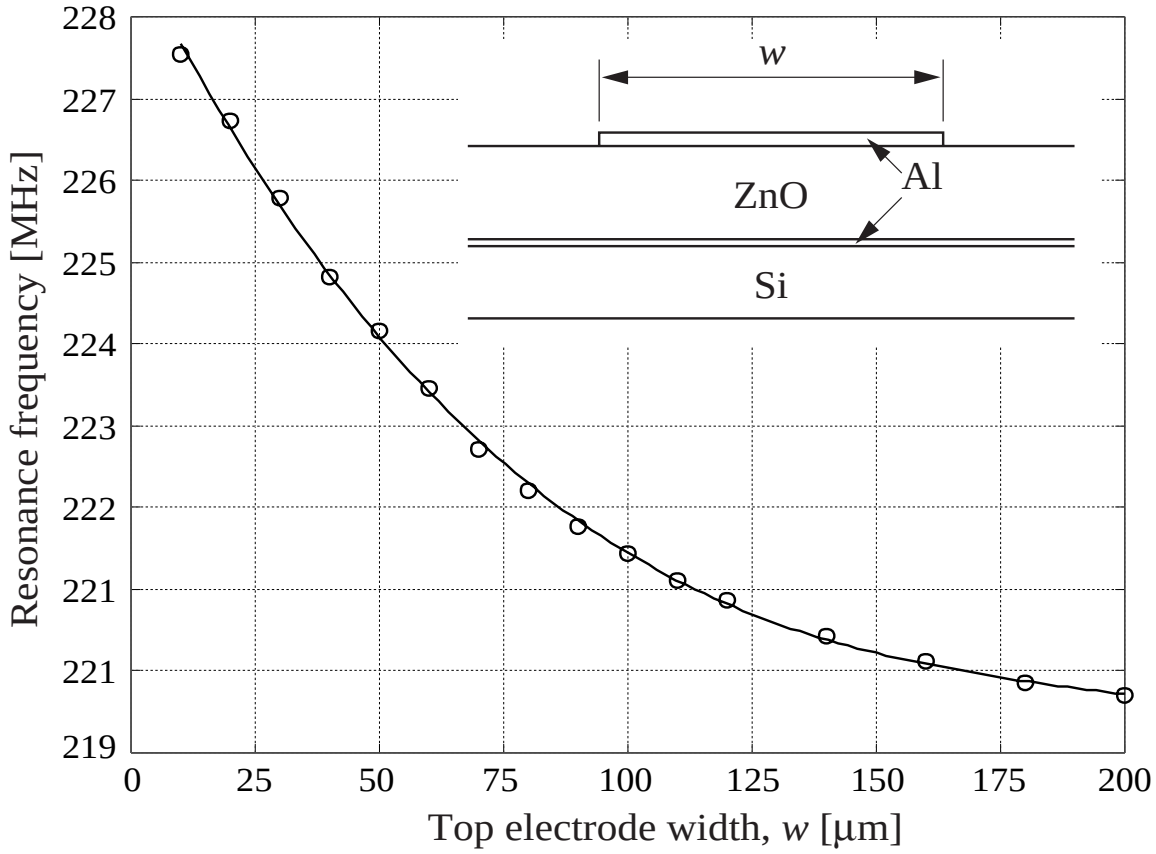

Figure 2.8: Resonance frequency of the fundamental TE1 mode as a function of top electrode width (w), obtained using 2D FEM modal analysis (circles). The solid line is a fitted cubic polynomial. The layer thicknesses are same as those for the resonator in Fig. 2.3, except that the top electrode is 600 nm thick.

thickened region forms a frame around the top electrode. If this edge region were infinite in lateral extent, its resonance frequency would be lower than that for the main area of the top electrode because it is thicker than the main area. However, due to the fact that the resonance frequency increases with decreasing electrode width, the resonance frequencies of the narrow edge region and the main top electrode region approach each other. Within certain optimum range for the edge region width, the conditions at the edge region of the main electrode area become such that the resonator operates in a mode, where the displacement magnitudes are approximately equal everywhere on the top electrode, as shown in Fig. 2.9 (a). The mode shape for the fundamental TE1 mode may be compared with that shown in Fig. 2.6 (a), where the displacement amplitude is highest at the middle of the electrode and decreases towards the electrode edges. Furthermore, the charge distributions on the electrodes associated with the anharmonic TE1 modes also change such that they become only weakly coupled to the driving electric field. The electrode shape considered provides

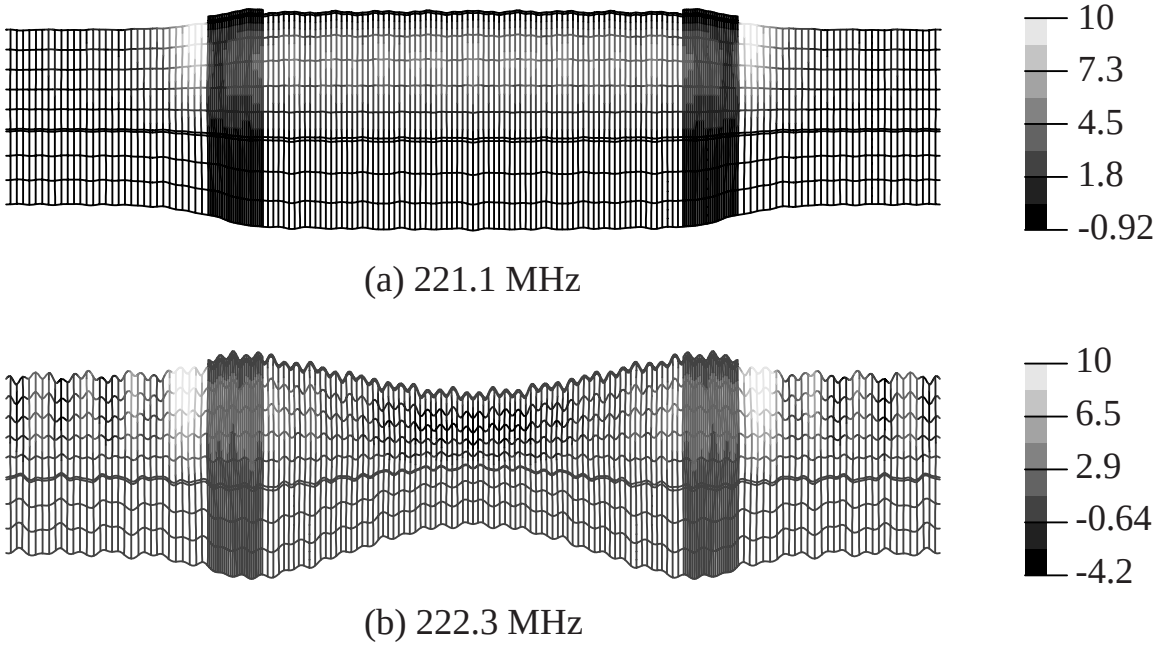

Figure 2.9: Mode shapes for fundamental and third anharmonic TE1 modes computed for 2D FE model that has a 52 μm wide and 600 nm thick region at the top electrode edges (see the left inset in Fig. 2.10 for schematic of the geometry). The bottom electrode is grounded and the top electrode is set to potential 1 V. The displacements are shown exaggerated for illustrative purposes. The gray scale coding indicates electric potential and it is normalized separately for each mode such that the maximum is given the value 10. The lateral and vertical dimensions are not on the same scale.

a flat displacement amplitude profile and effectively suppresses anharmonic modes, which was also recognized by Hirama *et al.* [131] in their theoretical study of quartz resonators with such an electrode shape. The mode shape for the third anharmonic TE1 mode is plotted in Fig. 2.9 (b), which may be compared with the corresponding mode shape in Fig. 2.6 (b).

Considering the resonator in Fig. 2.3, the 2D FEM simulation results in a frequency response, clean of the spurious resonance peaks due to the anharmonic TE1 modes, when the top electrode is made 600 nm thick within a 52 μm wide region at the edge of the top electrode. The simulated admittances for the model with and without the thickened edge region are plotted in Fig. 2.10. It shows that the spurious resonances caused by the anharmonic TE1 modes are strongly suppressed. Indeed, selecting the width and thickness of the edge region appropriately, a clean frequency response for the FBAR may be obtained.

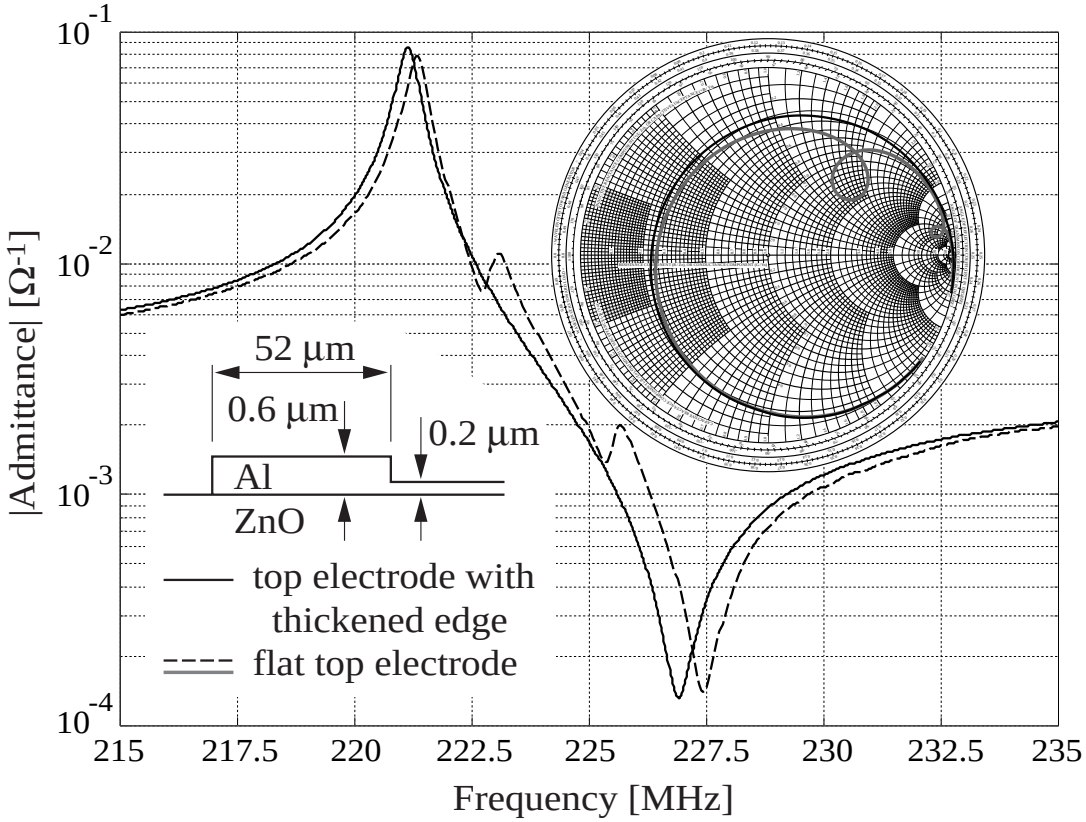

Figure 2.10: Magnitude of admittance versus frequency for resonators with and without a thickened region at the top electrode edges computed using FEM modal analysis. The left inset shows the dimensions of the top electrode edge region. The right inset displays the S_{11} parameter for the two resonators on the Smith chart.

2.5 Computation of dispersion curves for acoustic waves in layered structures

In the research presented in Paper II, the global matrix method [132] is used in the numerical computation of the dispersion curves, accounting for anisotropic and piezoelectric layers [133]. The implementation can properly handle the exponentially increasing/decaying fields of evanescent partial modes inside the layers. This exponential behaviour may lead to numerical instabilities for the other commonly used computational method, viz. the transfer matrix method [134, 135]. However, global matrix method requires larger computational effort than the transfer matrix method, since the size of the linear system of equations describing the stratified structure is proportional to the number of layers in the structure. Recently, a new scattering-matrix method which is computationally economical and does not suffer from numerical instabilities has been reported by Pastureaud *et al.* [136].

In the matrix formulation used in the computational method utilized in Paper II, straight-crested waves are considered, i.e., the field quantities are taken to be independent of one of the coordinates, say, y-coordinate. The fields are taken to assume the form $e^{-ik_x x - ik_z z} e^{i\omega t}$, where ω is the angular frequency and k_x and k_z are the x and z-components of the wavevector, respectively. Substituting this ansatz into the constitutive and governing equations for the piezoelectric material under the quasi-static approximation, an eigenvalue problem with a coefficient matrix of size 8×8 is obtained, which is solved at given x-component of the wavevector. The eigenvectors represent the bulk-wave modes in an infinite medium and the eigenvalues describe the dependence on z of the modes (z direction being the thickness direction). The elements of the generalized eigenvectors are the generalized displacements and the generalized stresses. The generalized displacements comprise the three displacement components and the electric potential. The generalized stresses embody the three stress components (T_{zi}, i=x,y,z) and the z-component of electric displacement (D_z).

Within each layer, the fields are represented as linear combinations of the eigenvectors. Proper care has to be taken in the numerical treatment of the problem to avoid numerical difficulties which may occur for large frequency-slowness-thickness products owing to the exponential behaviour of the field variables for evanescent modes [136]. This is accomplished by associating the modes decaying into the $+z$ and $-z$ directions with different reference planes in the z-direction. For modes decaying towards $-z$, the origin is placed at the top interface of the layer (interface with a higher z-coordinate value) and for modes decaying towards $+z$, it is placed at the bottom interface of the layer. Then, the displacements and potential, as well as the stresses and D_z at the bottom and top interfaces of a layer may be expressed as linear combinations of the eight modes. Hence, we have eight unknown coefficients and 16 equations. Solving the eight coefficients from the equations for displacements and potential and substituting into equations for stresses and electric displacement, we obtain Green's function which relates the generalized stress to the generalized

displacement at the top and bottom interfaces of the layer. For layers of dielectric and piezoelectric materials the size of the matrix is 8×8. For metals the matrix is 6×6, as only mechanical field variables are considered. For a dielectric or piezoelectric half-space, four of the eight modes are selected: modes decaying into the substrate (surface waves) and those corresponding to bulk waves with the energy flow into the substrate. The resulting matrix is then 4×4 instead of 8×8. Vacuum supports only electric fields. Hence, only the relation between potential and D_z is considered, and the resulting matrix is a scalar. In vacuum, the potential must decay towards infinity.

To obtain the equations describing the complete layer stack (system equations), interface and boundary conditions involving the mechanical and electrical field variables at the material interfaces and the stack bounding surfaces, respectively, are imposed. In the numerical equations, the mechanical displacements and the electric potential on each interface are the unknowns (comprising column array u below). For each layer, the associated Green's function is computed. The electric potential and the three components of stress are required to be continuous across the material interfaces (stress components vanish at vacuum interfaces). Across the interfaces between dielectric materials, the three displacement components and D_z are taken continuous (at vacuum interfaces, there are no conditions imposed on the displacements). Across interfaces where the material on one side of the interface is a metal, the condition of continuous D_z is dropped. Instead, for each metal layer we need to impose either a condition for its potential or a condition for the total charge density (current) on the metal. The total charge density for a metal layer is obtained as $D_{z1} - D_{z2}$, where D_{z1} and D_{z2} are the z-components of the electric displacement at the upper and lower interfaces of the metal, respectively, when the interface is approached from the dielectric side.

As an example, consider an interface separating two dielectric materials. All the field variables need to be continuous across this interface. Hence, this interface will result in 8 rows to the system equations:

$$u_{\mathrm{i,b}}^{(\mathrm{u})} - u_{\mathrm{i,t}}^{(\mathrm{l})} = 0 \tag{2.2}$$

$$T_{\mathrm{i,b}}^{(\mathrm{u})} - T_{\mathrm{i,t}}^{(\mathrm{l})} = 0 \ , \tag{2.3}$$

i=1,2,3,4, where u_1, u_2, u_3 and u_4 represent x, y, z-displacement and potential, respectively, and T_1, T_2, T_3 and T_4 represent T_{zx}, T_{zy}, T_{zz} and D_z, respectively. (u) and (l) denote the upper and lower layers with respect to the considered interface, respectively. Furthermore, b and t denote bottom and top interface of the layer, respectively.

Following the above steps, we obtain a linear system of equations $\mathrm{G}u = b$. As displacements and potential at the interfaces are the unknowns, each row of matrix G corresponding to Eq. (2.2) has only two nonvanishing elements, whose values are 1 and -1. The rows of the G matrix corresponding to Eq. (2.3) are obtained from the 8×8 matrices (discussed above) for the two dielectric layers. The column array b

is mostly zero (because of the requirement of continuity of the field variables across the materials interfaces). However, to solve u from the equations, at least one of the elements of b must be nonzero to serve as an excitation force for generating the waves, e.g., the stress component T_{zz} at the top surface of the stack.

One of the field variables is selected as the response of interest. This may be, e.g., current in one of the metal layers, or stress, potential or displacement at one of the materials interfaces. After solving for u from the system equations, the response can be obtained either directly from u (in the case of displacements and potential) or computed using u (in the case of currents and stresses). To determine the mode frequencies for a given k_x, the system matrices are formed and solved at specified frequencies to compute the desired response as a function of frequency. The magnitude of the response versus frequency curve shows peaks corresponding to propagating Lamb-wave modes. The frequencies of the modes at a given k_x are determined as the frequencies for which the maxima occur. The excitation conditions (elements of array b) and the response of interest may be selected to accentuate certain modes over the others. For example, using the shear stress component for the excitation and the displacement component parallel to the layers as the response favours thickness shear (TS) modes over the thickness extensional (TE) modes. Alternatively, one may compute the magnitude of the determinant of the system matrix versus frequency and determine the mode frequencies as the frequencies of the minima. For lossless modes both approaches yield the same frequencies. Assuming that loss mechanisms such as viscous losses are not present, modes in plates with finite thickness are lossless. However, if the structure comprises a semi-infinite substrate, the propagating wave may lose energy through radiation of bulk waves into the substrate. With increasing loss and assuming real-valued k_x, the response peak broadens and its height decreases rendering the determination of the accurate mode frequency more difficult.

2.6 Determination of material parameters in FBARs

The main purpose of the research reported in Paper II was to investigate a technique based on fitting the calculated and experimentally obtained dispersion curves for an FBAR device for the determination of materials constants for thin-films. The paper presents a novel approach of using dispersion curves measured with scanning laser interferometer from SMR in the fitting procedure to obtain best fit values for the density and stiffness matrix elements of thin-film ZnO.

Techniques for the evaluation of elastic constants of films employing fitting of the measured and calculated velocity dispersion of SAW [29, 137, 138] or Lamb-wave modes [139] are quite common. However, these techniques involve specialized test devices employing IDTs for wave generation and the velocity dispersion is usually obtained from electrical measurements. Also the Brillouin scattering technique has been pursued to experimentally determine the dispersion curves for Rayleigh SAW modes, with subsequent fitting procedure to determine the elastic constants for ZnO

thin films [88]. In Paper II, the dispersion curves of Lamb-wave modes are obtained experimentally with the help of laser-interferometric measurements. The interferometer is used to measure the displacement amplitude profile on the top electrode of an SMR. The spatial data is Fourier transformed into the wavenumber space to obtain the lateral components of the wavevector for the excited wave modes. The interferometer used in the measurements detects only the relative vibration amplitude on the surface in direction normal to the surface. Because of the absence of phase data, the measurement relies on the presence of standing waves arising from the reflection of the Lamb waves at the edges of the top electrode as discussed in Section 2.4.

In the homodyne laser interferometer used in the measurements [37], the measured relative vibration amplitude depends on the reflectivity of the sample surface. Assuming that the true vibration amplitude remains constant, the measured value of the relative vibration amplitude decreases with decreasing light reflectivity of the surface. For example, metal usually has higher reflectivity than dielectric or piezoelectric material and, thus, metallized regions yield a correspondingly higher measured amplitude. Hence, to improve the sensitivity, a correction procedure compensating for the variations caused by the varying light reflectivity of the top electrode surface is employed. Furthermore, to enhance weak modes, circular integration of the Fourier transformed data is performed [140, 141]. This may be done, because the c-axis of ZnO is oriented in the direction of the surface normal and, consequently, it is isotropic in the plane of the resonator, i.e., the velocity does not depend on the propagation direction in the plane of the structure. The dispersion curves are obtained through carrying out the measurement and processing the data for each frequency.

In the calculations reported in Paper II, the published values were used for the materials parameters of other layers except the ZnO. The computation also showed that the elements of the piezoelectric matrix and dielectric matrix only weakly affect the dispersion behaviour and, consequently, they were also fixed to the published values [119]. Hence, in the fitting procedure, only the values of the density and the stiffness matrix elements for the ZnO were allowed to vary. Their values were modified in the numerical calculations until the calculated and measured dispersion curves agreed well. The measured dispersion curves and those computed using the best fit values for the optimized material constants are plotted in Fig. 2.11. In the optimization of the materials constants, the conjugate gradient method with a Polak-Ribiere update rule [142] was used. For the determination of the elements of the piezoelectric matrix for thin-film ZnO, other methods need to be used. For instance, to estimate the value of the element d_{33} of the piezoelectric strain matrix, a double-beam interferometer [143] has been employed [50].

The resonator studied in Paper II is of the SMR type which contains seven different thin-film layers deposited on the substrate, four of them constituting the acoustic mirror. Since the dispersion behaviour also depends on the materials constants of the mirror layers, more accurate results may be obtained for a membrane-type FBAR,

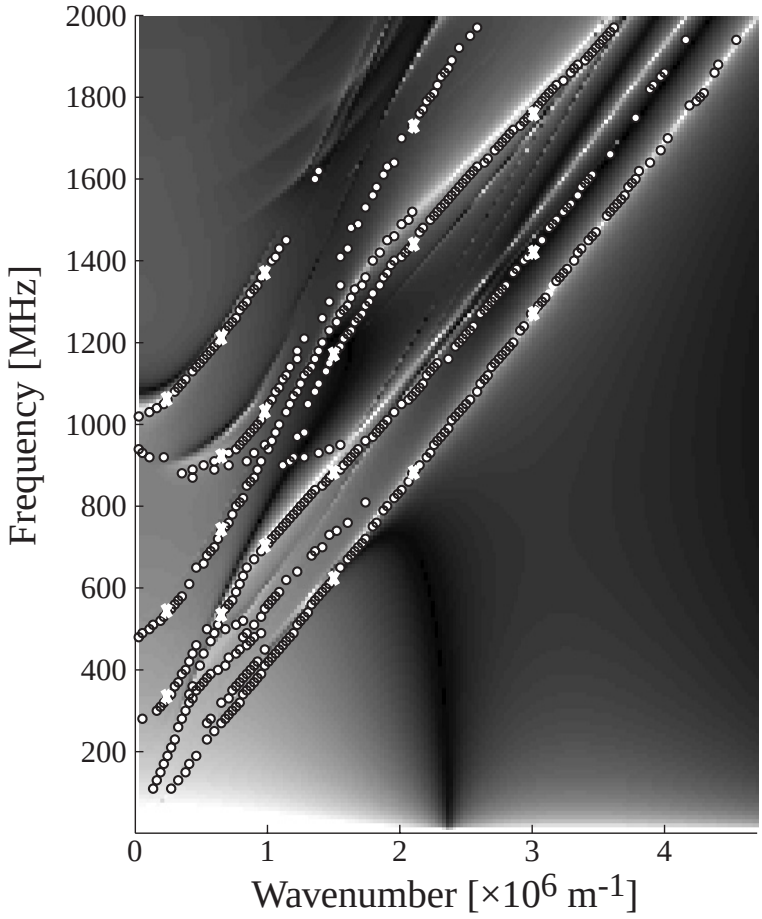

Figure 2.11: Measured dispersion curves (circles) and those computed using the optimized values for density and stiffness matrix elements of ZnO (grayscale). The crosses indicate the points on the measured dispersion curves which were used in the fitting procedure.

which is composed of the piezoelectric material between the top and bottom electrodes and possibly a support layer below the bottom electrode. The approach described here has the potential of determining materials constant for several materials in the layered stack simultaneously. The fit between the measured and simulated dispersion curves could be further improved through including the materials parameters of the electrodes into the fitting procedure. However, this was not done in this work as the increase in the number of fitted parameters also increases the computation time. The benefit of the method is that its application requires no special test structures [139] although such structures would help to improve the reliability and accuracy of the method.

3 Longitudinal leaky surface acoustic waves (LLSAW) and LLSAW devices

This Chapter is a summary of Papers III–V, where a high-velocity wave mode, the longitudinal leaky surface acoustic wave (LLSAW), propagating under a periodic Al grating deposited on YZ-cut $LiNbO_3$ substrate is considered. The velocity of the LLSAW is between those of the shear and longitudinal bulk waves. Because of the high velocity, the LLSAW has the potential to be used in realization of filters up to the 5 GHz WLAN band. Before discussing the LLSAW on YZ-cut $LiNbO_3$ in detail, several configurations and substrates where the LLSAW mode has been found are reviewed.

3.1 LLSAW mode in monocrystalline and layered configurations

The LLSAW mode with a high phase velocity exists in several monocrystalline substrate materials. Sato and Abe have applied LLSAW on lithium tetraborate ($Li_2B_4O_7$) substrate to realize bandpass filter of interdigital interdigitated type with center frequency close to 1.5 GHz [144]. The LLSAW on $Li_2B_4O_7$ features low attenuation, both on a flat surface (either free or metallized) [32] and under a periodic Al grating [145]. Tonami *et al.* [146] studied theoretically LLSAW on (90°, 90°, ϕ)-cut $LiNbO_3$ and $LiTaO_3$ substrates. The dependence of the propagation characteristics on the crystallographic angle ϕ was reported both for electrically open and shorted surfaces. Kobayashi *et al.* [30] confirmed experimentally the existence of LLSAW on (90°, 90°, 37°)-cut $LiNbO_3$ and on (90°, 90°, 31°)-cut $LiTaO_3$. They fabricated a bandpass filter on the (90°, 90°, 31°)-cut $LiTaO_3$ substrate based on LLSAW with a center frequency of 1.9 GHz and a minimum insertion loss (IL) of 3.3 dB [147]. Isobe *et al.* [33] have theoretically and experimentally investigated the propagation properties of LLSAW on several cuts of $LiNbO_3$ and $LiTaO_3$ substrates. The numerical results were obtained through modeling an infinite interdigital transducer (IDT) using a simulation tool for periodic structures. The tool employed FEM to model the electrodes and the region immediately underneath the electrodes, below which the fields were modeled using space harmonics expansion. They found several cuts with low propagation losses. For the cuts explored the phase velocity of LLSAW in an Al strip grating was computed to be between the values from 6160 m/s to 6184 m/s and from 5228 m/s to 5702 m/s on $LiNbO_3$ and $LiTaO_3$, respectively. The temperature stability of frequency for selected crystal cuts was experimentally determined from test resonators. They report measured TCFs of 99 ppm/K and 78 ppm/K, respectively, at resonance and antiresonance frequencies for an Al grating with a normalized thickness of 8.4%, fabricated on (60°, 99°, 90°)-cut $LiNbO_3$. Corresponding values for an Al grating with a normalized thickness of 9.2% on (60°, 136°, 90°)-cut $LiTaO_3$ are 64 ppm/K

and 79 ppm/K. Recently, Naumenko *et al.* [148] have considered LLSAW on the (0°, μ, 90°)-cut $LiNbO_3$ substrate and optimized the cut angle μ (μ=80° is found to be the optimum), together with the Al electrode thickness and metallisation ratio from the point-of-view of resulting ladder filter performance.

LLSAW has been reported also in structures comprising a thin-film layer of piezoelectric material deposited on a substrate that supports a high acoustic-wave velocity [25, 26]. The piezoelectric thin film on the substrate enables electrical excitation of the wave. Didenko *et al.* [25] investigated the wave modes propagating in a structure consisting of a ZnO film on the SiC substrate. In particular, the structure supports the LLSAW mode, also called the high-velocity pseudo SAW (HVPSAW). They considered circumstances where the sagittal plane is a symmetry plane of the substrate and film, and the interface is the plane of elastic symmetry for both the substrate and the film[6]. The LLSAW mode consists of two partial wave components: The predominantly longitudinally polarized partial wave, which decays exponentially into the substrate, and the predominantly horizontally polarized partial wave, radiating energy into the bulk. However, it was found that for a certain thickness of the ZnO layer, the LLSAW mode degenerates into a proper SAW. Then, the amplitude of the shear partial wave vanishes and, in substrate, the LLSAW solution is composed only of the quasi-longitudinal partial wave component.

The novel waveform described by Didenko *et al.* was theoretically studied by Darinskii *et al.* [149]. Sufficiently strong anisotropy of the substrate was found to be a necessary condition for the existence of the nonattenuated SAW. The authors provided an explanation for the vanishing of the shear partial wave component. The longitudinal and shear partial waves are coupled in the substrate through the substrate boundary and the materials constants (stiffness matrix component C_{13} in the case of an isotropic material). In addition, the partial waves are coupled through the presence of the layer on the substrate surface. For certain value of thickness, these two mechanisms of coupling work in opposite directions and cancel each other, resulting in the decoupling of the shear and longitudinal partial waves. Then, in the substrate the wave is composed only of the longitudinal partial wave which decays exponentially into the substrate. In this case, the LLSAW mode becomes a proper SAW propagating without attenuation [25, 26].

The propagation properties of the SAW, such as the phase velocity, electromechanical coupling coefficient, propagation loss, power flow angle and temperature behaviour are sensitive to the material properties and thickness of the thin film. As discussed in Chapter 2 in connection with FBARs, accurate control of the film parameters may prove difficult. Additional challenges associated with the stratified configurations that have been stated [25] are the dispersion of the SAW velocity and the fact that the propagation loss of the wave may be dominated by the polycrystalline film. Moreover, the need to deposit the thin-film layer complicates fabrication and

[6]These symmetry conditions hold also for LLSAW on YZ-$LiNbO_3$, studied in Papers III–V.

increases costs. Employing wave modes in monocrystalline substrates, the difficulties pointed out above may be avoided to a large degree.

3.2 LLSAW on YZ-cut $LiNbO_3$

The substrate material investigated in the research reported in Papers III–V is the YZ cut of $LiNbO_3$. LLSAW properties on YZ-$LiNbO_3$ were first studied by Grigorievski [34]. Although Isobe *et al.* [33] have found cuts of $LiNbO_3$ which exhibit higher Q values than the YZ cut, this cut [specified by Euler angles $(0°,-90°,-90°)$] possesses many desirable properties because it is readily available, there is no beam steering, and the cut is only weakly pyroelectric.

In contrast to, e.g., $Li_2B_4O_7$, where the propagation loss of LLSAW is low both on an open and a shorted flat surface (calculated values for $(0°, 47.3°, 90°)$-cut $Li_2B_4O_7$ are 5×10^{-4} dB/λ and 8.4×10^{-3} dB/λ for free and metallized surfaces, respectively [32]), for YZ-$LiNbO_3$ the propagation loss on a shorted flat surface is high, 1.5 dB/λ [31, 34]. In addition to the SAW propagation properties on a uniform electrically open or shorted surface, it is also necessary to consider propagation on a periodically disturbed surface, as SAW devices employ periodic electrode structures, e.g., IDTs and grating reflectors. Grigorievski found that the propagation loss of LLSAW decreases significantly for a periodic system of electrodes [34]; for a shorted Al electrode grating on YZ-$LiNbO_3$ with the normalized thickness of 8% and metallisation ratio[7] 0.5, the loss is on the order of 0.03 dB/λ [150]. The phase velocity of LLSAW for this configuration is approximately 6100 m/s [150, 151], which is about twice the velocity of the Rayleigh SAW on the same cut.

The displacements for LLSAW on YZ-$LiNbO_3$ are confined to the sagittal plane. The solution contains only one shear partial wave term, which gives rise to the shear bulk wave radiating energy into the solid and being responsible for the propagation loss. The shear bulk wave with displacements perpendicular to the sagittal plane is decoupled. Apparently, the grating modifies the boundary condition at the substrate surface such that the coupling to the shear wave radiating into the bulk weakens and, consequently, the propagation loss decreases. The displacements in an LLSAW mode propagating on YZ-$LiNbO_3$ under an Al grating are visualized in Fig. 3.1. The substrate surface is in the direction of crystal Y axis and the propagation direction is parallel to the crystal Z axis. The components of mechanical displacement and electric potential as a functions of distance from the substrate surface are plotted in Fig. 3.2, showing the exponential decay of the dominant longitudinal displacement component (u_z) into the substrate. The energy of the wave is localized close to the surface. This property together with the fact that the crystal Z-direction (propagation direction of the LLSAW) is the direction with the strongest piezoelectricity results in a high effective coupling coefficient for the wave. Because of the intrinsically leaky nature

[7] a/p parameter, where $a(< p)$ is the electrode width and p is the center-to-center distance of adjacent electrodes (see Fig. 3.3).

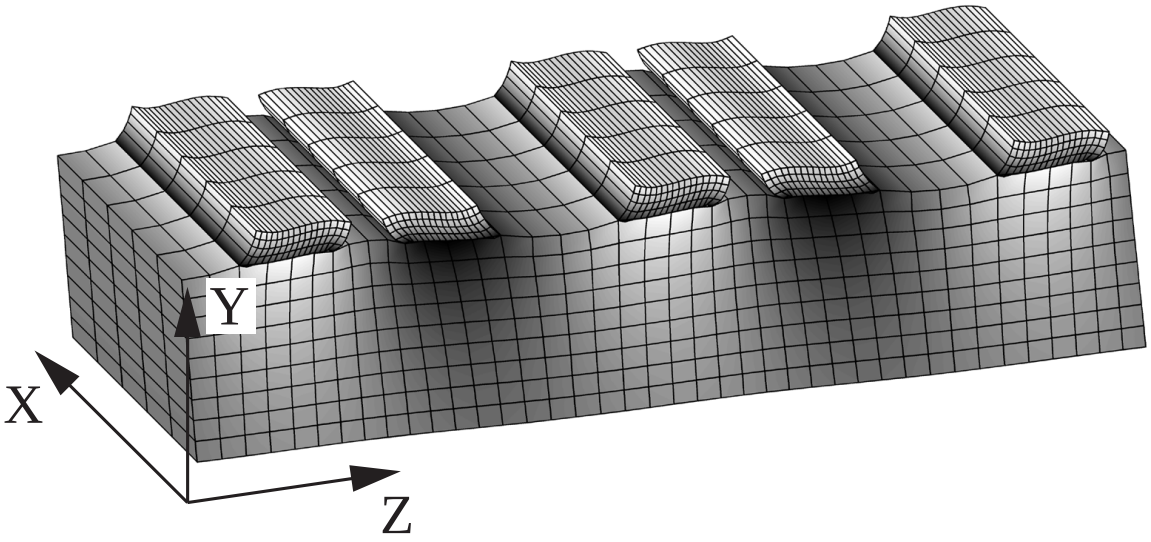

Figure 3.1: Characteristic displacements for the LLSAW mode propagating on YZ-cut lithium niobate under a periodic system of aluminum electrodes with a normalized thickness h/λ_0 of 7.8%. The displacements, simulated using periodic FEM/BEM software, are exaggerated for the illustration purposes. The shades of gray for the substrate indicates the displacement component in the propagation (crystal Z) direction. The shades of gray for the electrodes are independent of those for the substrate and they indicate the magnitude of the Z-displacement.

of the LLSAW, the modeling primarily aims at identifying the grating parameters minimizing the losses.

3.3 Numerical simulation of LLSAW propagation properties

SAW devices often comprise long periodic gratings of metal electrodes. Therefore, it is important to know the propagation properties of the wave in such a grating. In Paper III, the propagation properties of LLSAW in a grating of Al electrodes on YZ-$LiNbO_3$ substrate are studied using numerical simulations.

3.3.1 Periodic FEM/BEM simulator

Several modeling approaches are available for the prediction of the electrical response of a SAW resonator. A phenomenological coupling-of-modes (COM) model [152–154] is widely used in design of SAW devices; its accuracy is excellent for the Rayleigh SAW. The COM model involves two interacting, counterpropagating waves [155]. The parameters used in the COM model need to be specified separately for each substrate and electrode geometry. The COM model assumes perfect waveguiding and it is not capable of modeling the scattering of the surface wave mode into the bulk

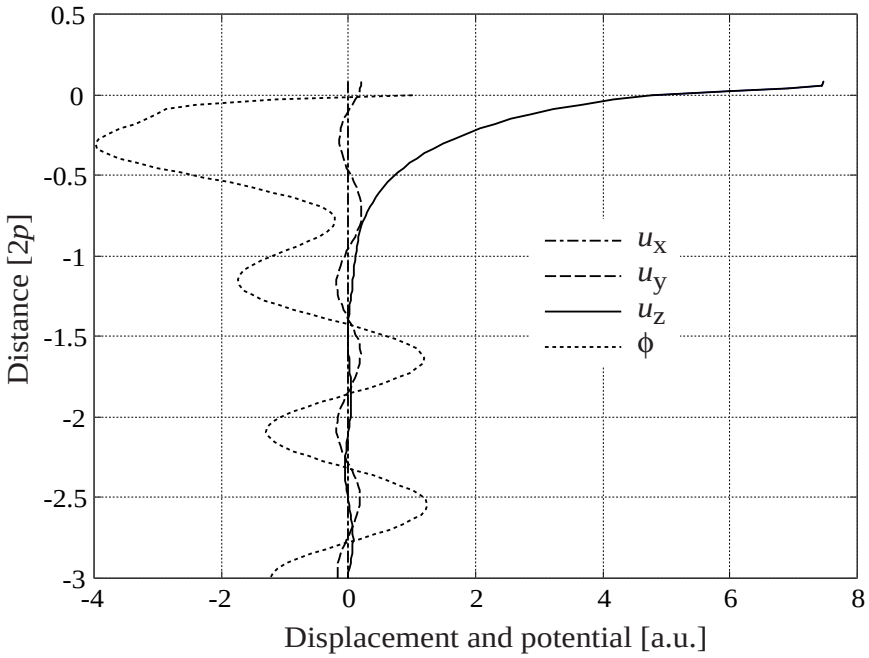

Figure 3.2: Components of displacement and electric potential versus distance from the substrate surface for an LLSAW mode under an Al electrode grating on YZ-$LiNbO_3$ computed using periodic FEM/BEM software. Normalized thickness of Al electrodes is $h/\lambda_0 = 7.8\%$. Distance is in units of electrical period of the IDT. The displacements above the substrate surface (for positive distance values) are the displacements in the electrode.

wave mode. Moreover, it does not take into account changes in the structure of the wave as a function of frequency. For example, the localisation depth of the wave may change quite rapidly close to the bulk-wave threshold frequency. Therefore, accuracy of the COM model for leaky SAW and LLSAW is limited. Several improvements have been proposed to the COM model [155, 156] when applied to the modeling of leaky SAW structures accounting for, e.g., the fast shear bulk wave radiation. Higher accuracy may be achieved with more complex numerical models such as the finite-element-method/boundary-element-method (FEM/BEM) technique [157] discussed below. However, the increasing accuracy obtained with more complicated models also increases the computational cost which may render the method effectively unusable in the practical design work. Nevertheless, the computationally expensive models may be used to determine numerically the parameters needed in the simpler models [101].

To characterize properties of waves propagating on a substrate with a periodically loaded surface, the so-called FEM/BEM technique has been developed [99, 158]. The FEM/BEM approach uses a Green's function formulation [159–161] to model the substrate and FEM to model the electrodes. Although the 2D FEM/BEM is among the most accurate models used in SAW design today, it still neglects several effects that

have significant influence on the resonator response. For example, the capacitance between the busbars of the SAW resonator as well as the capacitance between the end of the finger electrode and the adjacent busbar are ignored. These increase the static capacitance of the resonator, which induces a decrease of the antiresonance frequency and, consequently, a decrease of the effective coupling coefficient. Estimates for these parasitic capacitances may be obtained experimentally from measurements of various test structures in order to predict more accurately the resonator response. It should be noted here that for the thin-film bulk acoustic resonators (FBARs), parasitic capacitances are lower than for SAW resonators as the electric field is confined to the volume between the two electrodes. The contribution of the fringing field to the total static capacitance of the FBAR decreases with increasing area of the resonator, as the ratio of the length of the electrode perimeter to electrode area decreases [162].

In the periodic FEM/BEM modeling approach employed here [157], the components of stress and electric charge density on the substrate surface are represented within one period as a sum of Legendre and Chebychev polynomials, respectively. The unknowns in the problem are the coefficients of the polynomials. Substituting the sum representation for stress into the FEM equations, the displacements at the electrode–substrate interfaces may be expressed in terms of the unknown stress coefficients. Similarly, dyadic Green's function for the substrate [161, 163] allows one to express the displacements on the surface in terms of the unknown stress and charge coefficients[8]. The displacements obtained from the FEM equations and those resulting from the Green's function formulation are required to be equal at selected FEM nodes on the electrode–substrate interface leading to a linear system of equations. The remaining equations are obtained from the discretization of the electrical boundary conditions, which impose the prescribed electrode voltages. The electric potential that enters the discretization of the electrical boundary conditions is expressed in terms of the unknown stress and charge coefficients using dyadic Green's function characterizing the substrate. Once the charge coefficients are solved from the equations, the total charge on an electrode and, subsequently, admittance for the infinite IDT may be computed. The modeling approach assumes an infinite aperture and that the electric charge resides at the substrate–electrode boundary. The detailed description of the computational technique is given in [157].

3.3.2 Simulation of an infinite periodic electrode array on YZ-$LiNbO_3$

From the admittance of an infinite IDT computed using the 2D FEM/BEM, the resonance frequency, the antiresonance frequency, and the Q values at resonance and antiresonance for the LLSAW mode are determined. Using the simulation tool, the

[8]Green's function used here relates the displacements and potential to the components of stress and electric charge density, whereas Green's function discussed in Section 2.5 involves the z-component of electric displacement instead of electric charge density. However, simple relations between the two Green's functions may be derived [157].

influences of the dimensions of the rectangular Al electrodes on these quantities are derived. The results obtained within this Thesis show a strong dependence of the Q values on the normalized aluminum thickness. The calculated optimum thickness which maximizes the Q value at resonance for the metallisation ratio of 0.6 is close to 8%. It is also found that the optimum thickness increases with the metallisation ratio. For a fixed metallisation ratio, the optimum thickness providing the highest Q at antiresonance is higher than that required for the highest Q at resonance. The difference between these two optimum thicknesses increases with the metallisation ratio.

Plessky *et al.* [164] have proposed that the Al electrodes act as a periodic system of $\lambda/4$ resonators coupled by the substrate, where λ is the shear wavelength in aluminum. This results in a modification of the boundary condition at the substrate surface such that the coupling between the longitudinal and shear partial waves decreases, analogous to the case of thin film on substrate discussed in Section 3.1. Using numerical simulations Solal *et al.* [165] found that, in addition to the 8% thick Al electrodes, the propagation loss of LLSAW on YZ-$LiNbO_3$ is low also for Al electrodes with about three and five times higher thicknesses. Earlier, Kobayashi *et al.* [30, 166] experimentally determined the phase velocity variation with electrode thickness for such a higher-order LLSAW mode both on (90°, 90°, 31°)-cut $LiTaO_3$ [30] and on (90°, 90°, 37°)-cut $LiNbO_3$ [166]. The Q values measured by Solal *et al.* for an LLSAW resonator with 24%-thick Al electrodes operating in the 2.5 GHz frequency range were close to 200, not much lower than those measured within this work for resonators with the Al electrode thickness of 8% (see Section 3.4). The low attenuation of LLSAW was associated with electrode resonances due to a flexural Lamb-wave mode propagating in the electrode. These results support the theory that the mechanical resonance behaviour of the fingers is essential in obtaining low attenuation of the LL-wave. Furthermore, Solal *et al.* showed with numeric simulations that a strong resonance behaviour is obtained also for LLSAWs in a split-finger IDT, i.e., an IDT with four electrodes per electrical period. Hence, the strong reflections, present in a normal IDT with two electrodes per electrical period, which give rise to the Bragg stopband, are not necessary for the existence of LLSAW.

To better understand the nature of the LLSAW mode, it is useful to briefly review the results of Baghai-Wadji and Maradudin [167]. They considered an elastic material belonging to the cubic crystal system with a periodic system of thick ridges on the surface. The dispersion curves for shear horizontally polarized waves propagating in the structure were numerically computed. It was found that the dispersion curve exhibits several branches in the nonradiative region of the wavenumber−frequency space, i.e., at frequencies below the dispersion curve for the shear bulk wave. These branches are formed because in a periodic grating consisting of an infinite number of closely spaced ridges, the displacement fields of a particular resonance mode for a single ridge become coupled through the substrate. Hence, each branch may be asso-

ciated with a vibration mode of the whole grating, obtained as a phased superposition of the displacement fields for a certain resonance mode of a single ridge. For a sufficiently large height-to-period ratio of the ridges, several of these grating modes occur within the nonradiative region of the wavenumber-frequency space. The LLSAW in a periodic system of Al electrodes on the YZ-$LiNbO_3$ substrate may be considered to be a similar grating mode where the resonance modes of the Al electrodes are coupled via the $LiNbO_3$ substrate. The dispersion curves of the LLSAW modes are in the radiative region, between the dispersion curves for the longitudinal and shear bulk waves.

Laude *et al.* [168] carried out a similar investigation as Baghai-Wadji and Maradudin, but extended it for periodic gratings of thick Al electrodes on different piezoelectric substrates. They studied surface-wave modes excited below the frequencies of shear bulk wave excitation as a function of electrode thickness. One of the surface-wave modes considered had a dominantly shear-horizontal polarization and the other was polarized dominantly in the sagittal plane. Also here, both surface-wave modes displayed multiple branches in the dispersion curves.

3.4 Synchronous one-port LLSAW resonators on YZ-$LiNbO_3$

In addition to the characterisation of LLSAW properties in an infinite Al grating, the investigations in Paper III seek for the optimal electrode geometry for synchronous LLSAW resonators maximizing the Q values. The layout of a synchronous one-port SAW resonator is depicted in Fig. 3.3. For the construction of ladder filters, individual resonators [169] are electrically interconnected. To achieve ladder filters featuring low insertion losses and steep skirts, the resonators employed need to have high Q values. Numerical simulations of LLSAW resonators were carried out to explore the effects of mass loading caused by the rectangular Al electrodes on the Q values and the resonance frequencies. To compute the electric admittance of the resonator, software based on the FEM/BEM formulation, capable of modeling finite structures, was employed [100]. The resonator performance was also investigated experimentally through fabricating and measuring test resonators on YZ-$LiNbO_3$. The detailed dependence of the resonance frequencies and Q values of synchronous one-port LLSAW resonators on YZ-$LiNbO_3$ on electrode thickness and metallisation ratio has not been previously available. Resonators with two different IDTs were considered. The first resonator type has the standard IDT shown in Fig. 3.3 (1:1 IDT), with electrodes connected alternately to opposite busbars. The second resonator has an IDT where each electrode connected to one busbar is followed by three electrodes connected to the opposite busbar (1:3 IDT) [170]. The resonance-antiresonance distance for a resonator with a 1:3 IDT is approximately half of that for a resonator with a 1:1 IDT and, consequently, ladder filters constructed using 1:3 IDT resonators have correspondingly narrower passband widths.

The simulated and measured results for a 1:1 IDT show that for the normalized Al

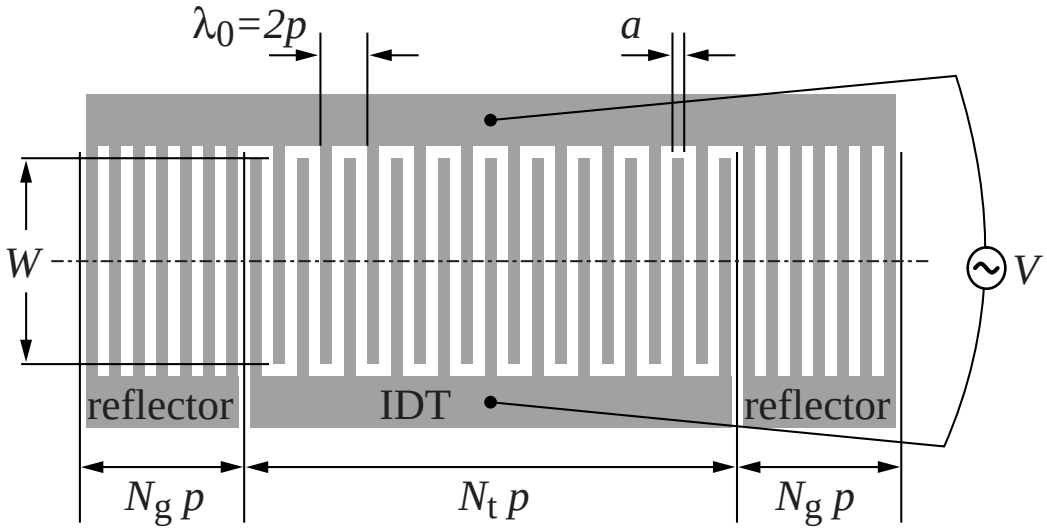

Figure 3.3: Schematic of metallisation deposited on substrate surface forming a synchronous SAW resonator. In practical resonators, the number of electrodes, N_t, in the IDT is much larger (>100) than that shown here. The two reflectors at both ends of the IDT (with N_g shorted electrodes) confine the SAW to improve the Q value. The electrical period in the IDT is $2p$. Electrode width is a and the acoustic aperture is W.

electrode thickness of approximately 8% and metallisation ratios in the range 0.45–0.50 the resonance and antiresonance frequencies are insensitive to small variations in metallisation ratio. This is beneficial because variations in metallisation ratio that may occur in the fabrication process then only have a slight effect on the operation frequency.

The variation of the measured Q values for a 1:1 IDT resonator with the Al electrode thickness is shown in Fig. 3.4. The experimental results verify that the optimum thickness for the highest Q at resonance for the metallisation ratio 0.6 is about 7.8%. The experiment also shows the increase of the optimum thickness with the metallisation ratio. However, the experiment displays that the highest Q at resonance is more than twice higher than the highest Q at antiresonance, a difference larger than theoretical predictions. The explanation for the discrepancies is still missing. Poor confinement of acoustic energy into the resonator may be one possible cause for the difference. However, experimental investigation of the displacement component normal to the substrate surface in an LLSAW resonator using a laser interferometer has not revealed any unexpected leakages of acoustic energy away from the resonator [171].

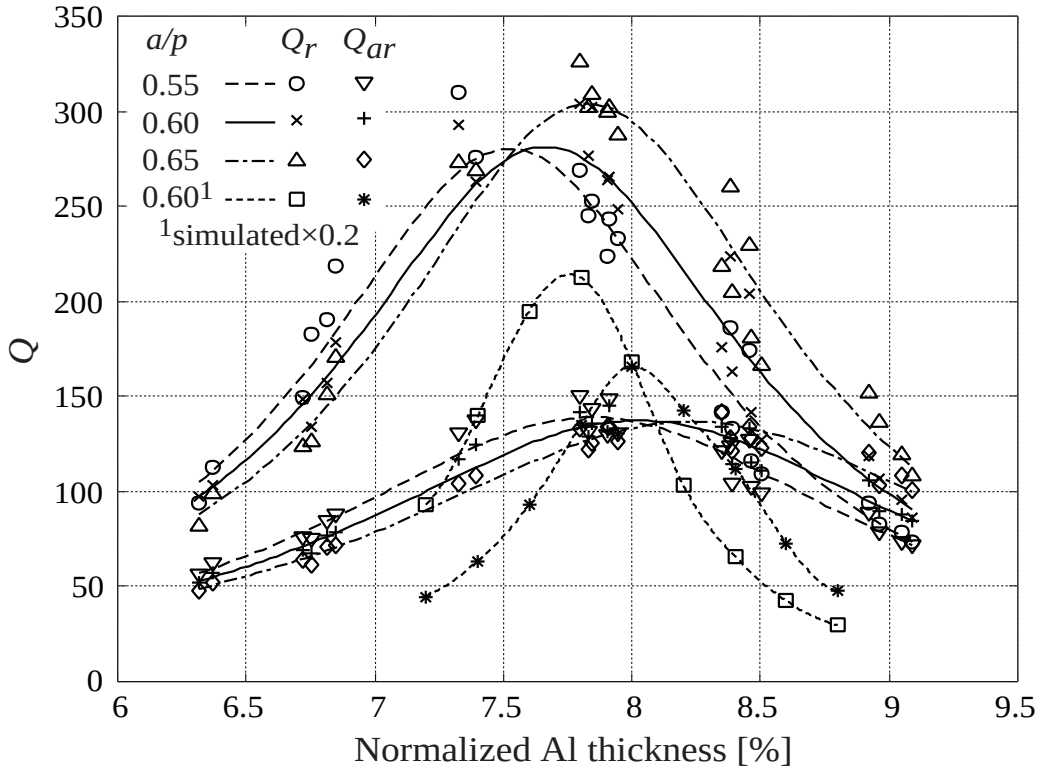

Figure 3.4: Measured Q at resonance (upper curves) and at antiresonance (lower curves) as a function of the Al electrode thickness for different a/p. The Q values are determined from test resonators with a 1:1 IDT in the 2.8 GHz frequency range. For comparison, the simulated curve is also plotted. The continuous curves are fitted to the measured and simulated points. Note that the simulated values have been scaled by a factor of 0.2.

3.5 Novel high-frequency bandpass filters utilizing the LLSAW mode

In Papers IV and V, LLSAW mode is applied to implement ladder-type bandpass filters for both the Bluetooth (2.45 GHz) and WLAN (5 GHz) bands. In particular, Paper IV is the first publication to report a filter based on the LLSAW mode on the YZ-$LiNbO_3$ substrate. Paper V reports the novel result of a bandpass filter for the WLAN frequency range with a center frequency above 5 GHz, fabricated using conventional optical lithography. The measured transmission response (measured on wafer) of this prototype filter, together with the measured admittances of the LLSAW resonators used in the filter, are plotted in Fig. 3.5. The resonators in the filter employ the fundamental LLSAW mode. The filter shows a commercially acceptable performance. It is expected that the filter performance may be further improved through the optimization of the design parameters, such as the acoustic aperture and number of fingers in the IDT for each resonator, and layout of the metallisations

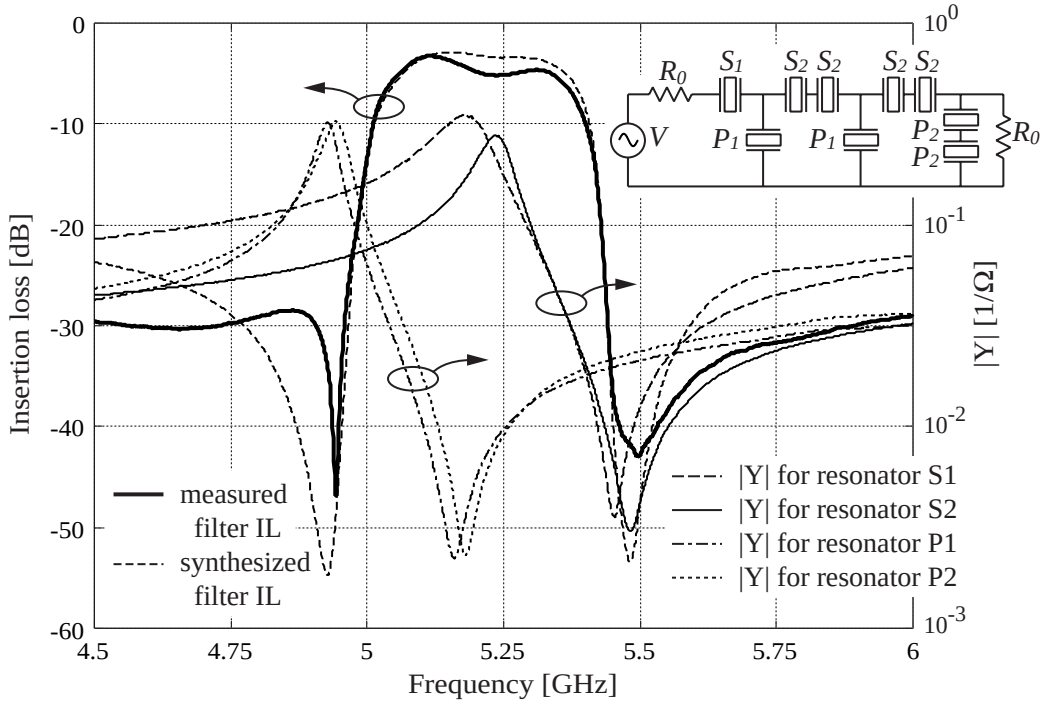

Figure 3.5: Measured insertion loss of an LLSAW filter together with the measured magnitudes of the admittances for the series (S) and parallel (P) LLSAW resonators. The effective Al electrode thickness is 965 Å. The ladder filter configuration employed is shown in the inset.

interconnecting the resonators.

In the design of the filters, mainly two complementing methods were used. One of the methods involves using the measured frequency responses of LLSAW test resonators and employing scaling techniques to obtain the structural resonator parameters needed for a filter with a given center frequency (method 1). The other method uses the FEM/BEM method for finite structures to numerically simulate the resonator responses necessary to synthesize the filter (method 2). The drawback of the rigorous computation is its slowness.

In the method 1, two scale factors for each resonator are used, one for the frequency and one for the admittance level. Using the scale factor for frequency, the response of an LLSAW resonator with operating frequency lower than the target frequency is scaled to the higher frequency range. To increase frequency by a factor of two amounts approximately to reducing all the dimensions of the resonator by the same factor. If all the dimensions of the resonator are decreased proportionally, the static and acoustic parts of admittance remain essentially unchanged. The second scale factor amounts to either adjusting the aperture from the value dictated by the scale factor for frequency, or adjusting the number of fingers in the resonator IDT. In the filters reported in Papers III and IV, the acoustic aperture is the same for all the

resonators, whereas in the filter reported in Paper V, also the aperture is varied. The drawback of increasing the acoustic aperture is the increase of resistive losses in the electrodes.

The two scale factors used in the method 1 are optimized such that the desired filter characteristics are achieved. From the geometrical parameters of the measured resonator and the optimized scale factors, the geometrical parameters for the resonators in the designed filter are deduced. In the process, the dependence of the resonance frequencies on the normalized Al electrode thickness is taken into account. This dependence is either numerically simulated or experimentally determined using test resonator measurements.

In Paper III, prototype filters with center frequencies around 2.8 GHz are reported. Filters with several different metallisation thicknesses and metallisation ratios for the resonators have been fabricated to determine their effect on the filter center frequency. As expected from the results for LLSAW resonators, it is found that the center frequency is much more sensitive to the Al electrode thickness than to the metallisation ratio. In fabrication, the metallisation thickness may be more accurately controlled than the metallisation ratio.

Comparing the Q values of the test resonators operating in the 2.8 GHz range, discussed in Paper III, with those operating in the 5.2 GHz regime, discussed in Paper V, the dependence of the resonator Q values on the operating frequency can be observed. Although the metallisation ratio, normalized thickness and normalized aperture for the test resonators in both frequency regimes are approximately equal, the resonators at 5.2 GHz clearly display lower Q values. This is attributed mostly to resistive losses in the Al electrodes. Furthermore, the resonator at 5.2 GHz with a 50λ aperture has a notably lower Q at resonance than the resonator with a 25λ aperture. This originates from the dramatic increase in the finger electrode resistance with increasing electrode length, leading to higher resistive losses in the electrodes. Contrary to the resonance, where the current in the electrodes is at the maximum, the Q at antiresonance, where the current is at the minimum, does not display such a decrease with increasing finger length.

The performance of the filters having center frequencies close to 2.5 GHz, 2.8 GHz and 5.2 GHz is summarized in Table 1. The relative 3 dB bandwidth of the 2.8 GHz filter is 4.7% and those of the 2.5 GHz and 5.2 GHz filters are 6.2% and 6.3%, respectively, indicating the range of bandwidths that may be obtained. The relative bandwidth of 6% achievable using LLSAW on YZ-$LiNbO_3$ is remarkably high. This compares favorably with 3.2% (4 dB bandwidth) and 5.0% (3 dB bandwidth) quoted in [162] and [46], respectively, for AlN-based FBAR ladder filters at 5.25 GHz. The filters in [162] and [46] employed SMR and membrane-type FBARs, respectively. In [46], it was necessary to use a specialized package with incorporated microstrip inductors to obtain the 5.0% bandwidth. Due to the high Q value of the FBARs (e.g., $Q = 913$ for resonance at 5.173 GHz [46]), minimum filter ILs of about 2.0 dB [162] and

Table 1: Performance of prototype LLSAW ladder filters in different frequency ranges. Column "Configuration" indicates the electrical connections of the resonators from input to output. S and P denote series and parallel resonator, respectively. When the series or parallel resonators in the filter are not identical, they are distinguished using a subindex. Number 2 in front of the letter denoting the resonator indicates series connection of two identical resonators.

Parameter					
f_0 [GHz]	Min IL [dB]	Relative 3 dB bandwidth [%]	Close-in selectivity [dB]	Configuration	Ref.
2.49	3.5	6.2	>20	P-S-P-P-S-P	Paper IV
2.80	2.3	4.7	>15	S_1-P_1-$2S_2$-P_1-S_1	Paper III
5.20	3.3	6.3	>25	S_1-P_1-$2S_2$-P_1 -$2S_2$-$2P_2$	Paper V

1.5 dB [46] were achieved. These are slightly better than the value 3.3 dB obtained for the LLSAW filter in Paper V.

The high bandwidth of the LLSAW filters is partly offset by the relatively low temperature stability of the LLSAW resonators. In [172] the TCF of LLSAW has been experimentally determined to be -105 ppm/K, using an LLSAW test resonator on YZ-$LiNbO_3$ with the normalized Al electrode thickness of 8% and $a/p = 0.7$. This value is higher than, e.g., that for the leaky SAW mode on 64°YX-$LiNbO_3$ (-79 and -81 ppm/K for free and metallized surfaces, respectively [32]). Hence, in the filter design, larger allowance for temperature variations is necessary when employing the LLSAW mode. The achieved stopband rejection of 25 dB is a very satisfactory value for a SAW ladder filter operating at 5.2 GHz. The stopband suppression level critically depends on the filter layout on the chip and, consequently, it needs to be carefully designed.

The results reported in Papers III–V confirm that LLSAW on YZ-$LiNbO_3$ is a viable propagation mode to be employed in low-loss, high-frequency, wide-band filters, enabling the fabrication of filters for frequencies beyond 5 GHz using conventional optical lithography. The LLSAW-based high-frequency filters may well find use in the current and future large-volume low-cost filter applications, in particular in WLAN systems.

4 Second-order effects affecting SAW ladder filter performance

This Chapter discusses the author's work in the development of a surface-acoustic-wave (SAW) antenna duplexer for the industrial-scientific-medical (ISM) band. In particular, in the research conducted in Paper VI, the emphasis is on the numerical modeling of the electromagnetic couplings in the package of the duplexer to predict the package effects on its performance. In addition, the results of laser-interferometric probing of the acoustic fields in the resonators which compose the two ladder filters in the duplexer are briefly discussed.

4.1 Packaging schemes for microwave acoustic filters

In mass production, bulk and surface acoustic wave filters are fabricated on wafers from three to six inches in diameter. The wafer is cut and each individual filter is then packaged and delivered to the customer. The hermetic package protects the active surface of the SAW chip from contamination and corrosion. This section briefly describes certain packaging schemes that are in use for SAW (and FBAR) RF filters.

In the 1990s, the dominant packaging method for RF SAW filters was to place the SAW chip inside a ceramic surface-mounted-device (SMD) package, using bond wires to establish the electrical connections between the chip and the package. Later, flip-chip packaging was introduced [35, 173], where the chip is assembled face down and the mechanical and electrical connections between the chip and package are established by small solder balls, e.g., gold bumps [22, 173]. For a reliable connection, the difference in the temperature coefficient of expansion for the substrate and that for the package base may not be too large to avoid excessive stress on the solder balls which can break the connection. In comparison with packages employing bond wires, flip-chip packages are generally smaller because the space-consuming bond pads in the package for bond-wire attachment are not required. However, both schemes use expensive ceramic packages; the price of the package may be comparable to or larger than the price of the chip inside.

The market demand for smaller component size is driving the development for higher miniaturization. Chip-size packaging (CSP) [35, 67], referring to packaging techniques where the size of the packaged chip is only marginally larger than the size of the chip alone, is a comparatively new packaging approach. In the packaging concept reported, e.g., in [67] the individual devices on the chip still need to be separated before attaching them into the package base. This is avoided in wafer-level CSP packaging schemes. The package must provide a cavity above the acoustically active areas of a SAW or FBAR device. For FBAR devices this is more readily achieved because the cavity does not need to be hermetically sealed. A recently introduced innovative wafer-level packaging technique [174] is based on bonding another wafer (cap wafer) on top of the active side of the SAW wafer using adhesive. This cap wafer

features etched enclosures that form the cavity over the active areas on the SAW wafer. After joining the wafers, the cap wafer is etched to expose pads for electric connection. Next, a layer to ensure the hermetic sealing is deposited onto the cap wafer. Only as the last step, the wafers are diced to separate the individual devices.

In a novel cost-effective wafer-level packaging concept (reported for FBAR devices), photo-epoxy is laid and patterned over a sacrificial layer to define the sides and top of the cavity [175]. The first intermediate epoxy layer features holes through which the underlying sacrificial layer is etched away to establish the cavity. The holes are sealed with an additional epoxy layer fabricated on top of the first epoxy layer. At this stage the devices are separated by dicing the wafer with a standard disc saw. The chips so fabricated may be used in modules or injection molding may be used to encompass the chip into an inexpensive plastic SMD package. Wafer-level CSP packaging will provide further reduction in size and cost.

The decreased size of the fully or partially packaged filter is useful especially when filters are used in multi-chip modules. Such a recent packaging scheme introduced to achieve a higher degree of integration at low cost includes multi-layer low-temperature co-fired ceramic (LTCC) modules [176, 177]. In this packaging method, active (e.g., low noise amplifiers) and passive components (e.g., SAW filters) are mounted and encapsulated on top of the module. The module contains feedthroughs carrying signals between the top and bottom surfaces of the module as well as buried interconnects between the components on the top surface of the module. The module may also encompass various passive functions, e.g., inductors and capacitors. The LTCC module may be connected to the printed circuit board either using solder balls (ball grid array) [178] or conductive adhesive. This way, modules with high degree of miniaturization and enhanced functionality, integrating RF SAW filters and front-end circuitry for a mobile phone into a single unit, with sizes smaller than 7×5 mm^2, have been realized [35].

4.2 Influence of electromagnetic couplings on filter response

The electrical response of a SAW ladder filter is not determined by the acoustoelectric characteristics of the resonators alone. There are parasitic electromagnetic couplings, e.g., between the metallisations on the SAW chip, between the metallisations of the package as well as between the metallisations on the chip and those of the package. These parasitic couplings may distort the transmission response of the filter and there may be considerable differences in the filter response as measured on wafer and after the packaging. As the frequency increases and the dimensions of the filter and package decrease the capacitive and inductive couplings in the package affect the filter response more prominently. Therefore, if the influence of the package can be estimated numerically, significant cost and time savings may be achieved as the simulation potentially allows to reduce the number of design and prototype fabrication cycles.

Interconnect metallisations of the resonators used to synthesize the bandpass ladder filter increase resistive losses and introduce additional series inductances [179]. Furthermore, there are capacitive couplings between the on-chip metallisations. For example, the contact pads at the input of the filter are capacitively connected to the contact pads at the output of the filter, causing capacitive feedthrough which decreases the stopband rejection level. In addition, there is capacitive connection between the metallisations on the signal path and the metallisations connected to the ground, causing a capacitive shunting effect [180]. These unwanted effects may increase the insertion loss of the filter.

Inductive couplings influence the stopband suppression level of ladder filters. Considering the close-in suppression, it can commonly be observed that, instead of the deep notch immediately below the passband frequencies, the measured filter transmission response is degraded and exhibits a peak. This is a result of inductive coupling between the input and output. At the frequency of the notch the magnitude of impedance of the parallel resonator is low, implying that a large current flows through the parallel resonator closest to the input, especially if it is not preceded by a series resonator. If the filter layout is symmetric and there is also a parallel resonator closest to the output, the current in the input loop may inductively couple to the corresponding low impedance output loop which leads to a decrease of the suppression level. Modeling these parasitic couplings due to the metallisations on the chip is reported for a SAW filter, e.g., in [181] and for an FBAR filter, e.g., in [36]. Recently, Lin *et al.* [182] and Kiwitt *et al.* [179] have implemented a complete model including both the on-chip and package metallisations. Electromagnetic modeling of an interdigital transducer (IDT), including the finger electrodes, have been reported both using the finite difference method [183] and the method of moments [184].

Instead of being completely detrimental, the package effects may also be exploited to improve the filter performance from that measured on wafer [46, 179, 185]. In the SMD ceramic multilayer package considered in Paper VI, the electrical connection between the SAW filter on the chip and the package is achieved by bond wires. The bond wire inductances may be used to improve the electrical matching and decrease the filter IL as well as increase the filter bandwidth. For a flip-chip package, the decreased mutual inductances between the connection bumps, as compared with the bond-wire connection, are expected to improve the stopband behaviour due to decreased inductive crosstalk. In a flip-chip package, inductors utilised to extend the filter bandwidth can be implemented as metallisations on the package [46].

The package capacitances and inductances, as well as on-chip capacitances and inductances [36], may give rise to low-Q-value resonances, in the same manner as in lumped element LC resonators [185, 186]. The frequency of this resonance may be conveniently located, e.g., to increase the rejection level of the filter far from passband.

4.3 Computation of electromagnetic couplings in a package of SAW filter

One of the goals of the studies presented in Paper VI was to numerically simulate the parasitic electromagnetic couplings in a package of an ISM SAW antenna duplexer. An antenna duplexer enables simultaneous transmission and reception of radio signals in two-way transceivers. The duplexer reported in Paper VI requires no additional passive components and both the transmission and reception filters are fabricated on the same chip to achieve high miniaturisation. On system level this offers the advantage of decreased board space and component count. However, it increases the complexity of modeling. The size of the ceramic SMD package for the duplexer is $5\times5\times1.5$ mm^3.

Although the effects of package capacitances and inductances on SAW filter performance have often been taken into account using estimates of varying accuracy [180], extensive modeling of the package of a SAW filter and extraction of the capacitances and inductances using rigorous computation, such as the procedure described in Paper VI, is still not quite common. In this work, the couplings between the conducting parts of the package are computed numerically from the known geometry and materials parameters of the package employing 3D models. The techniques employed here for the numerical evaluation of the package effects assume that the package dimensions are electrically small (significantly smaller than the wavelength of the electromagnetic wave [187]). It is also assumed that the effects of the electromagnetic couplings between the package and chip are small and, hence, may be ignored.

Within this Thesis, for a computation of the capacitance matrix, which expresses the capacitive couplings between the package metallisations, a software called FASTCAP [188–190] was employed. The software applies the boundary element method to the integral form of the Laplace equation assuming ideal conductors and linear, isotropic and piecewise homogeneous dielectric materials. In the equivalent-charge formulation employed, the charge density on the conductor surfaces and dielectric-dielectric interfaces is discretized through dividing the interfaces into small planar panels. The charge density on each small panel is taken to be constant. The conductor surfaces are required to be equipotential surfaces (static approximation) with prescribed potential, and the normal component of electric displacement is required to be continuous across the dielectric-dielectric interfaces. This results in a dense linear system of equations from which the unknown panel charges are solved. In the solution, a conjugate-residual style iterative method is utilized. Solution using Gaussian elimination would require on the order of N_p^3 operations, where N_p is the total number of panels used in the discretization. Acceleration of the iterative solution process by multipole and local expansions and by a preconditioner allows the solution to be computed at the cost of order NN_p operations, where N is the number of conductors. The model of the duplexer package for the extraction of the capacitance matrix is depicted in Fig. 4.1 (a).

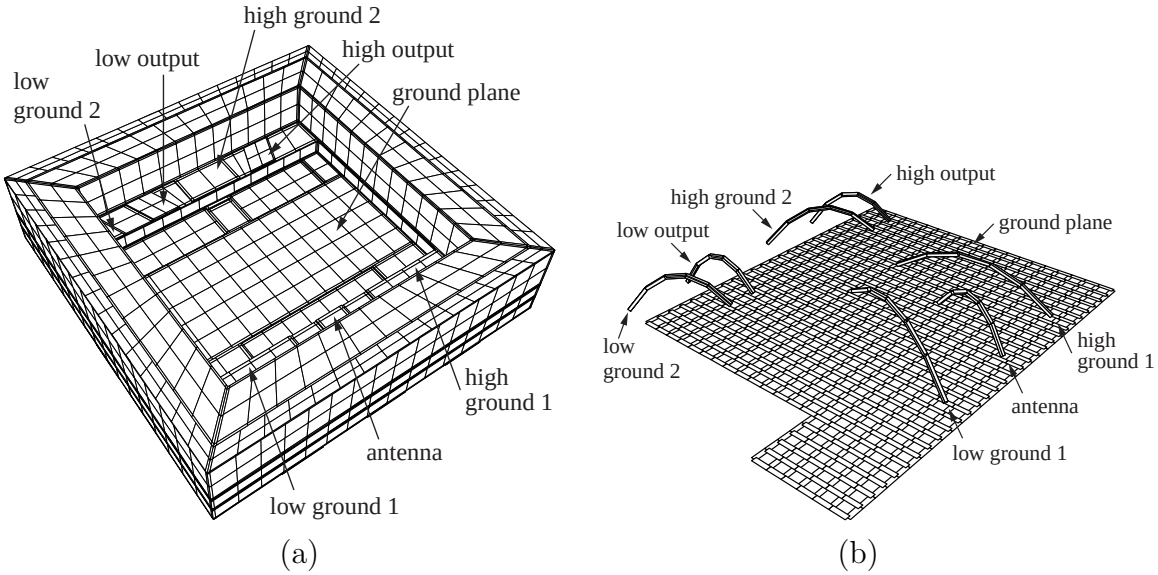

Figure 4.1: Models of duplexer package used in the numerical computation of the capacitance matrix (a) and impedance matrix (b). The grounded conductive lid of the package is not drawn. In the actual computation of the capacitance matrix, a finer discretization than that shown in (a) was used. In (b), the segments of the ground plane are drawn narrower than their actual width.

In the numerical computation of the inductances and resistances of the bond wires, a software named FASTHENRY [191, 192] was used. It employs the method of moments in discretization of the integral equation for current density and electric potential. The equation is derived under the assumption of sinusoidal steady-state excitation, magnetoquasistatic approximation and linear and isotropic conductors and magnetic media. The problem is reformulated using the mesh analysis approach to allow for an iterative solution. The model of the duplexer package for the extraction of the impedance matrix is displayed in Fig. 4.1 (b). The aluminum bond wires used in the duplexer are modeled using five consecutive straight segments with square cross-section of 30×30 μm^2, further subdivided adaptively into filaments (5×5 filaments per segment) in order to account for the skin and proximity effects. The tendency of the current at high frequencies to concentrate in the vicinity of the outer surface of the conductor is called the skin effect [193, 194]. This renders the resistances and self and mutual inductances frequency-dependent. As the current is assumed uniform in each filament, the cross-section of the filaments is taken smaller closer to the bond wire surface than in the interior regions to account for the skin effect in the modeling. The current distribution in a conductor is also affected by other nearby located current carrying conductors (proximity effect [195]). The influence of the discretization on the computed bond-wire impedance was investigated to ensure accurate results with moderate computation time. At frequencies around 1 GHz, the

skin depth is already much smaller than the diameter of the bond-wire. Therefore, the alternating current resistance of the bond wire equals several times the direct current resistance. The bond-wire resistance computed with FASTHENRY was also verified through comparison with resistance obtained from analytical formulas. The computed self-inductances of the bond wires are on the order of 1 nH and computed resistances (at the frequency of 1 GHz) are ca. 0.1-0.2 Ohm. However, the resistance caused by the attachment of the bond wire to the contact pads is dominating, being on order of 1 Ω. The model also includes two ground planes (Fig. 4.1 (b) shows only one of them). The frequency dependence of the self and mutual inductances within the comparatively narrow frequency range of interest around the passbands of the filters was found to be weak and, consequently, they were taken to be constants in the circuit simulation. The metallisations in the package further add to these inductances and resistances, although they were omitted in the model of the package employed in inductance extraction. The numerical modeling allows the evaluation of proposed package layouts and bonding schemes for optimizing the overall component performance.

After the numerical extraction of the inductances, capacitances and resistances, a unified model was formed in a form of an equivalent circuit describing the package and the filter on the chip. The interface between the chip and the equivalent circuit model is at the end of the bond wires attached to the bonding pads on the chip. The package parasitics are incorporated into the equivalent circuit as lumped elements. The SAW resonators are included in the model through their frequency-dependent impedances, computed using the modified COM model [196]. In addition to the self-inductances, also the mutual inductances between the bond wires were calculated and the relevant ones included into the equivalent circuit.

The equivalent circuit simulation was carried out using the Matlab software. To improve the correspondence between the measured and simulated filter responses, a fitting procedure was performed, using the computed values of the package parasitics as the initial values in the optimization. There are differences between the computed and the final fitted values of the package parasitics, owing to the fact that similar simulated filter response can be obtained for several different sets of values for the package parasitics in the equivalent circuit. Furthermore, in the equivalent circuit model, certain parasitic effects were omitted, such as inadequate grounding which may be modeled using a common-mode inductance to ground [197]. The measured and simulated transmission responses for the reception and transmission channels of the packaged duplexer are shown in Fig. 4.2. It is seen that the simulation fairly well predicts the relevant stopband behaviour. The discrepancies between the measured and simulated passband characteristics are mainly due to an acoustic loss mechanism briefly addressed in Section 4.4.

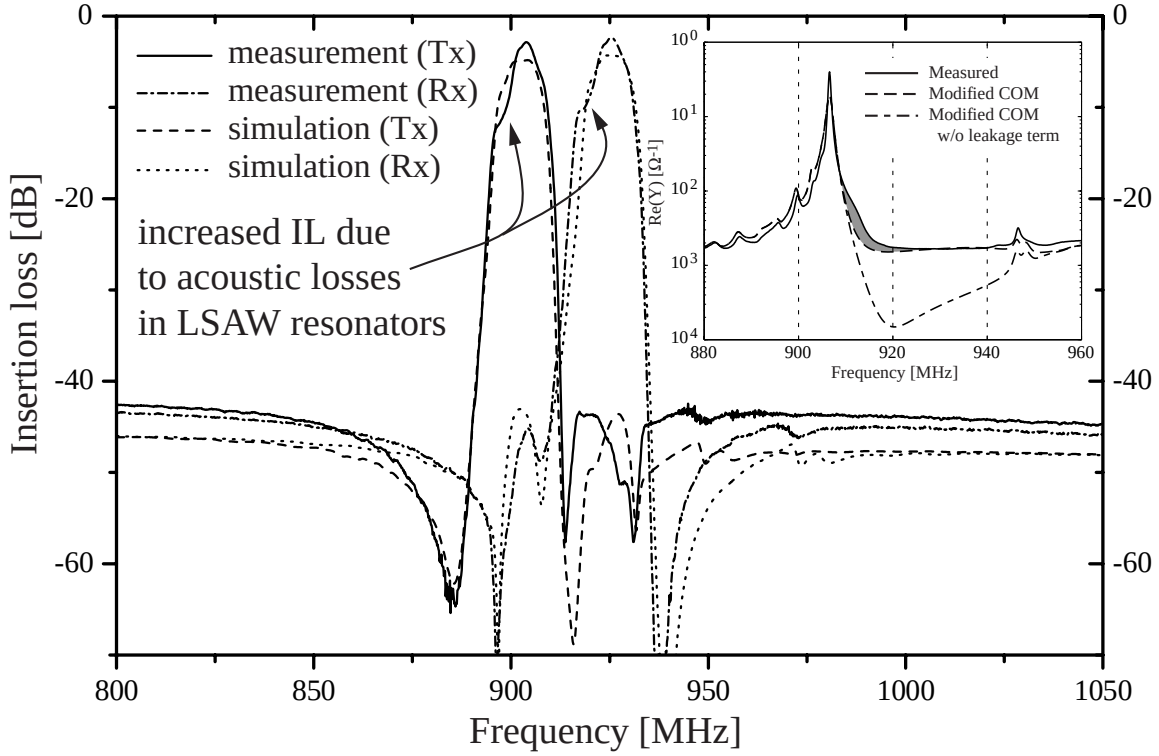

Figure 4.2: Simulated and measured frequency responses for the transmission and reception channels of the duplexer. The inset shows the measured conductance for a 1:3 IDT synchronous resonator as well as those simulated with a modified COM model [196] and fitted to the measurement.

4.4 Acoustic loss mechanism in leaky SAW resonators on 36°YX-$LiTaO_3$

The measured filter responses feature unexpected losses at the frequencies of the lower edge of the passbands (see Fig. 4.2). One of the aims of the research reported in Paper VI was to investigate and explain the cause for this discrepancy between the measured and simulated frequency responses. The discrepancy could not be explained as being a consequence of the packaging effects or an effect that could be modeled using the coupling-of-modes (COM) model applied in the resonator design. The synchronous one-port resonators in the ladder filters in the duplexer employed the leaky SAW mode on 36°YX-cut lithium tantalate and featured 1:3 IDTs to reduce the passband width.

To investigate the acoustic behaviour of the resonators in the ladder filter, a scanning laser interferometer [37] was used to image the acoustic fields on the substrate surface. In addition to the complete area of the chip, smaller portions were scanned to distinguish finer details. The investigation revealed an unprecedented acoustic loss mechanism, where the LSAW leaks from the resonator to the busbar and thereby

escapes the resonator [198]. This is a consequence of the anisotropy of the $LiTaO_3$ substrate. This loss mechanism manifests itself as an increased conductance at the stopband frequencies in the measured resonator response as shown in the inset in Fig. 4.2 (the gray region slightly above the series resonance frequency). The increased losses in the parallel resonators are responsible for the notches in the measured filter responses [199]. This loss mechanism was first explained and discussed in detail by Koskela *et al.* [199–201]. To solve the problem, dummy fingers may be used, where the tip of the electrode finger is not next to the busbar, but it faces another short finger extending from the busbar.

5 Summary and conclusions

The author's work presented in this Thesis has focused on using rigorous numerical methods for precise simulation of new physical effects in bulk and surface acoustic wave devices. The work considers aspects relevant to meeting the requirements posed by current and emerging applications in wireless communication: these include, in particular, high operating frequencies, low insertion loss and wide bandwidth. The novel results discussed in this work include: (i) Comprehensive FEM modeling of FBARs, especially the analysis of spurious anharmonic resonance modes (ii) Detailed study of propagation properties of LLSAW under a periodic Al electrode grating on YZ-$LiNbO_3$, optimization of the electrode geometry to achieve high-Q LLSAW resonators, and application of the LLSAW mode to realise high-frequency (2–5 GHz) ladder filters and (iii) One of the first rigorous electromagnetic modelings to study parasitic effects in the SAW filter transmission response caused by the ceramic package.

First, the modeling of thin-film bulk acoustic wave resonators (FBARs) using the finite element method (FEM) is considered. FBAR-based filters offer the advantage of high Q values, low temperature drift and high operating frequencies. The FEM used in the simulations is flexible and allows the modeling of complicated geometries and variations in the materials parameters. The powerful tailored 3D FEM software tool developed in this work and reported in Paper I features a unique combination of advanced numerical techniques. The software tool is highly useful in the analysis and design of FBARs. It enables one to study the effects of the resonator geometry, materials and various imperfections that may occur in the fabrication on the electrical response of the resonator. The results in Paper I manifest that the FEM software may be successfully applied to modeling FBARs. The performed 3D FEM simulations demonstrate that qualitative assessment of the influence of the electrode shape of a membrane-type FBAR on its electrical response is possible with manageable computational effort.

However, FEM simulation results can sometimes include artifacts caused by reflections of the waves from the artificial boundaries of the truncated computational mesh. Thus, to improve the accuracy of the modeling technique, the software should be extended such that it is capable of modeling the substrate as a half-space. This may be accomplished, e.g., through using the Green's function technique to model the substrate and employing the boundary element method (BEM) at the boundary of the FEM mesh to provide the interconnection to the FEM model. The FEM simulation tool described in Paper I is not limited to FBARs, but may be applied in modeling of a wide variety of piezoelectric devices, e.g., stacked crystal filter and monolithic crystal filter configurations, where BAW resonators are acoustically coupled.

To evaluate the quality of the piezoelectric material layer in an FBAR and to increase the accuracy of the modeling and design, it is beneficial to estimate the material parameters for the piezoelectric thin-film material. As FBARs are layered structures,

the dispersion behaviour of Lamb-wave modes propagating in such a structure is considered. In Paper II, a procedure to determine material parameters for the piezoelectric material layer is demonstrated, which is based on fitting computed dispersion curves to those measured using laser interferometer. Accurate results require precise knowledge of the layer thicknesses in the layer stack. The FBAR with acoustic mirror considered in Paper II has a larger number of material layers than its membrane-type counterpart and, correspondingly, a larger number of parameters affecting the dispersion curves. This suggests that the accuracy of the method would be higher when applied to membrane-type FBARs. To further improve the obtained fit between the experimental and computed dispersion curves, the optimisation of the material constants of the electrodes would possibly be required. However, increasing the number of optimized parameters will increase the computational cost. It is conceivable to choose the points on the dispersion curves differently for each material parameter to be optimized. The points would be chosen such that they display the highest sensitivity towards the variation of the material parameter considered. For stratified structures with a large number of layers, the technique yields the best results when used to complement other existing methods.

Second, the LLSAW mode on the YZ-cut $LiNbO_3$ substrate is studied. Because the velocity of LLSAW on YZ-$LiNbO_3$ under a grating with Al electrode thickness of 8% is approximately 6100 m/s, the LLSAW mode allows the fabrication of fundamental-mode resonators operating in the 5 GHz regime using optical lithography. In this work, the propagation properties of LLSAW in a periodic grating of Al electrodes are investigated using a periodic FEM/BEM simulator (Paper III). The variation of the Q values and resonance frequencies with the electrode geometry is derived for an infinite IDT. In addition, the performance of synchronous one-port LLSAW resonators is investigated in detail both theoretically and experimentally. In the numerical simulation, a software tool based on the FEM/BEM approach for finite structures is utilized. This work presents the first detailed study on the effects of Al electrode geometry on the resonator Q values and resonance frequencies, providing essential information for the design of LLSAW ladder filters. In the filter design, both rigorous numerical simulations and methods employing measured admittances of test resonators were used. Here, LLSAW ladder filters on the YZ-$LiNbO_3$ substrate are designed, fabricated and characterized, for the first time. As a highlight, Paper V reports a filter with a center frequency as high as 5.2 GHz. The LLSAW filters feature wide relative bandwidths around 5-6% and a comparatively low IL. In particular, the results demonstrate that the LLSAW mode on YZ-$LiNbO_3$ enables wide-band low-loss filters for wireless local area network frequencies at 5 GHz. As an especially attractive feature, the filters may be fabricated using conventional optical lithography which allows mass fabrication at low cost. Depending on the wireless system, FBAR-based filters with AlN as the piezoelectric material may have difficulties in attaining the required bandwidth. In this respect, LLSAW filters offer advantage with their comparatively large rela-

tive bandwidth of 5–6%. It remains to be seen whether commercial filters based on LLSAW for frequency bands within 2–5 GHz will appear or if the market will be dominated by FBAR filters.

Third, in the work reported in Paper VI, a modeling strategy is demonstrated to predict the transmission response of a SAW antenna duplexer. In particular, the influence of the package on the transmission response of the duplexer is investigated. In this work, rigorous numerical computation is employed to extract the inductive and capacitive couplings in the package. The modeling approach is valid only if the size of the package is sufficiently smaller than the wavelength of the electromagnetic wave. At higher frequencies, however, more rigorous electromagnetic analysis is necessary [182, 202, 203]. In the numerical computation of capacitance and impedance matrices, the charge density and current, respectively, are represented using pulse functions. A pulse function has difficulties to model the actual strongly varying charge density on the sharp edges of the conductors. The same applies to the strong variation of the current density close to the surface of the bond wire due to the skin effect. Hence, this may decrease the accuracy of the computed results unless special attention is paid to the discretization such that it accounts for the variations in the charge density or current. Foremost, to further improve the precision of the modeling, also the electromagnetic couplings between the on-chip and package metallizations need to be taken into account in the modeling. However, this is more important for the flip-chip configuration where the package and chip metallisations are considerably closer to each other than in the bond-wire configuration.

In an equivalent-circuit model of the duplexer, the package effects are included in terms of lumped elements. The applied modeling approach was able to predict the dominant features of the duplexer behaviour in the stopband. To explain the measured transmission behaviour in the passbands, the acoustic vibration amplitudes in the resonators constituting the filter were measured using a laser interferometer. The experiment displays a loss mechanism where the acoustic energy escapes the resonator explaining the increased insertion loss occurring at the frequencies of the lower passband edge of the prototype filters.

References

[1] D. P. Morgan, *Surface-Wave Devices for Signal Processing* (Elsevier, Amsterdam, 1991).

[2] C. K. Campbell, *Surface Acoustic Wave Devices for Mobile and Wireless Communications* (Academic Press, San Diego, 1998).

[3] K. Hashimoto, *Surface Acoustic Wave Devices in Telecommunications: Modelling and Simulation* (Springer, Berlin, 2000).

[4] IEEE Std 802.11a 1999(R2003), *Supplement to IEEE Standard for Information technology—Telecommunications and information exchange between systems—Local and metropolitan area networks—Specific requirements, Part 11: Wireless LAN Medium Access Control (MAC) and Physical Layer (PHY) specifications, High-speed Physical Layer in the 5 GHz Band* (The Institute of Electrical and Electronics Engineers, New York, 2003).

[5] R. Weigel, D. P. Morgan, J. M. Owens, A. Ballato, K. M. Lakin, K. Hashimoto, and C. C. W. Ruppel, "Microwave acoustic materials, devices, and applications", *IEEE Trans. Microwave Theory Tech.* **50**, 738–749 (2002).

[6] T. Ikeda, *Fundamentals of Piezoelectricity* (Oxford University Press, Oxford, 1996).

[7] T. W. Grudkowski, J. F. Black, T. M. Reeder, D. E. Cullen, and R. A. Wagner, "Fundamental-mode VHF/UHF miniature acoustic resonators and filters on silicon", *Appl. Phys. Lett.* **37**, 993–995 (1980).

[8] K. M. Lakin and J. S. Wang, "Acoustic bulk wave composite resonators", *Appl. Phys. Lett.* **38**, 125–127 (1981).

[9] E. A. Ash, "Surface wave grating reflectors and resonators", in *Proc. IEEE Int. Microwave Symposium*, 385–386 (1970).

[10] K. M. Lakin, T. Joseph, and D. Penunuri, "A surface acoustic wave planar resonator employing an interdigital electrode transducer", *Appl. Phys. Lett.* **25**, 363–365 (1974).

[11] K. M. Lakin, T. Joseph, and D. Penunuri, "Erratum: A surface acoustic wave planar resonator employing an interdigital electrode transducer", *Appl. Phys. Lett.* **26**, 351 (1975).

[12] E. J. Staples, "UHF surface acoustic wave resonators", in *Proc. 28th Annual Frequency Control Symposium*, 280–285 (1974).

[13] A. J. DeVries, T. Sreenivasan, S. Subramanian, and T. J. Wojcik, "Detailed description of a commercial surface-wave TV IF filter", in *Proc. IEEE Ultrasonics Symposium*, 147–152 (1974).

[14] Y. Satoh, O. Ikata, T. Miyashita, and H. Ohmori, "RF SAW filters", in *International Symposium on Acoustic Wave Devices for Future Mobile Communication Systems*, 125–132 (2001).

[15] P. Bradley, R. Ruby, J. D. Larson III, Y. Oshmyansky, and D. Figueredo, "A film bulk acoustic resonator (FBAR) duplexer for USPCS handset applications", in *IEEE MTT-S Digest*, 367–370 (2001).

[16] D. S. Burnett, *Finite Element Analysis* (Addison-Wesley, Reading, 1988).

[17] K.-J. Bathe, *Finite Element Procedures* (Prentice Hall, Englewood Cliffs, 1996).

[18] J. Molarius, J. Kaitila, T. Pensala, and M. Ylilammi, "Piezoelectric ZnO films by r.f. sputtering", *Journal of Materials Science: Materials in Electronics* **14**, 431–435 (2003).

[19] Lord Rayleigh, "On waves propagated along the plane surface of elastic solid", *Proc. London Math. Society* **17**, 4–11 (1885).

[20] B. A. Auld, *Acoustic Fields and Waves in Solids, Vol. 1* (John Wiley & Sons, New York, 1973).

[21] R. M. White and F. W. Voltmer, "Direct piezoelectric coupling to surface elastic waves", *Appl. Phys. Lett.* **7**, 314–316 (1965).

[22] H. Yatsuda, H. Iijima, K. Yabe, and O. Iijima, "Flip-chip STW filters in the range of 0.4 to 5 GHz", in *Proc. IEEE Ultrasonics Symposium*, 11–18 (2002).

[23] V. P. Plessky and C. S. Hartmann, "Characteristics of leaky SAWs on 36-$LiTaO_3$ in periodic structures of heavy electrodes", in *Proc. IEEE Ultrasonics Symposium*, 1239–1242 (1993).

[24] S. Lehtonen, J. Koskela, M. M. Salomaa, V. P. Plessky, M. Honkanen, and J. Turunen, "Surface acoustic wave impedance element filters for 5 GHz", *Appl. Phys. Lett.* **75**, 142–144 (1999).

[25] I. S. Didenko, F. S. Hickernell, and N. F. Naumenko, "The experimental and theoretical characterization of the SAW propagation properties for zinc oxide films on silicon carbide", *IEEE Trans. Ultrason., Ferroelect., Freq. Contr.* **47**, 179–187 (2000).

[26] N. F. Naumenko and I. S. Didenko, "High-velocity surface acoustic waves in diamond and sapphire with zinc oxide film", *Appl. Phys. Lett.* **75**, 3029–3031 (1999).

[27] E. Dogheche, V. Sadaune, X. Lansiaux, D. Remiens, and T. Gryba, "Thick $LiNbO_3$ layers on diamond-coated silicon for surface acoustic wave", *Appl. Phys. Lett.* **81**, 1329–1331 (2002).

[28] K. Kaya Y. Shibata and K. Akashi, "Epitaxial growth and surface-acoustic-wave properties of $LiTaO_3$ films grown by pulsed laser deposition", *Appl. Phys. Lett.* **62**, 3046–3048 (1993).

[29] K. Tsubouchi and N. Mikoshiba, "Zero-temperature-coefficient SAW devices on AlN epitaxial films", *IEEE Trans. Sonics Ultrasonics* **SU-32**, 634–644 (1985).

[30] Y. Kobayashi, Y. Hirao, K. Takeuchi, T. Usuki, K. Shibata, and Y. Shimizu, "New high-phase-velocity leaky surface acoustic wave mode on $LiTaO_3$ and $LiNbO_3$", *Jpn. J. Appl. Phys.* **34**, L1309–L1310 (1995).

[31] M. P. da Cunha, "Extended investigation on high velocity pseudo surface waves", *IEEE Trans. Ultrason., Ferroelect., Freq. Contr.* **44**, 548–556 (1997).

[32] T. Sato and H. Abe, "Propagation properties of longitudinal leaky surface waves on lithium tetraborate", *IEEE Trans. Ultrason., Ferroelect., Freq. Contr.* **45**, 136–151 (1998).

[33] A. Isobe, M. Hikita, and K. Asai, "Propagation characteristics of longitudinal leaky SAW in Al-grating structure", *IEEE Trans. Ultrason., Ferroelect., Freq. Contr.* **46**, 849–855 (1999).

[34] V. I. Grigorievski, "Fast leaky surface acoustic waves on lithium niobate and lithium tantalate", in *Proc. IEEE Ultrasonics Symposium*, 259–262 (2000).

[35] P. Selmeier, R. Grünwald, A. Przadka, H. Krüger, G. Feiertag, and C. Ruppel, "Recent advances in SAW packaging", in *Proc. IEEE Ultrasonics Symposium*, 283–292 (2001).

[36] R. F. Milsom, H.-P. Löbl, D. N. Peligrad, J.-W. Lobeek, A. Tuinhout, and R. H. ten Dolle, "Combined acoustic-electromagnetic simulation of thin-film bulk acoustic wave filters", in *Proc. IEEE Ultrasonics Symposium*, 963–968 (2002).

[37] J. V. Knuuttila, P. T. Tikka, and M. M. Salomaa, "Scanning Michelson interferometer for imaging surface acoustic wave fields", *Optics Lett.* **25**, 613–615 (2000).

[38] D. Royer and E. Dieulesaint, *Elastic Waves in Solids* I (Springer-Verlag, Berlin, 2000).

[39] K. F. Graff, *Wave Motion in Elastic Solids* (Dover Publications, New York, 1991).

[40] D. Salt, *Hy-Q handbook of Quartz Crystal Devices* (Van Nostrand Reinhold, Wokingham, 1987).

[41] W. G. Cady, "The piezo-electric resonator", *Proc. I.R.E.* **10**, 83–114 (1922).

[42] Y. Kagawa and T. Yamabuchi, "A finite element approach to electromechanical problems with an application to energy-trapped and surface-wave devices", *IEEE Trans. Sonics Ultrasonics* **SU-23**, 263–272 (1976).

[43] M. Naillon, R. H. Coursant, and F. Besnier, "Analysis of piezoelectric structures by a finite element method", *Acta Electronica* **25**, 341–362 (1983).

[44] S. H. Chang, N. N. Rogacheva, and C. C. Chou, "Analysis of methods for determining electromechanical coupling coefficients of piezoelectric elements", *IEEE Trans. Ultrason., Ferroelect., Freq. Contr.* **42**, 630–640 (1995).

[45] ANSI/IEEE Std 176-1987, *IEEE Standard on Piezoelectricity* (The Institute of Electrical and Electronics Engineers, New York, 1987).

[46] T. Nishihara, T. Yokoyama, T. Miyashita, and Y. Satoh, "High performance and miniature thin film bulk acoustic wave filters for 5 GHz", in *Proc. IEEE Ultrasonics Symposium*, 944–947 (2002).

[47] G. R. Kline and K. M. Lakin, "1.0-GHz thin-film bulk acoustic wave resonators on GaAs", *Appl. Phys. Lett.* **43**, 750–751 (1983).

[48] H. Satoh, Y. Ebata, H. Suzuki, and C. Narahara, "An air-gap type piezoelectric composite thin film resonator", in *Proc. 39th Annual Frequency Control Symposium*, 361–366 (1985).

[49] H. Satoh, H. Suzuki, C. Takahashi, C. Narahara, and Y. Ebata, "A 400 MHz one-chip oscillator using an air-gap type thin film resonator", in *Proc. IEEE Ultrasonics Symposium*, 363–368 (1987).

[50] M.-A. Dubois and P. Muralt, "Stress and piezoelectric properties of aluminum nitride thin films deposited onto metal electrodes by pulsed direct current reactive sputtering", *J. Appl. Phys.* **89**, 6389–6395 (2001).

[51] R. Lanz, *Piezoelectric Thin Films for Bulk Acoustic Wave Resonator Applications: from Processing to Microwave Filters*, PhD thesis (École Polytechnique Fédérale de Lausanne, Lausanne, 2004).

[52] K. M. Lakin, K. T. McCarron, and R. E. Rose, "Solidly mounted resonators and filters", in *Proc. IEEE Ultrasonics Symposium*, 905–908 (1995).

[53] W. E. Newell, "Face-mounted piezoelectric resonators", *Proc. IEEE* **53**, 575–581 (1965).

[54] K. M. Lakin, G. R. Kline, and K. T. McCarron, "Development of miniature filters for wireless applications", *IEEE Trans. Microwave Theory Tech.* **43**, 2933–2939 (1995).

[55] F. S. Hickernell, "Zinc oxide films for acoustoelectric device applications", *IEEE Trans. Sonics Ultrasonics* **SU-32**, 621–629 (1985).

[56] M. Ylilammi, J. Ellä, M. Partanen, and J. Kaitila, "Thin film bulk acoustic wave filter", *IEEE Trans. Ultrason., Ferroelect., Freq. Contr.* **49**, 535–539 (2002).

[57] J. Kaitila, M. Ylilammi, J. Molarius, J. Ellä, and T. Makkonen, "ZnO based thin film bulk acoustic wave filters for EGSM band", in *Proc. IEEE Ultrasonics Symposium*, 803–806 (2001).

[58] B. L. Olutade and W. D. Hunt, "Sensitivity analysis of a thin film bulk acoustic resonator ladder filter", in *Proc. IEEE Int. Freq. Contr. Symp.*, 737–742 (1997).

[59] Y. Miyasaka, S. Hoshino, and S. Takahashi, "Advances in structure and fabrication process for thin film acoustic resonator", in *Proc. IEEE Ultrasonics Symposium*, 385–393 (1987).

[60] K. M. Lakin, J. Belsick, J. F. McDonald, and K. T. McCarron, "Improved bulk wave resonator coupling coefficient for wide bandwidth filters", in *Proc. IEEE Ultrasonics Symposium*, 827–831 (2001).

[61] T. Shiosaki, T. Fukuichi, M. Tokuda, and A. Kawabata, "Temperature compensated high coupling and high quality factor ZnO/SiO_2 bulk wave resonators on high resistance substrates", in *Proc. IEEE Ultrasonics Symposium*, 405–410 (1984).

[62] S. Ohta, K. Nakamura, A. Doi, and Y. Ishida, "Temperature characteristics of solidly mounted piezoelectric thin film resonators", in *Proc. IEEE Ultrasonics Symposium*, 2011–2015 (2003).

[63] J. S. Wang and K. M. Lakin, "Low-temperature coefficient bulk acoustic wave composite resonators", *Appl. Phys. Lett.* **40**, 308–310 (1982).

[64] C. W. Seabury, P. H. Kobrin, and R. Addison, "Thin film ZnO based bulk acoustic mode filters", in *Proc. IEEE MTT-S Int. Microwave Symp.*, 181–184 (1997).

[65] M.-A. Dubois and P. Muralt, "Properties of aluminum nitride thin films for piezoelectric transducers and microwave filter applications", *Appl. Phys. Lett.* **74**, 3032–3034 (1999).

[66] R. B. Stokes, J. D. Crawford, and D. Cushman, "Monolithic bulk acoustic filters to X-band in GaAs", in *Proc. IEEE Ultrasonics Symposium*, 547–551 (1993).

[67] F. M. Pitschi, J. E. Kiwitt, B. Bader, and K. C. Wagner, "On the design of an FBAR PCS duplexer in LTCC chip-sized package", in *Proc. IEEE Ultrasonics Symposium*, 1525–1528 (2004).

[68] R. Takayama, H. Nakanishi, Y. Iwasaki, T. Inoue, and T. Kawasaki, "The approach to realize the characteristics of SAW resonator with the temperature compensation and steepness for PCS duplexer", in *Proc. IEEE Ultrasonics Symposium*, 385–388 (2003).

[69] D. Feld, P. Bradley, A. Barfknecht, and R. Ruby, "A wafer level encapsulated FBAR chip molded into a 2.0 mm x 1.6 mm plastic package for use as a PCS full band Tx filter", in *Proc. IEEE Ultrasonics Symposium*, 1798–1801 (2003).

[70] Q.-X. Su, P. Kirby, E. Komuro, M. Imura, Q. Zhang, and R. Whatmore, "Thin-film bulk acoustic resonators and filters using ZnO and lead-zirconium-titanate thin films", *IEEE Trans. Microwave Theory Tech.* **49**, 769–778 (2001).

[71] J. Kaitila, M. Ylilammi, J. Ellä, and R. Aigner, "Spurious resonance free bulk acoustic wave resonators", in *Proc. IEEE Ultrasonics Symposium*, 84–87 (2003).

[72] T. Makkonen, *Finite Element Modeling of Bulk Acoustic Wave Devices*, Licentiate thesis (Helsinki University of Technology, Espoo, 2001).

[73] R. D. Mindlin, "High frequency vibrations of piezoelectric crystal plates", *Int. J. Solids Structures* **8**, 895–906 (1972).

[74] P. C. Y. Lee, S. Syngellakis, and J. P. Hou, "A two-dimensional theory for high-frequency vibrations of piezoelectric crystal plates with or without electrodes", *J. Appl. Phys.* **61**, 1249–1262 (1987).

[75] K. M. Lakin, G. R. Kline, R. S. Ketcham, J. T. Martin, and K. T. McCarron, "Stacked crystal filters implemented with thin films", in *Proc. 43rd Annual Frequency Control Symposium*, 536–543 (1989).

[76] H. Zhang and E. S. Kim, "Air-backed Al/Zno/Al film bulk acoustic resonator without any support layer", in *Proc. IEEE Int. Freq. Contr. Symp.*, 20–26 (2002).

[77] Y.-K. Yong, J. T. Stewart, and A. Ballato, "A laminated plate theory for high frequency, piezoelectric thin-film resonators", *J. Appl. Phys.* **74**, 3028–3046 (1993).

[78] R. F. Milsom, D. T. Elliott, and M. Redwood, "Three-dimensional mode-matching theory of rectangular bar resonators using complex wave-numbers", in *Proc. 35th Annual Frequency Control Symposium*, 174–186 (1981).

[79] R. F. Milsom, "Two-dimensional theory of thin-film ZnO resonators on silicon", in *Proc. IEEE Ultrasonics Symposium*, 484–489 (1982).

[80] P. Lloyd and M. Redwood, "Finite-difference method for the investigation of solids and the evaluation of the equivalent-circuit characteristics of piezoelectric resonators I, II", *J. Acoust. Soc. Amer.* **39**, 346–361 (1966).

[81] E. Langer, S. Selberherr, P. A. Markowich, and C. A. Ringhofer, "Numerical analysis of acoustic wave generation in anisotropic piezoelectric materials", in *Proc. IEEE Ultrasonics Symposium*, 350–353 (1982).

[82] C. F. Campbell and R. J. Weber, "Two dimensional finite difference method for the analysis of piezoelectric devices", in *Proc. IEEE Ultrasonics Symposium*, 477–481 (1992).

[83] R. F. Milsom, D. T. Elliot, S. Terry-Wood, and M. Redwood, "Analysis and design of coupled-mode miniature bar resonators and monolithic filters", *IEEE Trans. Sonics Ultrasonics* **30**, 140–155 (1983).

[84] R. F. Milsom, J. E. Curran, S. L. Murray, S. Terry-Wood, and M. Redwood, "Effect of mesa-shaping on spurious modes in ZnO/Si bulk-wave composite resonators", in *Proc. IEEE Ultrasonics Symposium*, 498–503 (1983).

[85] K. M. Lakin, "Analysis of composite resonator geometries", in *Proc. 37th Annual Frequency Control Symposium*, 320–324 (1983).

[86] K. M. Lakin, "Numerical analysis of two dimensional thin film resonators", in *Proc. IEEE Int. Freq. Contr. Symp.*, 502–508 (1993).

[87] K. M. Lakin, G. R. Kline, and K. T. McCarron, "Thin film bulk acoustic wave filters for GPS", in *Proc. IEEE Ultrasonics Symposium*, 471–476 (1992).

[88] G. Carlotti, D. Fioretto, L. Palmieri, G. Socino, L. Verdini, and E. Verona, "Brillouin scattering by surface acoustic modes for elastic characterization of ZnO films", *IEEE Trans. Ultrason., Ferroelect., Freq. Contr.* **38**, 56–61 (1991).

[89] J. R. Heffelfinger, D. L. Medlin, and K. F. McCarty, "On the initial stages of AlN thin-film growth onto (0001) oriented Al_2O_3 substrates by molecular beam epitaxy", *J. Appl. Phys.* **85**, 466–472 (1999).

[90] H. Allik and T. J. R. Hughes, "Finite element method for piezoelectric vibration", *Int. J. Numer. Methods Eng.* **2**, 151–157 (1970).

[91] H. F. Tiersten, "Hamilton's principle for linear piezoelectric media", *Proc. IEEE* **55**, 1523–1524 (1967).

[92] H. F. Tiersten, *Linear Piezoelectric Plate Vibrations* (Plenum Press, New York, 1969).

[93] P. C. Y. Lee, "A variational principle for the equations of piezoelectromagnetism in elastic dielectric crystals", *J. Appl. Phys.* **69**, 7470–7473 (1991).

[94] Z. Zhang and Y.-K. Yong, "Numerical analysis of thickness shear thin film piezoelectric resonators using a laminated plate theory", *IEEE Trans. Ultrason., Ferroelect., Freq. Contr.* **42**, 734–746 (1995).

[95] P. Bettess, *Infinite Elements* (Penshaw Press, Sunderland, 1992).

[96] United States Patent 5,604,891, "3-D acoustic infinite element based on a prolate spheroidal multipole expansion", Lucent Technologies Inc, Murray Hill, USA, D. S. Burnett and R. L. Holford, 18 February 1997.

[97] D. S. Burnett, "A three-dimensional acoustic infinite element based on a prolate spheroidal multipole expansion", *J. Acoust. Soc. Amer.* **96**, 2798–2816 (1994).

[98] A. Reinhardt, V. Laude, M. Solal, S. Ballandras, and W. Steichen, "Investigation of spurious resonances in thin film bulk acoustic wave resonators", in *Proc. IEEE Ultrasonics Symposium*, 1698–1701 (2004).

[99] P. Ventura, J. M. Hodé, J. Desbois, and M. Solal, "Combined FEM and Green's function analysis of periodic SAW structure, application to the calculation of reflection and scattering parameters", *IEEE Trans. Ultrason., Ferroelect., Freq. Contr.* **48**, 1259–1274 (2001).

[100] P. Ventura, J.-M. Hodé, M. Solal, J. Desbois, and J. Ribbe, "Numerical methods for SAW propagation characterization", in *Proc. IEEE Ultrasonics Symposium*, 175–186 (1998).

[101] J. Koskela, V. P. Plessky, and M. M. Salomaa, "SAW/LSAW COM parameter extraction from computer experiments with harmonic admittance of a periodic array of electrodes", *IEEE Trans. Ultrason., Ferroelect., Freq. Contr.* **46**, 806–816 (1999).

[102] S. Ballandras, M. Wilm, P.-F. Edoa, A. Soufyane, V. Laude, W. Steichen, and R. Lardat, "Finite-element analysis of periodic piezoelectric transducers", *J. Appl. Phys.* **93**, 702–711 (2003).

[103] M. Wilm, S. Ballandras, A. Reinhardt, V. Laude, R. Lardat, R. Armati, W. Daniau, F. Lantéri, J.-F. Gelly, and O. Burat, "A 3-D mixed finite-element/boundary-element model for the simulation of periodic ultrasound transducers radiating in layered media", in *Proc. IEEE Ultrasonics Symposium*, 1654–1657 (2003).

[104] R. Lerch, "Simulation of piezoelectric devices by two- and three-dimensional finite elements", *IEEE Trans. Ultrason., Ferroelect., Freq. Contr.* **37**, 233–247 (1990).

[105] J. Kocbach, *Finite Element Modeling of Ultrasonic Piezoelectric Transducers*, PhD thesis (University of Bergen, Bergen, 2000).

[106] H. Allik, K. M. Webman, and J. T. Hunt, "Vibrational response of sonar transducers using piezoelectric finite elements", *J. Acoust. Soc. Amer.* **56**, 1782–1791 (1974).

[107] J. T. Stewart and D. S. Stevens, "Three dimensional finite element modeling of quartz crystal strip resonators", in *Proc. IEEE Int. Freq. Contr. Symp.*, 643–649 (1997).

[108] M. Koshiba, S. Mitobe, and M. Suzuki, "Finite-element solution of periodic waveguides for acoustic waves", *IEEE Trans. Ultrason., Ferroelect., Freq. Contr.* **34**, 472–477 (1987).

[109] P. Bauerschmidt, R. Lerch, J. Machui, W. Ruile, and G. Visintini, "Reflection and transmission coefficients of SAW in a periodic grating computed by finite element analysis", in *Proc. IEEE Ultrasonics Symposium*, 421–423 (1990).

[110] M. Buchner, W. Ruile, A. Dietz, and R. Dill, "FEM analysis of the reflection coefficient of SAWs in an infinite periodic array", in *Proc. IEEE Ultrasonics Symposium*, 371–375 (1991).

[111] M. Hofer, N. Finger, G. Kovacs, J. Schöberl, U. Langer, and R. Lerch, "Finite element simulation of bulk- and surface acoustic wave (SAW) interaction in SAW devices", in *Proc. IEEE Ultrasonics Symposium*, 53–56 (2002).

[112] W. Friedrich, R. Lerch, K. Prestele, and R. Soldner, "Simulations of piezoelectric Lamb wave delay lines using a finite element method", *IEEE Trans. Ultrason., Ferroelect., Freq. Contr.* **37**, 248–254 (1990).

[113] Y.-K. Yong and Y. Cho, "Numerical algorithms for solutions of large eigenvalue problems in piezoelectric resonators", *Int. J. Numer. Methods Eng.* **39**, 909–922 (1996).

[114] Y.-K. Yong and Y. Cho, "Algorithms for eigenvalue problems in piezoelectric finite element analyses", in *Proc. IEEE Ultrasonics Symposium*, 1057–1062 (1994).

[115] J. G. Lewis, "Implementation of the Gibbs-Poole-Stockmeyer and Gibbs-King algorithms", *ACM Transactions on Mathematical Software* **8**, 180–189 (1982).

[116] N. Guo, P. Cawley, and D. Hitchings, "The finite element analysis of the vibration characteristics of piezoelectric discs", *J. Sound and Vibration* **159**, 115–138 (1992).

[117] N. Guo and P. Cawley, "Measurement and prediction of the frequency spectrum of piezoelectric disks by modal analysis", *J. Acoust. Soc. Amer.* **92**, 3379–3388 (1992).

[118] Deptartment of Computational and Applied Mathematics, Rice University, ARPACK software (Online) [Referenced 5 April 2005] Available: http://www.caam.rice.edu/software/ARPACK.

[119] J. F. Rosenbaum, *Bulk Acoustic Wave Theory and Devices* (Artech House, Boston, 1988).

[120] W. Shockley, D. R. Curran, and D. J. Koneval, "Energy trapping and related studies of multiple electrode filter crystals", in *Proc. 17th Annual Frequency Control Symposium*, 88–126 (1963).

[121] H. F. Tiersten, J. F. McDonald, and P. K. Das, "Monolithic mosaic transducer utilizing trapped energy modes", *Appl. Phys. Lett.* **29**, 761–763 (1976).

[122] K. B. Yoo, H. Überall, and W. Williams, "Spurious resonances in bulk acoustic wave resonators", in *Proc. IEEE Ultrasonics Symposium*, 490–493 (1982).

[123] K. M. Lakin and K. G. Lakin, "Numerical analysis of thin film BAW resonators", in *Proc. IEEE Ultrasonics Symposium*, 74–79 (2003).

[124] H.-P. Loebl, C. Metzmacher, R. F. Milsom, R. Mauczok, W. Brand, P. Lok, F. van Straten, and A. Tuinhout, "Low-level effects in SBARs and their application to device optimisation", in *Proc. IEEE Ultrasonics Symposium*, 182–186 (2003).

[125] J. Xia, S. Burns, M. Porter, T. Xue, G. Liu, R. Wyse, and C. Thielen, "A micromachined sensor array using thin film resonators", in *Proc. IEEE Int. Freq. Contr. Symp.*, 879–884 (1995).

[126] R. F. Milsom, H.-P. Löbl, C. Metzmacher, P. Lok, A. Tuinhout, and F. van Straten, "2D model of solidly-mounted and membrane BAW devices", in *Proc. IEEE Ultrasonics Symposium*, 1802–1807 (2003).

[127] E. E. Antonova and P. P. Silvester, "Finite elements for piezoelectric vibrations with open electric boundaries", *IEEE Trans. Ultrason., Ferroelect., Freq. Contr.* **44**, 548–556 (1997).

[128] European Patent Application EP 1 041 717 A2, "Bulk acoustic wave resonator with improved lateral mode suppression", Agilent Technologies Inc, Palo Alto, USA, J. D. Larson III, R. C. Ruby, and P. Bradley, 4 October 2000.

[129] United States Patent 6,693,500 B2, "Film bulk acoustic resonator with improved lateral mode suppression", Samsung Electro-Mechanics Ltd, Suwon, South Korea, D. Y. Yang and H. W. Kim, 17 February 2004.

[130] International Patent WO 01/06647 A1, "Resonator structure and a filter comprising such a resonator structure", Nokia Mobile Phones Ltd, Espoo, Finland, J. Kaitila, M. Ylilammi, and J. Ellä, 25 January 2001.

[131] K. Hirama, Y. Aoyama, and M. Naito, "AT-cut quartz resonators with inverted-mesa electrodes", *Jpn. J. Appl. Phys.* **36**, 6432–6436 (1997).

[132] M. J. Lowe, "Matrix techniques for modeling ultrasonic waves in multilayered media", *IEEE Trans. Ultrason., Ferroelect., Freq. Contr.* **42**, 525–542 (1995).

[133] J. T. Stewart and Y.-K. Yong, "Exact analysis of the propagation of acoustic waves in multilayered anisotropic piezoelectric plates", *IEEE Trans. Ultrason., Ferroelect., Freq. Contr.* **41**, 375–390 (1994).

[134] A. H. Fahmy and E. L. Adler, "Propagation of acoustic surface waves in multilayers: A matrix description", *Appl. Phys. Lett.* **22**, 495–497 (1973).

[135] E. L. Adler, "Matrix methods applied to acoustic waves in multilayers", *IEEE Trans. Ultrason., Ferroelect., Freq. Contr.* **37**, 485–490 (1990).

[136] Th. Pastureaud, V. Laude, and S. Ballandras, "Stable scattering-matrix method for surface acoustic waves in piezoelectric multilayers", *Appl. Phys. Lett.* **80**, 2544–2546 (2002).

[137] K. Tsubouchi, K. Sugai, and N. Mikoshiba, "AlN material constants evaluation and SAW properties on AlN/Al_2O_3 and AlN/Si", in *Proc. IEEE Ultrasonics Symposium*, 375–380 (1981).

[138] C. Deger, E. Born, H. Angerer, O. Ambacher, M. Stutzmann, J. Hornsteiner, E. Riha, and G. Fischerauer, "Sound velocity of $Al_xGa_{1-x}N$ thin films obtained by surface acoustic-wave measurements", *Appl. Phys. Lett.* **72**, 2400–2402 (1998).

[139] R. S. Wagers, "PVF_2 elastic constants evaluation", in *Proc. IEEE Ultrasonics Symposium*, 464–469 (1980).

[140] J. E. Graebner, "Optical scanning interferometer for dynamic imaging of high-frequency surface motion", in *Proc. IEEE Ultrasonics Symposium*, 733–736 (2000).

[141] G. G. Fattinger and P. T. Tikka, "Laser measurements and simulations of FBAR dispersion relation", in *Proc. IEEE MTT-S Int. Microwave Symp.*, 371–374 (2001).

[142] W. H. Press, S. A. Teukolsky, W. T. Vetterling, and B. P. Flannery, *Numerical Recipes in C: The Art of Scientific Computing*, 2nd edition (Cambridge University Press, Cambridge, 1992).

[143] A. L. Kholkin, Ch. Wütchrich, D. V. Taylor, and N. Setter, "Interferometric measurements of electric field-induced displacements in piezoelectric thin films", *Rev. Sci. Instrum.* **67**, 1935–1941 (1996).

[144] T. Sato and H. Abe, "SAW device applications of longitudinal leaky surface waves on lithium tetraborate", *IEEE Trans. Ultrason., Ferroelect., Freq. Contr.* **45**, 1506–1516 (1998).

[145] T. Sato and H. Abe, "Propagation of longitudinal leaky surface waves under periodic metal grating structure on lithium tetraborate", *IEEE Trans. Ultrason., Ferroelect., Freq. Contr.* **45**, 394–408 (1998).

[146] S. Tonami, A. Nishikata, and Y. Shimizu, "Characteristics of leaky surface acoustic waves propagating on $LiNbO_3$ and $LiTaO_3$ substrates", *Jpn. J. Appl. Phys.* **34**, 2664–2667 (1995).

[147] Y. Kobayashi, N. Tanaka, K. Matsui, H. Okano, T. Usuki, and K. Shibata, "1.9 GHz-band surface acoustic wave device using second leaky mode on $LiTaO_3$", *Jpn. J. Appl. Phys.* **35**, 2987–2990 (1996).

[148] N. Naumenko and B. Abbott, "Optimized cut of lithium niobate for HVPSAW filters with different metalization ratio in element resonators", in *Proc. IEEE Ultrasonics Symposium*, 1213–1217 (2004).

[149] A. N. Darinskii, I. S. Didenko, and N. F. Naumenko, ""Fast" quasilongitudinal sagittally polarized surface waves in layer-substrate structures", *J. Acoust. Soc. Amer.* **107**, 2351–2359 (2000).

[150] Y. V. Gulyaev, V. I. Grigorievski, and V. P. Plessky, "Longitudinal leaky surface acoustic waves in periodic systems of metal electrodes on lithium niobate", in *Proc. IEEE Ultrasonics Symposium*, 2118–2121 (2003).

[151] T. Makkonen, V. P. Plessky, W. Steichen, S. Chamaly, C. Poirel, M. Solal, and M. M. Salomaa, "Properties of LLSAW on YZ-cut $LiNbO_3$: Modeling and experiment", in *Proc. IEEE Ultrasonics Symposium*, 613–616 (2003).

[152] D.-P. Chen and H. A. Haus, "Analysis of metal-strip SAW gratings and transducers", *IEEE Trans. Sonics Ultrasonics* **SU-32**, 395–408 (1985).

[153] H. A. Haus and W. Huang, "Coupled-mode theory", *Proc. IEEE* **79**, 1505–1518 (1991).

[154] P. V. Wright, "A new generalized modeling of SAW transducers and gratings", in *Proc. 43rd Annual Frequency Control Symposium*, 596–605 (1989).

[155] V. Plessky and J. Koskela, "Coupling-of-modes analysis of SAW devices", *International Journal of High Speed Electronics and Systems* **10**, 867–947 (2000).

[156] B. P. Abbott and K. Hashimoto, "A couling-of-modes formalism for surface transverse wave devices", in *Proc. IEEE Ultrasonics Symposium*, 239–245 (1995).

[157] J. Koskela, *Modeling SAW Devices Including Mass-Loading Effects*, Licentiate thesis (Helsinki University of Technology, Espoo, 1998).

[158] P. Ventura, J. M. Hodé, and M. Solal, "A new efficient combined FEM and periodic Green's function formalism for the analysis of periodic SAW structures", in *Proc. IEEE Ultrasonics Symposium*, 263–268 (1995).

[159] R. F. Milsom, N. H. C. Reilly, and M. Redwood, "Analysis of generation and detection of surface and bulk acoustic waves by interdigital transducers", *IEEE Trans. Sonics Ultrasonics* **24**, 147–166 (1977).

[160] A. R. Baghai-Wadji, H. Reichinger, H. Zidek, and Ch. Mecklenbräuker, "Green's function applications in SAW devices", in *Proc. IEEE Ultrasonics Symposium*, 11–20 (1991).

[161] V. P. Plessky and T. Thorvaldsson, "Periodic Green's functions analysis of SAW and leaky SAW propagation in a periodic system of electrodes on a piezoelectric crystal", *IEEE Trans. Ultrason., Ferroelect., Freq. Contr.* **42**, 280–293 (1995).

[162] G. G. Fattinger, J. Kaitila, R. Aigner, and W. Nessler, "Thin film bulk acoustic wave devices for applications at 5.2 GHz", in *Proc. IEEE Ultrasonics Symposium*, 174–177 (2003).

[163] P. M. Smith, "Dyadic Green's functions for multi-layer SAW substrates", *IEEE Trans. Ultrason., Ferroelect., Freq. Contr.* **48**, 171–179 (2001).

[164] V. Plessky, T. Makkonen, and M. M. Salomaa, "Leaky SAW in an isotropic substrate with thick electrodes", in *Proc. IEEE Ultrasonics Symposium*, 239–242 (2001).

[165] M. Solal, V. Plessky, R. Lardat, T. Makkonen, T. Pastureaud, W. Steichen, and M. M. Salomaa, "Existence of harmonic metal thickness mode propagation for longitudinal leaky waves", in *Proc. IEEE Ultrasonics Symposium*, 1207–1212 (2004).

[166] Y. Kobayashi, N. Tanaka, Y. Baba, H. Okano, T. Usuki, K. Shibata, and Y. Shimizu, "GHz-band surface acoustic wave devices using the second leaky mode on $LiTaO_3$ and $LiNbO_3$", *Jpn. J. Appl. Phys.* **36**, 6083–6087 (1997).

[167] A. R. Baghai-Wadji and A. A. Maradudin, "Shear horizontal surface acoustic waves on large amplitude gratings", *Appl. Phys. Lett.* **59**, 1841–1843 (1991).

[168] V. Laude, A. Khelif, Th. Pastureaud, and S. Ballandras, "Generally polarized acoustic waves trapped by high aspect ratio electrode gratings at the surface of a piezoelectric material", *J. Appl. Phys.* **90**, 2492–2497 (2001).

[169] V. P. Plessky, "SAW impedance elements", *IEEE Trans. Ultrason., Ferroelect., Freq. Contr.* **42**, 870–875 (1995).

[170] V. P. Plessky, S. N. Kondratiev, and C. Lambert, "Reduced passband ladder type SAW impedance element filters on strong piezoelectric substrates", in *Proc. IEEE Ultrasonics Symposium*, 11–14 (1996).

[171] O. Holmgren, J. V. Knuuttila, T. Makkonen, K. Kokkonen, V. P. Plessky, W. Steichen, M. Solal, and M. M. Salomaa, "Imaging surface-acoustic fields in a longitudinal leaky wave resonator", *Appl. Phys. Lett.* **86**, 024101 (2005).

[172] T. Pastureaud, S. Ballandras, and W. Steichen, "Prediction of the thermal sensitivity of surface acoustic waves excited under a periodic grating of electrodes", in *Proc. IEEE Ultrasonics Symposium*, 200–203 (2003).

[173] H. Yatsuda, T. Horishima, T. Eimura, and T. Ooiwa, "Miniaturized SAW filters using a flip-chip technique", *IEEE Trans. Ultrason., Ferroelect., Freq. Contr.* **43**, 125–130 (1996).

[174] M. Goetz and C. Jones, "Chip scale packaging techniques for RF SAW devices", in *Proc. IEEE/SEMI Electronics Manufacturing Technology Symposium*, 63–66 (2002).

[175] M. Franosch, K.-G. Oppermann, A. Meckes, W. Nessler, and R. Aigner, "Wafer-level-package for bulk acoustic wave (BAW) filters", in *Proc. IEEE MTT-S Int. Microwave Symp.*, 493–496 (2004).

[176] J. Heyen, T. von Kerssenbrock, A. Chernyakov, P. Heide, and A. F. Jacob, "Novel LTCC/BGA modules for highly integrated millimeter-wave transceivers", *IEEE Transactions on Microwave Theory and Techniques* **51**, 2589–2596 (2003).

[177] H. Jantunen, T. Kangasvieri, J. Vähäkangas, and S. Leppävuori, "Design aspects of microwave components with LTCC technique", *Journal of the European Ceramic Society* **23**, 2541–2548 (2003).

[178] M. P. R. Panicker, D. Douriet, M. S. Hyslop, and N. L. Greenman, "Ball grid arrays: a DC to 31.5 GHz low cost packaging solution for microwave and mm-wave MMICs", *Microwave Journal* **41**, 158–168 (1998).

[179] J. Kiwitt, F. M. Pitschi, K. Wagner, and M. Lorenz, "Novel approaches to the electromagnetic design of CSSP RF filters with improved selectivity", in *Proc. IEEE Ultrasonics Symposium*, 1992–1995 (2004).

[180] G. Fischerauer, D. Gogl, R. Weigel, and P. Russer, "Investigation of parasitic effects in multi-transducer SAW RF filters", in *Proc. IEEE Ultrasonics Symposium*, 241–244 (1994).

[181] J. J. Caron and S. Malocha, "Electrical parasitic modeling in SAW RF filters", in *Proc. IEEE Ultrasonics Symposium*, 361–346 (2002).

[182] S.-H. Lin, K.-H. Lin, S.-C. Chiu, and C.-Y. Chen, "Full wave simulation of SAW filter package and SAW pattern inside package", in *Proc. IEEE Ultrasonics Symposium*, 2089–2092 (2003).

[183] D. Jatkar and B. Beker, "Effects of package parasitics on the performance of SAW filters", *IEEE Trans. Ultrason., Ferroelect., Freq. Contr.* **43**, 1187–1194 (1996).

[184] S. Zhgoon, K. Bhattacharjee, A. Loseu, J. Rao, and J. Flowers, "Modeling of electromagnetic and acoustical properties of RF SAW filters from on-chip layout including all electrodes and comparison with experimental data", in *Proc. IEEE Ultrasonics Symposium*, 1914–1917 (2004).

[185] H. Yatsuda, "Modeling of parasitic effects for flip-chip SAW filters", in *Proc. IEEE Ultrasonics Symposium*, 143–146 (1997).

[186] S. Mineyoshi, O. Kawachi, M. Ueda, Y. Fujiwara, H. Furusato, and O. Ikata, "Analysis and optimal SAW ladder filter design including bonding wire and package impedance", in *Proc. IEEE Ultrasonics Symposium*, 175–178 (1997).

[187] C.-T. Tsai, "Package inductance characterization at high frequencies", *IEEE Transactions on Components, Packaging and Manufacturing Technology-Part B: Advanced Packaging* **17**, 175–181 (1994).

[188] K. Nabors and J. White, "Fastcap: A multipole accelerated 3-D capacitance extraction program", *IEEE Transactions on Computer-Aided Design* **10**, 1447–1459 (1991).

[189] K. Nabors, S. Kim, J. White, and S. Senturia, *FastCap USER'S GUIDE*, Research Laboratory of Electronics, Department of Electrical Engineering and Computer Science, Massachusetts Institute of Technology, Cambridge (1992).

[190] K. Nabors and J. White, "Multipole-accelerated capacitance extraction algorithms for 3-D structures with multiple dielectrics", *IEEE Transactions on Circuits and Systems-I: Fundamental Theory and Applications* **39**, 946–954 (1992).

[191] M. Kamon, C. Smithhisler, and J. White, *FastHenry USER'S GUIDE*, Research Laboratory of Electronics, Department of Electrical Engineering and Computer Science, Massachusetts Institute of Technology, Cambridge (1994).

[192] M. Kamon, M. J. Tsuk, and J. K. White, "Fasthenry: A multipole-accelerated 3-D inductance extraction program", *IEEE Transactions on Microwave Theory and Techniques* **42**, 1750–1758 (1994).

[193] J. D. Cockcroft, "Skin effect in rectangular conductors at high frequencies", *Proc. Royal Soc.* **122**, 533–542 (1929).

[194] H. A. Wheeler, "Formulas for the skin effect", *Proc. IRE* **30**, 412–424 (1942).

[195] J. R. Carson, "Wave propagation over parallel wires: the proximity effect", *Phil. Mag.* **41**, 607–633 (1921).

[196] K. Honkanen, J. Koskela, V. P. Plessky, and M. M. Salomaa, "Parasitic BAW excitation in LSAW transducers", in *Proc. IEEE Ultrasonics Symposium*, 949–952 (1998).

[197] P. Dufilié and J. Desbois, "Modeling of feedthrough and ground loops in SAW filters", in *Proc. IEEE Ultrasonics Symposium*, 223–226 (1993).

[198] J. V. Knuuttila, P. T. Tikka, C. S. Hartmann, V. P. Plessky, and M. M. Salomaa, "Anomalous asymmetric acoustic radiation in low-loss SAW filters", *Electronics Lett.* **35**, 1115–1116 (1999).

[199] J. Koskela, J. V. Knuuttila, T. Makkonen, V. P. Plessky, and M. M. Salomaa, "Acoustic loss mechanisms in leaky SAW resonators on lithium tantalate", *IEEE Trans. Ultrason., Ferroelect., Freq. Contr.* **48**, 1517–1526 (2001).

[200] J. Koskela, J. V. Knuuttila, P. T. Tikka, C. S. Hartmann, V. P. Plessky, and M. M. Salomaa, "Mechanism for acoustic leakage in surface-acoustic wave resonators on rotated Y-cut lithium tantalate substrate", *Appl. Phys. Lett.* **75**, 2683–2685 (1999).

[201] J. Koskela, *Analysis and Modeling of Surface-Acoustic Wave Resonators*, PhD thesis (Helsinki University of Technology, Espoo, 2000).

[202] C. Finch, X. Yang, T. Wu, and B. Abbott, "Full-wave analysis of RF SAW filter packaging", in *Proc. IEEE Ultrasonics Symposium*, 81–84 (2001).

[203] H. Dong, T. X. Wu, K. S. Cheema, B. P. Abbott, C. A. Finch, and H. Foo, "Design of miniaturized RF SAW duplexer package", *IEEE Trans. Ultrason., Ferroelect., Freq. Contr.* **51**, 849–858 (2004).

Abstracts of publications I–VI

I A finite element method (FEM) formulation is presented for the numerical solution of the electroelastic equations that govern the linear forced vibrations of piezoelectric media. A harmonic time dependence is assumed. Both of the approaches, that of solving the field problem (harmonic analysis) and that of solving the corresponding eigenvalue problem (modal analysis), are described.

A FEM software package has been created from scratch. Important aspects central to the efficient implementation of FEM are explained, such as memory management and solving the generalized piezoelectric eigenvalue problem. Algorithms for reducing the required computer memory through optimization of the matrix profile, as well as Lanczos algorithm for the solution of the eigenvalue problem are linked into the software from external numerical libraries.

Our FEM software is applied to detailed numerical modeling of thin-film bulk acoustic wave (BAW) composite resonators. Comparison of results from 2D and full 3D simulations of a resonator are presented. In particular, 3D simulations are used to investigate the effect of the top electrode shape on the resonator electrical response. The validity of the modeling technique is demonstrated by comparing the simulated and measured displacement profiles at several frequencies. The results show that useful information on the performance of the thin-film resonators can be obtained even with relatively coarse meshes and, consequently, moderate computational resources.

II The dispersion curves of Lamb-wave modes propagating along a multilayer structure are important for the operation of thin-film bulk acoustic wave (BAW) devices. For instance, the behavior of the side resonances that may contaminate the electrical response of a thin-film BAW resonator depends on the dispersion relation of the layer stack. Because the dispersion behavior depends on the materials parameters (and thicknesses) of the layers in the structure, measurement of the dispersion curves provides a tool for determining the materials parameters of thin films. We have determined the dispersion curves for a multilayer structure through measuring the mechanical displacement profiles over the top electrode of a thin-film BAW resonator at several frequencies using a homodyne Michelson laser interferometer. The layer thicknesses are obtained using scanning electron microscope (SEM) measurements. In the numerical computation of the dispersion curves, the piezoelectricity and full anisotropy of the materials are taken into account. The materials parameters of the piezoelectric layer are determined through fitting the measured and computed dispersion curves.

III The high phase velocity (above 6100 m/s in an Al grating on $LiNbO_3$) of the longitudinal leaky SAW (LLSAW) mode makes it attractive for application in high frequency SAW ladder filters in the 2–5 GHz range. We investigate the dependence of one-port synchronous LLSAW resonator performance on YZ-$LiNbO_3$

on the metallization thickness and metallization ratio, both experimentally and theoretically. Our results indicate a strong dependence of the Q factor and resonance frequency on the aluminum thickness, with the optimal thickness that produces the highest Q values being about 8%. The optimal thickness increases with the metallization ratio. The observed behavior is interpreted with the help of simulations using a combined FEM/BEM method. As an application, bandpass filters have been fabricated in the 2.8 GHz frequency regime, based on longitudinal leaky SAWs. The synchronous resonators constituting the ladder filters operate in the fundamental mode. The filters feature low insertion losses below 3 dB and wide relative passbands of 4.5–5%.

IV The recently discovered "longitudinal leaky" surface acoustic wave on YZ-cut lithium niobate has been used to implement low-loss bandpass filters operating in the 2.5-GHz Bluetooth frequency range. The filter is of the ladder type, employing synchronous resonators as building blocks. Resonator Q-values above 300 have been measured. The filter features a center frequency of 2491 MHz, a minimum insertion loss of 3.5 dB, and a fractional 3-dB bandwidth as wide as 6.2%.

V Resonators and bandpass filters have been implemented in the 5 GHz frequency range, based on "longitudinal leaky" surface-acoustic waves on standard YZ-cut lithium niobate substrate. The synchronous one-port resonators constituting a ladder filter operate in the fundamental mode. The electrode width in the resonators is above 0.25 μm, thus making them readily accessible for fabrication with optical lithography. Test resonators are fabricated to study the effects of the metallization ratio and aperture on the resonator behavior. For the prototype filter, a center frequency of 5.20 GHz, a wide fractional 3 dB bandwidth of 6.3%, a minimum insertion loss of 3.3 dB and a high stopband suppression of 25 dB have been achieved.

VI Surface acoustic wave (SAW) impedance element antenna duplexers provide compact, high performance, front-end components apt for industrial fabrication. We describe investigations on the design and modeling of a compact ISM antenna duplexer fabricated on a 36° YX-cut $LiTaO_3$ substrate based on SAW impedance elements. In particular, we have performed 3-D modeling of the inductive and capacitive electromagnetic couplings caused by the package parasitics for the duplexer. The use of a 1:3 IDT structure for the reduction of the passband width is discussed. The frequency response of the duplexer is predicted with the help of circuit simulation; the modeling is refined by optimization of the model parameters to improve the fit between the measured and simulated responses. We also report scanning optical imaging of the acoustic field within the resonator structures with the help of laser interferometry; this provides insight into the loss mechanisms beyond that attainable in mere electric measurements.

ISBN 951-22-7635-6
ISBN 951-22-7636-4 (PDF)
ISSN 1795-2239
ISSN 1795-4584 (PDF)